MODELING THE DEPENDENCE OF GALAXY QUENCHING ON STELLAR, BARYONIC AND HALO MASS IN THE ECO SURVEY

By

Mehnaaz Asad

Dissertation

Submitted to the Faculty of the

Graduate School of Vanderbilt University

in partial fulfillment of the requirements

for the degree of

DOCTOR OF PHILOSOPHY

in

Astrophysics

May 12, 2023

Nashville, Tennessee

Approved:

Andreas Berlind, Ph.D.

Kelly-Holley Bockelmann, Ph.D.

Jonathan Bird, Ph.D.

David Weintraub, Ph.D.

Sheila Kannappan, Ph.D.

Copyright © 2023 Mehnaaz Asad
All Rights Reserved

This dissertation is dedicated first and foremost to my parents, Sumbul Asad and Asad Ullah, whose endless support and love have led me to this moment in my life and to whom I am forever indebted. To my grandfathers, Syed Arif Bashir and Dr. Salamatullah, whose ardent love of learning inspires me and whose presence I felt cheering me on when this journey got difficult. And to Ángel, for his unwavering belief in me and constant encouragement.

ACKNOWLEDGMENTS

First and foremost, I'd like to thank my advisor, Andreas Berlind. Your support, patience and guidance have been invaluable to me over the past seven years and have helped shape the researcher I am today. Your belief in me throughout my time at Vanderbilt has given me the courage to face the many challenges graduate life has thrown at me. I am eternally grateful for how even when your schedule got busy, you never made me feel like you didn't have time to meet with me. So, thank you for being the gem of an advisor that you are. I'd also like to thank all the members of my committee for their guidance and support in the completion of the work in this dissertation.

I'd like to thank all my 9th floor friends who never failed to make my time at Vanderbilt fun - Abbie, Gillian, Adam, Karl (my gaming buddy), George, Laura, Stefan, Antonio, and Christina. I'd like to also thank my Nashville friends Mafe and Elle for making life in Nashville eventful. Above all, I'd like to thank the two friendships I made at Vanderbilt that I will treasure forever - Victor and John. You both very quickly became an integral part of my support system in Nashville and I am so grateful to have you both in my life. Victor, I have learned so much from you, especially when I was too afraid to ask Andreas for help in the early months as a graduate student! You've had a huge part to play in shaping the programmer I am today. Thank you for always taking out the time to teach me about mock catalogues, 'shuffling' and Pandas! (Even when I didn't ask for it!) John, you've witnessed me at my lowest and showed up when I needed someone and for that I owe you enormously! From our tea runs to the kitchen to every time you wandered into our office and all the selfies you left on my phone, you never failed to brighten my day.

I'd like to thank my parents for their love and support these past seven years. Even though you are thousands of miles away, you've never once made me feel the distance. I'd like to thank Swetha and Fatima for our hours long weekend chats, Virginia for bringing cheer to my weekends in the form of "domingos en español" and Ilma, Alex and Meghana for their invaluable friendship. Above all, I'd like to thank Ángel for being my partner in life, work and video games! Getting this PhD would not have been possible without you.

TABLE OF CONTENTS

Page

LIST OF TABLES . . . . . **vii**

LIST OF FIGURES . . . . . **viii**

1 Introduction **1**

1.1 The ΛCDM Cosmological Model and Structure Formation 2
1.2 Observing the Universe 4
1.2.1 Environmental COntext survey (ECO) and Volume-limited Samples 5
1.2.2 Galaxy Bimodality 6
1.2.3 Redshift-space Distortions and Galaxy Group Catalogues 7
1.3 Simulating the Universe 8
1.4 Modeling the Galaxy Halo Connection 9
1.5 Summary 11

2 Modeling the dependence of galaxy quenching on stellar, baryonic and halo mass in the ECO survey **12**

2.1 Introduction 12
2.2 Data 18
2.2.1 ECO catalogue 18
2.2.2 Photometry, stellar masses, and separating red and blue galaxies . . 20
2.2.3 21cm data, gas and baryonic masses 20
2.3 Mass and Quenching: A Preliminary Approach with ECO 21
2.4 Mock Galaxy Catalogues 24
2.4.1 For building correlation matrix 25
2.4.1.1 N-body simulation and halo catalogues 25
2.4.1.2 Populating halos with galaxies 25
2.4.1.3 Adding survey realism 26
2.4.1.4 Assigning group masses 27
2.4.2 For MCMC parameter exploration 27
2.4.2.1 N-body simulation and halo catalogues 27
2.4.2.2 Populating halos with galaxies 28
2.4.3 Assigning colour labels using quenching models 29
2.4.3.1 Hybrid quenching model 30
2.4.3.2 Halo quenching model 31
2.4.4 Adding survey realism and finding groups 31
2.5 Observables 32
2.5.1 Mass Functions 32

2.5.2 Blue fraction of group centrals and satellites 34
2.5.3 Measuring velocity dispersion as a function of group central mass . 36
2.5.4 Measuring average group central mass as a function of group velocity dispersion 38
2.6 Correlation Matrix 39
2.6.1 Methodology 39
2.6.2 Joint correlation matrix 41
2.6.3 Noise in the joint correlation matrix 44
2.7 Model fitting 45
2.7.1 Computing the likelihood function 45
2.7.2 Running the MCMC chains 47
2.8 Results 51
2.8.1 Comparisons between model predictions and ECO measurements of observables 51
2.8.1.1 Mass functions 51
2.8.1.2 Blue fractions of group centrals and satellites 53
2.8.1.3 Average group central stellar/baryonic mass as a function of velocity dispersion 55
2.8.1.4 Velocity dispersion as a function of group central stellar/baryonic mass 59
2.8.2 Red fraction of true centrals 60
2.8.3 Red fraction of true satellites 64
2.8.4 Total stellar- and baryonic-to-halo mass relations 68
2.8.5 Stellar- and baryonic-to-halo mass relations split by star formation state 69
2.9 Summary and Conclusions 71
2.10 Acknowledgements 77

3 Summary and Outlook 79

3.1 Summary 79
3.2 Outlook 80

References 81

LIST OF TABLES

Table Page

2.1 Survey geometry 27

2.2 Marginalised parameter constraints. Similar to Table 2.3, except that listed parameter values show the median, and the lower and upper limits corresponding to the 16 and 84 percentiles of the parameter values from the MCMC chain. . . 49

2.3 Best-fit Model Results. The table lists the best-fit values of the five shmr parameters and quenching parameters (columns 3-11) and the corresponding values of χ^2, number of degrees of freedom and $p-$values (columns 12-14) for all the combinations of galaxy sample-assumed quenching model, and choice of reducing noise in the correlation matrix via PCA (columns 1-2). 50

LIST OF FIGURES

Figure Page

1.1 The distribution of galaxies as mapped by the Sloan Digital Sky Survey. The observer is located at the center of the slice. Each point is a galaxy coloured by its (g-r) colour. (Image Credit: M. Blanton and SDSS; https://www.sdss4.org/science/orangepie/) 4

1.2 The Right Ascension - Declination distribution of the ECO survey. Each point represents a galaxy and is coloured according to its group halo mass as shown in the scale bar above the figure. The black and red hatched regions indicate overlap with ALFALFA and and RESOLVE-A respectively. (Image Credit: Eckert et al. 2016) 5

1.3 A high resolution slice of the entire 250 Mpc DMO Bolshoi simulation (Klypin et al., 2011) box. Points are dark matter particles and the colour gradient reflects their density such that the lighter colours correspond to areas of high density. (Image Credit: Stefan Gottlober (AIP); https://hipacc.ucsc.edu/Bolshoi/images/Images/Bolshoi_high-res.jpg) 10

2.1 Velocity difference measurements of ECO galaxies, where Δv is the difference between the velocity of a galaxy and the velocity of the group to which it belongs, as a function of its group central stellar mass (in units of $M_\odot$ assuming $h = H_0/(100km\ s^{-1}\ Mpc^{-1}) = 0.7$). The points are coloured by the foreground extinction-corrected and k-corrected u-r colour of the group central. 22

2.2 Velocity dispersion as a function of group central stellar mass (*left panel*) and average group central stellar mass as a function of group velocity dispersion (*right panel*) as measured for ECO galaxies. Red points show measurements for groups with red centrals and blue points show measurements for groups with blue centrals. In this figure, stellar masses assume $h = H_0/(100km\ s^{-1}\ Mpc^{-1}) = 0.7$. Both red and blue error bars are estimated from 100 bootstrap samples. 23

2.3 Stellar mass function measurements for ECO galaxies. Black points show measurements for ECO galaxies and 1σ errors estimated from dispersion among mock measurements are shown by the shaded region. Bin centers are plotted. 33

2.4 Blue fraction as a function of stellar mass for ECO galaxies. Purple and yellow points show measurements for ECO group centrals and satellites respectively. 1σ errors estimated from dispersion among mock measurements are shown by the shaded regions. Binning is the same as in Fig. 2.3. 35

2.5 Group velocity dispersion as a function of group central stellar mass for ECO galaxies. Red and blue points show measurements for red and blue group centrals respectively. 1σ errors estimated from dispersion among mock measurements are shown by the shaded regions. Bin centers are plotted. 37
2.6 Average group central stellar mass as a function of group velocity dispersion for ECO galaxies. Red and blue points show measurements for red and blue group centrals respectively. 1σ errors estimated from dispersion among mock measurements are shown by the shaded regions. Bin centers are plotted. 38
2.7 The average joint correlation matrix, R, for the stellar mass function (4 bins), blue fraction of centrals (4 bins), blue fraction of satellites (4 bins), average red group central stellar mass (4 bins), average blue group central stellar mass (4 bins), velocity dispersion of groups with red centrals (4 bins) and velocity dispersion of groups with blue centrals (4 bins) estimated from averaging 100 realizations of 64 independent ECO mock catalogues. Each cell shows the correlation between any two bins and is coloured according to the correlation coefficient as calculated using Eqn. 2.10. Each off-diagonal cell also includes a scatter plot of 64 mock measurements (black points) and the ECO measurement for comparison (white cross). Each diagonal cell shows the distribution of mock measurements for each bin of a given statistic (black histogram) as well as a Gaussian fit to the distribution (white line) along with the ECO measurement for comparison (white cross). The 4 individual boxes that are outlined in black represent the correlations between bins of the same statistic. 42
2.8 Stellar mass function (*left panel*) and baryonic mass function (*right panel*) for the stellar and baryonic quenching models where the models are jointly fit to all four observables. Black points show measurements for ECO and the error bars on the ECO measurements are calculated from the dispersion among 64 mock catalogues as shown in Fig. 2.3 and discussed in S 5.1. The black dashed line represents the best-fit model. The gray shaded region corresponds to a random subset of 200 models from the MCMC chains that correspond to a random sampling within the 68th percentile of the χ^2 distribution. The models shown here do not include PCA. Bin centers are plotted. 53
2.9 Blue fraction of group centrals and satellites as a function of stellar mass (*left panel*) and as a function of baryonic mass (*right panel*) for the stellar and baryonic quenching models where the models are jointly fit to all four observables. Points, error bars, dashed lines and shaded regions have the same meaning as in Fig. 2.3. Group centrals are shown in purple and group satellites are shown in yellow. The models shown here do not include PCA. Bin centers are plotted. 56

2.10 Average group central stellar mass as a function of group velocity dispersion (*left panel*) and average group central baryonic mass as a function of group velocity dispersion (*right panel*) for the stellar and baryonic quenching models where the models are jointly fit to all four observables. Points, error bars, dashed lines and shaded regions have the same meaning as in Fig. 2.3. The colours represent groups with red and blue centrals. The models shown here do not include PCA. Bin centers are plotted. 58
2.11 Velocity dispersion as a function of group central stellar mass (*left panel*) and as a function of group central baryonic mass (*right panel*) for the stellar and baryonic quenching models where the models are jointly fit to all four observables. Points, error bars, dashed lines and shaded regions have the same meaning as in Fig. 2.3. The colours represent groups with red and blue centrals. The models shown here do not include PCA. Bin centers are plotted. 60
2.12 Posterior probability distributions and confidence regions for the 5 SHMR/BHMR and 4 quenching parameters for the stellar and baryonic quenching models where the models are jointly fit to all four observables. The baryonic chain is shown in purple and the stellar chain in yellow. The histograms in the diagonal panels show the 1D posterior distributions of individual parameters. The off-diagonal panels contain 2D contours that show the region of parameter space that contains 68% (dark yellow and dark purple) and 95% (light yellow and light purple) of the MCMC probability for all pairwise combinations of the nine parameters. The yellow and the purple stars in the off-diagonal panels indicate the best-fit parameter values for the stellar and baryonic chain respectively. The models shown here do not include PCA. 61
2.13 Red fractions of true centrals as a function of their stellar mass (*left panel*) and as a function of their baryonic mass (*right panel*) for the stellar and baryonic quenching models where the models are jointly fit to all four observables. The yellow curve represents the best-fit model and the purple curves represent the random subset of 200 models from the MCMC chain that correspond to a random sampling within the 68th percentile of the χ^2 distribution. In the left panel, we also show curves from Dark Sage (black dashed line), TNG (black dashed-dotted line) and (Salim et al., 2018) (black dotted line). The models shown here do not include PCA. 64

2.14 Red fractions of true satellites as a function of their stellar mass (*left panel*) and as a function of their baryonic mass (*right panel*) for the stellar and baryonic quenching models where the models are jointly fit to all four observables. The yellow curve represents the best-fit model and the purple curves represent the random subset of 200 models from the MCMC chain that correspond to a random sampling within the 68th percentile of the χ^2 distribution. In the left panel, both sets of curves are average red fractions calculated in 25 evenly spaced logarithmic bins of stellar mass between $10^{8.6}$ and $10^{12.0}\,h^{-2}\mathrm{M}_\odot$. In this panel, we also show curves from Dark Sage (black dashed line) and TNG (black dashed-dotted line). In the right panel, both sets of curves are average red fractions calculated in 25 evenly spaced logarithmic bins of baryonic mass between $10^{9.0}$ and $10^{12.0}\,h^{-2}\mathrm{M}_\odot$. The models shown here do not include PCA. Bin centers are plotted. 67

2.15 The parameterized stellar-to-halo (*left panel*) and baryonic-to-halo mass relation (*right panel*) for the stellar and baryonic quenching models where the models are jointly fit to all four observables. Solid lines represent the best-fit analytical model and the shaded regions have the same meaning as in Fig. 2.3 except they are shown here in analytical space rather than in mock space. The (*left panel*) also includes SHMRs from literature - B19 (brown dotted), RP17 (orange dashed-dotted) and M18 (yellow dashed). The models shown here do not include PCA. Bin centers are plotted. 69

2.16 Similar to Fig. 2.15 but split by star-formation state where quenched galaxies are shown in red and star-forming galaxies are shown in blue. Bin centers are plotted. 70

CHAPTER 1

Introduction

When looking at the night sky today, we see structure on all scales - stars, planets and galaxies. However, the hierarchical organization of this structure does not end there. While some galaxies are found to exist in isolation, most of them actually form galaxy groups and clusters, which in turn form superclusters. Our own Milky Way galaxy is a member of the Local Group which lies on the edge of the Virgo Supercluster. On even larger scales, these superclusters form sheets of galaxies and the largest known structures in our Universe, galaxy filaments. Filaments are separated by massive voids, areas that contain little to no galaxies, and together they both form a mesh-like structure known as the ”cosmic web” (Bond et al., 1996). The field of cosmology includes the study of this observed large-scale structure (LSS) as well as the processes responsible for galaxy formation.

There exists a firmly established cosmological model, Lambda cold dark matter (ΛCDM), that predicts and explains this large-scale distribution of galaxies. According to ΛCDM, most of the matter that exists in the Universe is in the form of dark matter ($\sim 5/6$) (Ade et al., 2016a) while the remaining $\sim 1/6$ is ordinary matter i.e. matter that can be observed, like stars and gas. While this ordinary matter has been mapped at various wavelengths due to the fact that it interacts electromagnetically (in addition to interacting gravitationally), dark matter cannot be observed directly. Instead, its presence is ascertained by its gravitational interaction with ordinary matter. Some evidence for dark matter includes galaxy rotation curves (Rubin et al., 1980), gravitational lensing (Sheldon et al., 2003) and the scatter in radial velocities of galaxies within clusters (Zwicky et al., 1933).

Within the theory of structure formation, gravitationally bound regions of dark matter are called ”halos”. These halos form the most basic unit of structure within which galaxies form and evolve. Therefore, it is not unreasonable to assume that the internal properties

of the halos are likely to be closely tied to those of the galaxies that occupy them. This statistical and physical connection between the two is often referred to as the galaxy-halo connection. The better we can understand this connection, the better grasp we will have on the physics of galaxy formation and evolution, the distribution of dark matter and the parameters of the cosmological model.

In this dissertation, I present a statistical approach undertaken to better understand the galaxy-halo connection. To achieve this, I use a parameterized model applied to cosmological simulations to constrain this connection using various observational data of galaxies and galaxy groups.

1.1 The ΛCDM Cosmological Model and Structure Formation

The Big Bang, coloquially known as the birth of the Universe, was an event that occurred almost 13.8 billion years ago. The initial conditions of the Universe were extremely hot, dense, homogeneous and isotropic. However, this state changed soon after as the Universe underwent a period of rapid expansion known as inflation where it grew exponentially in size. Microscopic fluctuations in the pre-inflation density field froze during this inflation period and as the Universe expanded, these fluctuations amplified to later become the origin of structure as we know it. Post-inflation, the Universe continued to grow but at a slower rate and due to its growth it also cooled down tremendously until eventually, the temperature reached a point where ordinary matter was able to form. Protons and electrons were moving at slow enough velocities that they were able to bind together to form neutral hydrogen. This is known as the recombination period after which photons were able to stream through the Universe, unhindered by interactions with electrons, for the next 13.8 billion years. It is this afterglow of the Big Bang that is known as the CMB. It is a map of the hot and cold spots in the background radiation that correspond to perturbations in the density field, as measured by the Cosmic Background Explorer satellite (COBE) and the Wilkinson Microwave Anisotropy Probe (WMAP) spacecraft. In fact, the age estimate of

the Universe is based on measurements of temperature fluctuations in the CMB as well as measurements of the expansion of the Universe based on Type Ia supernovae (Riess et al. 1998; Perlmutter et al. 1999).

The ΛCDM model is alternatively referred to as the standard model of Big Bang cosmology as it is able to provide an explanation for many observed phenomena like the previously mentioned LSS, the accelerating expansion of the Universe, the abundances of primordial chemical elements, like hydrogen, helium and lithium, as well as the cosmic microwave background (CMB) (Aghanim et al., 2018). When referring to the ΛCDM model, Λ is a cosmological constant associated with dark energy that is used to explain the accelerating expansion of the Universe. Based on measurements from (Aghanim et al., 2018), dark energy accounts for $\sim 69\%$ of the mass-energy budget of the Universe. CDM refers to cold dark matter which is believed to make up $\sim 26\%$ of the mass-energy budget of the Universe. The remaining $\sim 5\%$ is comprised of all visible matter which implies that the mass budget of the Universe is dark matter dominated. While the visible matter is observable due to its interaction via electromagnetic force, the presence of dark matter can only be inferred due to its gravitational influence. It is because of this influence that dark matter was able to clump together to form regions of gravitational stablility called halos, whose density is ~ 200 times the mean density of the Universe. It is within these halos, that gravity further pulled in clouds of gas that condensed and cooled, forming stars and galaxies.

In order to provide context for the work presented in this dissertation, the main takeaways from this section are that the Universe is dark matter dominated, that dark matter provides the scaffolding for the growth of structure and that galaxies form and evolve in dense, gravitationally bound dark matter halos.

1.2 Observing the Universe

Mapping and quantifying the LSS as well as comparing with theoretical predictions requires surveys that map the 3-dimensional distribution of galaxies in space. Thanks to efforts made in the 1980s and early 2000s, we are able to do so with great accuracy using galaxy redshift surveys like Center for Astrophysics; CfA (Huchra et al., 1988), Two-degree-Field; 2df (Colless et al., 2001) and most notably the Sloan Digital Sky Survey; SDSS (York et al., 2000), as seen in Fig. 1.1. These surveys, the largest of which is SDSS, have really paved the way in quantifying the growth of structure by providing us with reliable spectroscopic information about the locations of not just galaxies and clusters but other astronomical objects of interest as well.

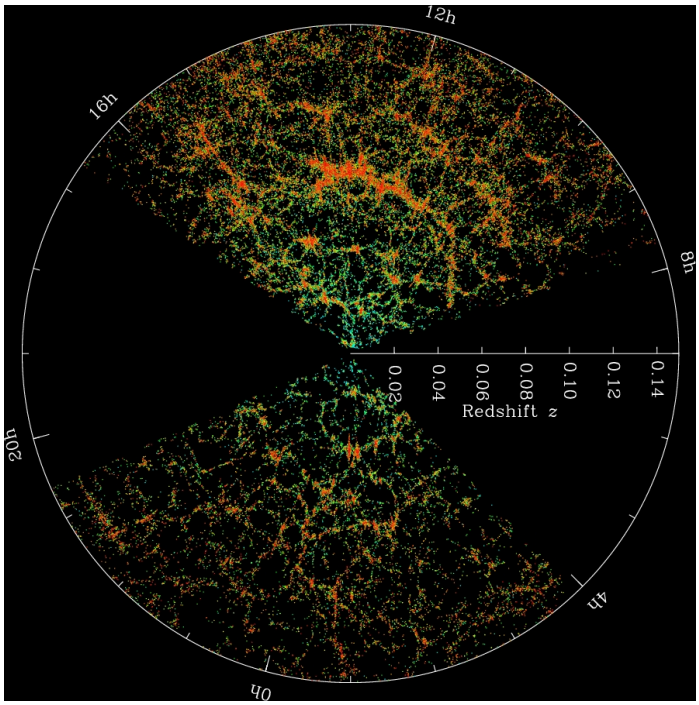

Figure 1.1: The distribution of galaxies as mapped by the Sloan Digital Sky Survey. The observer is located at the center of the slice. Each point is a galaxy coloured by its (g-r) colour. (Image Credit: M. Blanton and SDSS; https://www.sdss4.org/science/orangepie/)

1.2.1 Environmental COntext survey (ECO) and Volume-limited Samples

In order to compare theoretical models to observed galaxy data, the analysis presented in this dissertation makes use of the Environmental COntext survey (ECO). The ECO survey (Moffett et al., 2015), as shown in Fig. 1.2, is a census of roughly 12,600 galaxies that spans roughly 440,000 Mpc^3 in volume. It is a purely archival survey as it was constructed from the overlap of many redshift surveys, including (but not limited to) SDSS, 2dF, RESOLVE (Kannappan et al., 2008) and ALFALFA (Haynes et al., 2011).

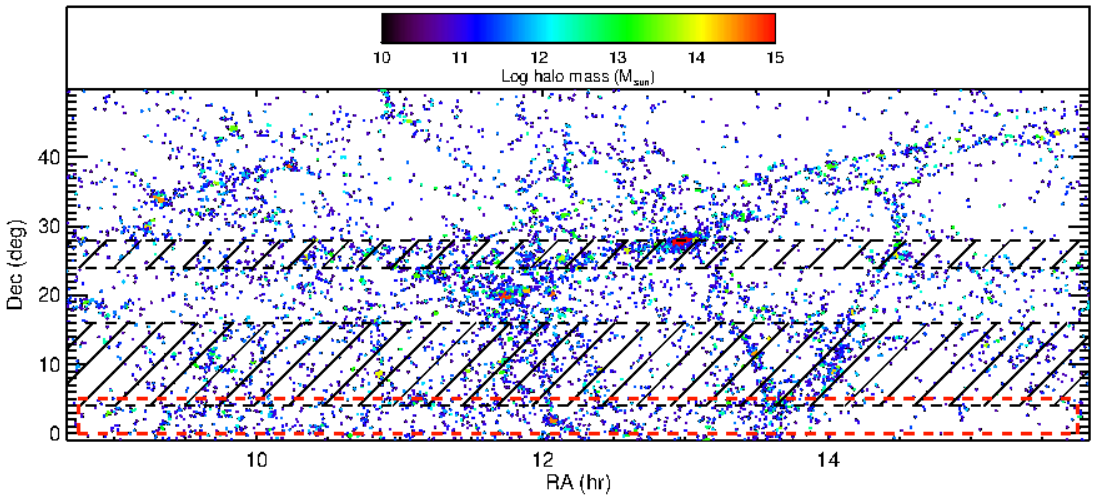

Figure 1.2: The Right Ascension - Declination distribution of the ECO survey. Each point represents a galaxy and is coloured according to its group halo mass as shown in the scale bar above the figure. The black and red hatched regions indicate overlap with ALFALFA and and RESOLVE-A respectively. (Image Credit: Eckert et al. 2016)

Intrinsically, all redshift surveys are flux-limited. This means that the number density of galaxies decreases with distance (i.e. redshift) because the further away we observe, only the brightest galaxies will be detectable. This effect can be seen in Fig. 1.1 whereby a clear gradient in the number of galaxies mapped is visible as we move away from the center of the cone to the outer edge of the survey. The edge corresponds to the survey's flux limit/magnitude cutoff which implies a magnitude-dependent incompleteness. ECO is different from a flux-limited sample in that, within its volume it is complete down to some magnitude threshold in a particular band. In other words, we have distances and brightness measurements for all galaxies within ECO's volume. This is what is called a volume-

limited catalog and given ECO, this threshold corresponds to $M_r < -17.33$. This threshold was calculated in Moffett et al. 2015 to be the SDSS completeness limit of $M_r < -17.23$ corrected for the fact that ECO galaxy magnitudes are brighter than those from the SDSS catalogue by approximately 0.1 mag. So, by only retaining all galaxies that are brighter than $M_r = -17.33$, Moffett et al. 2015 ensured that ECO would be complete down to that specific magnitude threshold.

1.2.2 Galaxy Bimodality

As more and more observations of galaxies were made, the more evident it became that there were a range of galaxy types ("morphologies"). This led astronomers like Edwin Hubble and Gérard de Vaucouleurs to come up with a classification scheme to help identify the different morphologies. While not all galaxies can be put into clearly defined categories, broadly speaking, the division includes galaxies that are ellipticals (galaxies of a smooth and ellipsoidal shape), spirals (galaxies with a disk and spiral arms, where star-formation is known to occur, and a central bulge), lenticulars (galaxies with a disk and central bulge but devoid of arms and regions of star-formation) and irregulars (galaxies with no obvious regular structure). de Vaucouleurs 1961 was able to study colours of galaxies via photometry and found there to be a correlation between galaxy colours and galaxy types where the colours varied smoothly from red to blue as galaxies advanced along the Hubble sequence from ellipticals (galaxies dominated by old stars) to spirals (galaxies dominated by massive young stars). Armed with a much larger sample of galaxies and their colours from SDSS, this bimodality was demonstrated to a high degree of significance whereby the distribution of colour was seen to have two distinctive peaks: a red peak that included mainly ellipticals and lenticulars, and a blue peak that included spirals and irregulars (Strateva et al., 2001). When looking at a figure of (u-r) colour as a function of absolute M_r magnitude, there is a clear distinction between older, redder galaxies that fall along a narrow band called the red sequence and younger, bluer galaxies that form a looser cluster called the blue cloud

(Baldry et al., 2004). It is thought that galaxies evolve from the blue cloud to the red sequence as their star formation is quenched i.e. they no longer have cold gas (baryons) from which to form stars. Kauffmann et al. 2003b and Kannappan et al. 2013 identified a mass scale above which quenched galaxies are more likely to dominate, since these galaxies have minimal cold gas reservoirs so their baryonic mass is roughly the same as their stellar mass and below this point, star-forming galaxies are more likely to be the norm. Also known as the bimodality scale, this mass scale was identified with stellar mass $M_* \sim 10^{10.5}\,\mathrm{M}_\odot$.

There are many physical mechanisms that have been proposed to explain galaxy quenching e.g. mergers between galaxies, inability of gas to cool due to shock heating and feedback from supernovae and active galactic nuclei (AGN). These physical mechanisms have a range of validity in terms of masses. Understanding what causes star formation to turn off is an ongoing challenge in galaxy formation and as of now, there is no consensus on (i) all the internal and external mechanisms responsible (ii) whether there is only one mechanism responsible for both the onset and the maintenance of quenching and (iii) how these mechanisms differ for centrals and satellites. Additionally, when it comes to internal mechanisms, it is unclear which galaxy and halo properties are tied to those mechanisms. So, if we are to better understand the galaxy-halo connection, understanding the formation and evolution of these two galaxy sub-populations is key to elucidating that connection. ECO boasts a highly complete selection in stellar and baryonic mass that extends into the gas-dominated low-mass galaxy regime making it ideal for our study of the dependence of galaxy quenching on mass.

1.2.3 Redshift-space Distortions and Galaxy Group Catalogues

In order to map the 3-dimensional distribution of galaxies, we require the x-y position of the galaxy and its distance from us, the observer. In redshift surveys, distance to galaxies is inferred from their spectra. Light emitted from the galaxy is stretched (or redshifted) in part due to the expansion of space itself (”Hubble flow”). However, in addition to the Hubble

flow, galaxies also experience peculiar motion which is due to the fact that most galaxies are found in groups or clusters where they experience a significant gravitational effect from one another. This alters their velocity as expected purely from the Hubble flow and therefore affects their measured redshifts and inferred distances. As a result, when their positions are plotted as a function of their redshift, they appear stretched on small scales and squashed on large scales. This effect is known as redshift-space distortions and this systematic error needs to be accounted for when determining distances to galaxies. Inaccurate distances can result in inaccurate galaxy group membership which can affect our statistical analysis of the galaxy-halo connection. So, we ensure that our modeling includes these distortions.

Observational galaxy catalogues pose an issue when trying to elucidate the galaxy-halo connection in that they don't contain information about halos due to the unobservable nature of dark matter. As a workaround, it is common practice to apply a group-finding algorithm to galaxy redshift surveys and in doing so, assign galaxies to groups resulting in a galaxy group catalogue. Armed with group halo measurements, the impact that the group environment has on galaxy quenching can be studied and galaxies from observed space can be compared with theoretical measurements from simulations where halo masses are available.

1.3 Simulating the Universe

While galaxy surveys provide us with large amounts of observational data, interpreting these observations requires accurate theoretical predictions. For this we rely on cosmological computer simulations. These N-body simulations are important in understanding the details behind galaxy properties and their evolution. Since dark matter is the backbone for the formation of galaxies in the Universe, it is also a key ingredient in simulations in addition to dark energy. These simulations evolve an initial distribution of particles from the early Universe (high redshift) to a present-day redshift of zero. This is done within a box that corresponds to a physical size within the real Universe and with well-defined initial

conditions that correspond to a given cosmological model. As the simulation proceeds in discrete time steps, particles are evolved through force calculations that include the effect of gravity on the particles' postions and velocities.

One flavour of cosmological simulations is a hydrodynamic simulation. In addition to modeling gravity and expansion, these simulations include baryonic physics to model the visible components of the Universe. (Vogelsberger et al., 2014) These simulations can be quite computationally expensive as they require modeling various complex baryonic galaxy processes like gas cooling, star formation, stellar feedback, AGN activity, supermassive black holes and the interstellar medium to name a few. These models all have a degree of uncertainty to them since the exact details of these processes aren't fully known.

Another, less complex approach is to use "dark matter only" (DMO) simulations where only dark matter particles need to be evolved via gravity. Since the physics involved is simpler than that of hydrodynamic simulations, fewer assumptions need to be made which means a smaller degree of uncertainty is present in the modeling. When looking at a snapshot of a simulation run, as shown in Fig. 1.3, the same web-like structure is visible as seen in Fig. 1.1.

While the output of a hydrodynamic simulation is a catalogue of galaxies that can be directly compared to observations, the output of a DMO simulation is a list of dark matter particle positions and velocities. A halo-finding algorithm (Behroozi et al., 2013a) is used to identify dark matter halos and then these halos are populated with galaxies using prescriptions that govern this process. The end result is a mock galaxy catalogue.

A vast majority of the work in this dissertation makes use of mock galaxy catalogues obtained from DMO simulations to statistically analyse the galaxy-halo connection.

1.4 Modeling the Galaxy Halo Connection

There are two techniques available when it comes to modeling the galaxy-halo connection: (i) *physical modeling*, where the physics of galaxy formation (star formation, feedback and

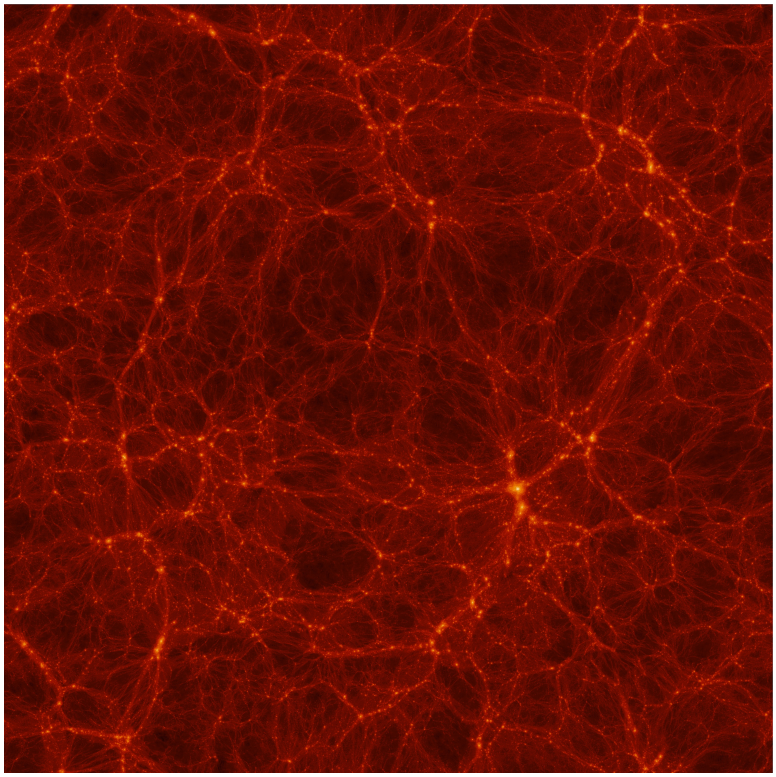

Figure 1.3: A high resolution slice of the entire 250 Mpc DMO Bolshoi simulation (Klypin et al., 2011) box. Points are dark matter particles and the colour gradient reflects their density such that the lighter colours correspond to areas of high density. (Image Credit: Stefan Gottlober (AIP); https://hipacc.ucsc.edu/Bolshoi/images/Images/Bolshoi_high-res.jpg)

gas cooling) is either directly simulated via hydrodynamic simulations or parameterized via semi-analytic models and (ii) *empirical modeling*, where data is used to constrain a certain set of parameters that determine tha galaxy-halo connection at a given redshift.

Within the family of empirical models, there exists a relation between the stellar mass of a galaxy and its halo mass called the stellar-to-halo mass relation (SHMR). This relation stems from the simplest assumption one can make about the galaxy-halo connection which is that the most massive halo hosts the most massive galaxy. While the SHMR can be predicted with galaxy models as well as measured directly from observed data, within the empirical framework it has a parameterized form which can and has been constrained using various observed measurements (Behroozi et al., 2019; Rodriguez-Puebla et al., 2017;

Moster et al., 2018). The form of this relation that we use for the work in this dissertation includes five free parameters and we use the SHMR as our prescription to populate dark matter halos with galaxies. Since the goal of our work is to study the dependence of quenching on mass, this also requires a parameterized model of quenching. The form of this relation that we use for the work in this dissertation includes four free parameters. Once galaxies are assigned to halos, we use the parameterized quenching model to assign colours to galaxies. The end result of this procedure is a mock galaxy catalogue with masses and colours which can then be compared to observational data using a chosen set of statistics.

As models transition from being physical to empirical in nature, any assumptions made become less directly tied to galaxy physics and therefore the model has less predictive power. However, empirical models have more flexibility when it comes to constraining the poorly understood aspects of the galaxy-halo connection with direct comparisons to data. That being said, there is a synergy that exists between the two approaches and both have their advantages. Physical models are useful in testing the assumptions that go into parameterizations of empirical models while empirical constraints, which are often quite diverse due to the flexibility in measurements used, are useful in determining the uncertainties in the physical models. Empirical models have been used to fix unconstrained parameters in hydrodynamic simulations.

1.5 Summary

The goal of the work presented in this dissertation is to determine the dependency of galaxy quenching on stellar, baryonic (cold gas + stellar) and halo mass and to test whether one of these three mass measurements is more correlated to the mechanisms that drive quenching. In this chapter, I have detailed concepts that are vital to understanding this work. In Chapter 2, I present the work that has been done in applying mass and quenching focused empirical models mentioned in this chapter to data from the ECO survey. Finally, in Chapter 3, I provide a brief summary of the analysis.

CHAPTER 2

Modeling the dependence of galaxy quenching on stellar, baryonic and halo mass in the ECO survey

Constraining the connection between the properties of galaxies and the dark matter halos they reside in is a powerful tool for understanding the processes responsible for galaxy formation. While the stellar-to-halo mass relation (SHMR) is one such connection that has been studied in detail, there is little consensus on the difference between the SHMRs of red and blue galaxies. The baryonic-to-halo mass relation (BHMR) and its conditional dependence on galaxy colour is even less studied. In this paper, we adopt an empirical forward-modeling mock-based approach to constrain a parameterized SHMR/BHMR model along with three types of quenching models, each employing a different driver of quenching: stellar, baryonic or halo mass. We use mass functions, galaxy blue fractions, and satellite kinematics as constraints measured directly from the ECO survey. Based on our model fits, we identify the mass scale that divides predominantly star-forming galaxies from the quenched population to be $\sim 10^{10.2}\,h^{-2}\mathrm{M}_{\odot}$ in stellar/baryonic mass or $\sim 10^{11.8}\,h^{-2}\mathrm{M}_{\odot}$ in halo mass. Moreover, we constrain the rate at which quenching depends on mass, finding that the quenched fraction of galaxies grows from 10% to 90% over $\sim$1.5 dex in mass. We find that the model where quenching depends on stellar mass provides the best fit to our data, with the halo-driven quenching model also providing an acceptable fit. As a result, we are not able to conclusively detect a dependence of the SHMR on galaxy colour. Finally, we compare our empirical results to predictions from galaxy formation models and show large discrepancies in the quenching fractions of both central and satellite galaxies.

2.1 Introduction

According to the standard Λ Cold Dark Matter (ΛCDM) paradigm of galaxy formation and evolution, the matter density of the Universe is dominated by gravitationally self-bound,

virialized regions of dark matter (DM) called halos. Within the radius of a halo, there can exist multiple, distinct self-bound structures (subhalos). Within this framework, galaxies form due to the cooling and condensation of gas in the centers of their halo's potential well (White and Rees, 1978; Fall and Efstathiou, 1980; Blumenthal et al., 1984). As a result, galaxy properties like stellar mass and luminosity are thought to be tightly coupled to the depth of the potential well and by extension to the mass of the halo itself.

There exist many different approaches to study this galaxy-halo connection. One approach has been to directly probe the mass of these halos using gravitational lensing (Mandelbaum et al., 2005, 2006; Guzik and Seljak, 2002; Sheldon et al., 2003; Velander et al., 2014), satellite galaxies or stellar velocities as dynamical tracers of the halo potential well (Erickson et al., 1987; More et al., 2009a,c, 2011; Eckert et al., 2017; Li et al., 2012; Zaritsky and White, 1994; Prada et al., 2003; Van Den Bosch et al., 2004; Conroy et al., 2007; Zaritsky et al., 1993; Carlberg et al., 1995) or X-ray studies that attempt to identify groups and clusters of galaxies (Lin et al., 2003, 2004; Lin and Mohr, 2004; Hansen et al., 2009; Yang et al., 2007; Kravtsov et al., 2018). However, these methods are limited in dynamic range in that they are only able to probe relatively high halo masses.

A second, theoretical, approach has been to model the physics behind galaxy formation using either semi-analytic models (SAMs) (Kauffmann et al., 1993; Cole et al., 1994; Gonzalez-perez et al., 2014; Henriques et al., 2015; Croton et al., 2016; Somerville and Primack, 1998) or large numerical simulations that combine both DM and gas (Katz et al., 1995; Springel and Hernquist, 2002; Nelson et al., 2015; McAlpine et al., 2016). However, there are many physical processes involved in galaxy formation that are still not fully understood, as exemplified by the fact that these simulations are not able to reproduce many observed quantities. Additionally, hydrodynamic simulations can be quite computationally expensive.

The advent of large galaxy surveys led to an alternative approach that attempts to link galaxies to halos using more empirical methods. One such example is the halo occupation

distribution (HOD) formalism which specifies a probability distribution for a halo of mass M to host N galaxies with certain intrinsic properties, such as luminosity, type or colour (Berlind and Weinberg, 2002; Cooray and Sheth, 2002; Peacock and Smith, 2000; Tinker et al., 2005; Bullock et al., 2002; Zheng et al., 2007; Yang et al., 2012; Carretero et al., 2015; Seljak, 2000; White, 2001). An extended, more complex formulation of the HOD is the conditional luminosity function (CLF) (Yang et al., 2003a; Van Den Bosch et al., 2003; Yang et al., 2003b, 2012) which adds an additional level of parameterization by describing the full probability distribution of galaxy luminosities for a given halo mass. These empirical approaches assume less about the physics behind galaxy formation than the theoretical approaches mentioned above, and thus lack their predictive power. However, assuming less physics also means that the models have more flexibility to constrain the unknown aspects of the galaxy-halo connection directly with data.

The HOD and CLF approaches treat central and satellite galaxies separately, with satellite galaxies being connected to their parent host halo statistically. This proves very useful when using DM simulation that do not resolve subhalos[1]. However, with a sufficiently high resolution simulation, where subhalos are resolved, it is possible to connect each galaxy to its immediate halo, centrals to parent halos and satellites to subhalos. This allows us to modify the HOD/CLF approach into the simplest assumption one can make about the galaxy-halo connection, which is that more massive galaxies live in more massive halos. This is called abundance matching and it describes a monotonic relation between a halo property, like mass or velocity, and a galaxy property, like stellar mass or luminosity. Abundance matching is usually applied to both halos and subhalos, and is often referred to as subhalo abundance matching (SHAM or simply AM; Kravtsov et al. 2004; Tasitsiomi et al. 2004; Vale and Ostriker 2004). AM can be used to determine the total stellar-to-halo mass relation (SHMR) by monotonically matching the abundance of halo masses (halo mass function; HMF) to the observed abundance of stellar masses (stellar mass function;

[1]We use the term *subhalo* to mean a halo that is within the virial radius of its parent halo.

SMF) (Behroozi et al. 2010, **hereafter B10**; Guo et al. 2010; Reddick et al. 2013; Girelli et al. 2020; Legrand et al. 2019; Shankar et al. 2017). This technique has been successful in reproducing various observational results including the redshift- and scale-dependent spatial clustering of galaxies (Kravtsov et al., 2004; Vale and Ostriker, 2004; Tasitsiomi et al., 2004; Conroy et al., 2006; Guo et al., 2010).

An alternative to inferring the SHMR from non-parametric abundance matching is to parametrize it and constrain those parameters in a forward-modeling Bayesian approach, by applying the model to DM halos from an N-body simulation to predict various observed galaxy properties like the SMF (Moster et al. 2010; Moster et al. 2013); SMF and star-formation rate (SFR) (Behroozi et al. 2013a; Rodriguez-Puebla et al. 2017, **hereafter RP17**) and SMF, SFR and quenched galaxy fractions (Behroozi et al. 2019, **hereafter B19**; Moster et al. 2018, **hereafter M18**).

Once a SHMR has been obtained, a natural next step in understanding the connection between galaxies and halos is to explore how other galaxy properties, besides mass, are connected to halos. Galaxy colour is one such property. The quenching of star formation in galaxies gives rise to two distinct populations of star-forming and quiescent galaxies, which can be seen in the strong bimodality that exists when looking at the distribution of galaxy colours (Baldry et al., 2004, 2006; Brinchmann et al., 2004; Weinmann et al., 2005; Wetzel et al., 2012; Kauffmann et al., 2003a). Kauffmann et al. 2003b identified a mass scale, called the bimodality scale (see also Kannappan et al. 2013), above which quenched galaxies are more likely to dominate, and below which star-forming galaxies are the norm. They identified this mass scale with stellar mass $M_* \sim 10^{10.5}\,\mathrm{M}_\odot$. Galaxy quenching is thought to be either host halo mass driven (Weinmann et al., 2005; Wetzel et al., 2012; Woo et al., 2013, 2015; Zu and Mandelbaum, 2016; Wang et al., 2018b), due to the large-scale environment density that surrounds the galaxy, stellar mass driven (Van Den Bosch et al., 2008; Knobel et al., 2015), or some combination of the aforementioned properties (Baldry et al., 2006; Bluck et al., 2014; Moffett et al., 2015; Bluck et al., 2016; Contini

et al., 2020; Peng et al., 2010, 2012). That is not to say that mass itself is responsible for quenching but rather the physical mechanisms that drive quenching correlate with mass. Galaxy quenching clearly correlates with mass, but whether it correlates more strongly with stellar, halo or even baryonic mass is a subtle question that is challenging to test. Galaxy samples that are complete in baryonic mass are few and far between and halo mass is difficult to probe due to its unobservable nature. Furthermore, how quenching differs for centrals and satellites is still an open area of research.

Zu and Mandelbaum 2016, **hereafter ZM16**, introduced a forward modeling approach that parameterized the quenched fractions of central and satellite galaxies as a function of both stellar and halo mass. They studied two different quenching scenarios: a purely halo mass driven model (*halo quenching model*) and a combination of stellar mass and halo mass (*hybrid quenching model*), and used them to predict the galaxy-galaxy lensing and clustering of red and blue galaxies in SDSS. They found that while both models described the clustering and lensing of red galaxies equally well, the halo quenching model outperformed when it came to predicting lensing signals of high mass blue galaxies. ZM16 demonstrated the power of using a parametric forward-model to probe the quenching-halo connection. This sort of modeling is able to map the desired relationships between quenching and fundamentally unobservable properties, such as DM halo mass or cental/satellite identity, onto statistics that can be directly measured in a galaxy survey. We would like to extend this type of analysis to investigate the role that baryonic mass could have on quenching.

In this paper, we adopt the quenching models from ZM16 to probe the relationship between galaxy quenching and stellar, baryonic, and halo mass. Specifically, we use the B10 parameterized form of either the SHMR or the baryonic-to-halo-mass relation (BHMR), together with the two parameterized quenching models from ZM16. With these models, we populate halos in a high resolution N-body simulation to produce a mock universe of galaxies with masses and colours that may be compared to real observations in order to

compute a Bayesian likelihood. The observed statistics that we use include mass functions, blue fractions of galaxies and satellite kinematics, measured using data from the Environmental COntext (ECO) survey (Moffett et al. 2015; **hereafter M15**). ECO represents a volume-limited, highly complete census of stellar mass and baryonic mass, that extends into the dwarf galaxy regime with a baryonic mass limit of $\sim 10^{9.3}\,\mathrm{M}_{\odot}$. This, coupled with ECO's large volume, makes it ideal for studies of mass and environment. M15 used ECO to examine the morphology-environment relation in a baryonic mass-limited catalog including group centrals and satellites. They found that, for central galaxies, there is no relationship between morphology and group halo mass at fixed stellar mass. As for satellites, they did find evidence of such a relationship where at fixed stellar mass, red early- and late-type galaxies occupy higher group halo mass environments than blue early- and late-type galaxies. In the M15 study, halo properties such as halo mass and central/satellite identification were estimated based on the properties of galaxy groups. The work done in this paper offers a different yet complementary approach by using forward modeling instead of direct measurements from observational data. In addition, there have been substantial updates to the ECO survey since M15, including improved atomic gas measurements, which we describe in more detail in §2.1.

This paper is organized as follows: in Section 2 we describe the ECO survey and the data we use, including how stellar masses, colour and baryonic masses are estimated. In Section 3 we show a preliminary exploration of ECO data. Section 4 specifies how we build our mock galaxy catalogues for both the correlation matrix we use in our MCMC framework as well as the mock universe we build at every point evaluated in parameter space. Section 5 details the observables that we use in our modeling, followed by Section 6, which describes how we construct the correlation matrix. We specify our modeling procedure in Section 7 and we present our results in Section 8. Finally, we summarize our conclusions in Section 9.

2.2 Data

2.2.1 ECO catalogue

In this work we make use of the Environmental COntext catalogue (ECO; see M15, for a thorough survey description and Eckert et al. 2016, **hereafter E16**, for a detailed description of photometry and galaxy properties.) ECO contains roughly 12,600 galaxies in a 440,000 Mpc^3 volume. It spans 130.05° ¡ R.A. ¡ 237.45° and -1° ¡ Dec. ¡ +49.85° with a line-of-sight group velocity range between 3000 $\mathrm{km\,s^{-1}}$ and 7000 $\mathrm{km\,s^{-1}}$. An additional 470 $\mathrm{km\,s^{-1}}$ buffer exists on either end which corresponds to roughly 1 Mpc. The purpose of this buffer is to mitigate edge effects due to the presence of groups and clusters with large peculiar velocities near the redshift boundaries. The ECO region encloses the A-semester of the REsolved Spectroscopy Survey Of a Local VolumE (RESOLVE; Kannappan et al. 2008) survey and its construction was primarily based on the overlap between the highly complete Updated Zwicky Catalogue (UZC; Falco et al. 1999) and the Sloan Digital Sky Survey (SDSS; Strauss et al. 2002) redshift databases. Redshifts are additionally complemented by RESOLVE, GAMA (Driver et al., 2011), 2dF (Colless et al., 2001), 6dF (Jones et al., 2009), HyperLEDA (Paturel et al., 2003) and ALFALFA (Haynes et al., 2011) surveys. These additional redshifts help in recovering galaxies that were missed by the main SDSS survey due to fiber collisions and photometric pipeline issues (Blanton et al., 2004). As such, ECO is a purely archival catalogue and provides a large sample to achieve robust statistics as well as large-scale environmental context for RESOLVE-A.

For our analysis, we use two separate samples from ECO - one for our stellar analysis and one for our baryonic analysis. More specifically, we use the latest release of ECO (DR3) which includes updates to survey membership, galaxy redshifts and a substantial addition of archival 21 cm data. DR3 is described in more detail in Z. Hutchens et al. (2023, submitted). For both samples though, we first use the Berlind et al. (2006) friends-of-friends (FOF) algorithm to assign galaxies to galaxy groups with $l_\perp = 0.07$ and $l_\parallel = 1.1$ as the linking lengths, in units of the mean inter-galaxy separation, which are based on Duarte

and Mamon (2014). Group centrals are chosen to be the most massive (stellar/baryonic mass) galaxy in each group. The rest of the galaxies are defined as satellite galaxies. A consequence of the FOF group-finding algorithm outlined in Eckert et al. (2017), **hereafter E17**, is that many isolated N=1 groups are falsely linked into pairs. To reduce the number of false pairs, E17 implement a pair-splitting algorithm where a mock catalogue is used (where true pairs are known) to identify a region in $\Delta cz - R_{proj}$ such that it contains 95% of true pairs. All pairs outside this region are broken into groups of N=1 resulting in the percentage of true pairs in the E17 group catalogue increasing from 62% to 73%. After using the group-finder in our analysis, we also implement the pair-splitting algorithm. While group-finding is carried out on the region of ECO that includes the buffer, the final samples used in this work are limited to galaxies excluding the buffer. Both stellar and baryonic samples encompass a volume of $\sim$ 151,829 Mpc^3 and are volume-limited as they are complete in absolute magnitude down to M_r = -17.33. The stellar sample contains 6546 galaxies with $M_\star \geq 10^{8.9}\,M_\odot$ (Eckert et al., 2016), which corresponds to ECO's stellar mass completeness limit. The baryonic sample contains 7057 galaxies with $M_b \geq 10^{9.3}\,M_\odot$ (Eckert et al., 2016), which corresponds to ECO's baryonic mass completeness limit. These limits are placed on the sample prior to group finding in addition to using the buffer region as mentioned above. This is done in order to mimic the modeling procedure, which we describe in detail in §7, as it is imperative that both model and data are treated in exactly the same way. Both mass completeness limits were calculated in E16 by examining the scatter in stellar and baryonic mass near the survey's luminosity completeness limit and requiring the percentage of galaxies above a given mass limit that are fainter than $M_r = -17.33$ to be less than 2%. While this pre-processing (group-finding and pair-splitting) assumes $h = H_0/(100km\ s^{-1}\ Mpc^{-1}) = 0.7$, for the remainder of the analysis of both samples as well as the figures presented in this paper we assume $h = H_0/(100km\ s^{-1}\ Mpc^{-1}) = 1.0$. Halo masses are in units of h^{-1} and stellar and baryonic masses are in units of h^{-2} unless otherwise stated.

2.2.2 Photometry, stellar masses, and separating red and blue galaxies

Details of the photometric data and galaxy properties for ECO can be found in M15 and E16 and in Eckert et al. (2015) for RESOLVE. Both surveys include reprocessed near-IR, optical and near-UV photometry. Stellar masses and colours were computed using a spectral energy distribution fitting (SED) procedure the details of which can be found in Kannappan et al. (2013).

In order to separate red and blue galaxies, a divider was chosen in the foreground extinction-corrected and k-corrected $(u-r)$ - M_* plane. A double gaussian was fitted to the distributions of u-r colour in 4 logarithmic bins of stellar mass (8.9-9.3, 9.3-9.8, 9.8-10.3 and >10.3) using a galaxy sample from ECO DR3 complete down to $M_\star = 10^{8.9}$ and within 3000 $\mathrm{km\,s^{-1}}$ < group velocity < 7000 $\mathrm{km\,s^{-1}}$. The fitting method is similar to that of M15 (§3.3) except more stellar mass bins are used. We note that the divider does not change significantly with twice the finer binning.

So, depending on the stellar mass of a galaxy in our ECO sample, if its u-r lies above the divider, it is assigned a red colour label, 'R', and if its u-r lies below the divider, it is assigned a blue colour label, 'B'.

2.2.3 21cm data, gas and baryonic masses

Since ECO is purely archival, it doesn't include any new 21 cm observations except where it overlaps with RESOLVE-A. The HI data in ECO DR3 includes 21cm detections or upper limits for roughly 90% of ECO galaxies mostly from the public ALFALFA 100 catalogue (α 100; Haynes et al. 2018). The inherited deeper RESOLVE-A HI data includes 3σ upper limits, confusion flags and de-confused detections. The portion of ECO that uses ALFALFA 100 includes 5σ upper limits and confusion flags, but no deconfusion is attempted. For more details on how confusion flags and upper limits were calculated we refer the reader to Stark et al. 2016 and Z. Hutchens et al. (2023, submitted). For the portion of ECO that either doesn't have robust HI detections, has weak upper limits or has badly

confused detections, an indirect method is used to obtain gas masses. A photometric gas fraction (PGF) technique is employed to determine the galaxy's gas-to-stellar mass ratio, the details of which can be found in E15. This ratio is then used, along with the stellar mass derived from SED fitting, to calculate a predicted HI mass. In the end, PGFs account for 60% of the galaxies in ECO DR3. All HI gas masses, both real and predicted, are multiplied by a factor of 1.4 to account for the presence of helium. The baryonic masses we use in our analysis are calculated by combining the stellar mass and the cold gas mass, whether from real HI data or the PGF technique.

2.3 Mass and Quenching: A Preliminary Approach with ECO

The goal of this paper is to better understand the relationship between mass and quenching with an interest in using intra-group galaxy dynamics as a probe of halo mass. To first order, we measure this quantity for ECO as is shown in Fig. 2.1. Each point in this figure is a galaxy coloured by the foreground extinction-corrected and k-corrected u-r colour of its group central.[3] We define Δv, which we use as a proxy for halo mass, as the difference between the line-of-sight galaxy velocity and the average line-of-sight velocity of all group members. We show this quantity as a function of group central stellar mass (in units of $M_\odot$ assuming $h = H_0/(100 km\, s^{-1}\, Mpc^{-1}) = 0.7$). While a dependency between quenching and stellar mass is evident, where more massive galaxies tend to be redder than less massive galaxies, it is less clear whether a dependency between quenching and Δv exists.

In order to mitigate the noise and projection effects, we attempt to measure velocity dispersion as a function of group central stellar mass (in units of $M_\odot$ assuming $h = H_0/(100 km\ s^{-1}\ Mpc^{-1}) = 0.7$) instead as shown in the left panel of Fig. 2.2. We do so in 4 evenly spaced logarithmic bins of stellar mass between $10^{8.9}$ and $10^{11.1}$ $M_\odot$. The left panel shows this measurement for groups with red centrals (red dashed line) and groups with blue centrals (blue dashed line). Instead of measuring a velocity dispersion per group, which would result in a noisy measurement for groups without many members, we mea-

[3] We use the term *group central* to mean a central galaxy in a galaxy group.

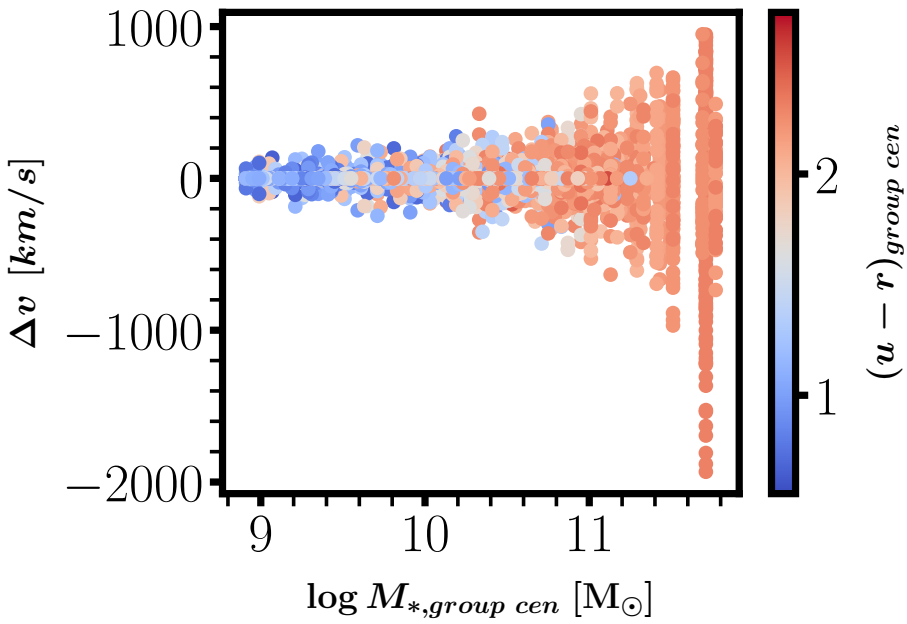

Figure 2.1: Velocity difference measurements of ECO galaxies, where Δv is the difference between the velocity of a galaxy and the velocity of the group to which it belongs, as a function of its group central stellar mass (in units of $\mathrm{M}_\odot$ assuming $h = H_0/(100km\ s^{-1}\ Mpc^{-1}) = 0.7$). The points are coloured by the foreground extinction-corrected and k-corrected u-r colour of the group central.

sure a velocity dispersion per bin. In other words, we stack many groups' members, whose respective Δv measurements are still calculated in the same way as in Fig. 2.1, in a bin of group central stellar mass and measure a velocity dispersion across different group members. Looking at the left panel, there is no clear evidence of a dependency between quenching and σ.

We then reverse this measurement and instead measure the average group central stellar mass (in units of $\mathrm{M}_\odot$ assuming $h = H_0/(100km\ s^{-1}\ Mpc^{-1}) = 0.7$) in bins of velocity dispersion as shown in the right panel of Fig. 2.2. In order to calculate a group velocity dispersion prior to binning we use the Gapper method (Beers et al. 1990, E17), which was found to be more robust than a simple rms method for low-N groups which is an issue when trying to calculate a velocity dispersion for a group with very few satellites. Group velocity dispersion was calculated using the following formula

$$\sigma = \frac{\sqrt{\pi}}{n(n-1)} \sum_{i=1}^{N-1} \Delta v_i w_i, \tag{2.1}$$

where N is the number of galaxies in each group, Δv_i is $v_{i+1} - v_i$ after having ordered the velocities in ascending order, and w_i is $i(N-i)$. We define v_i as the difference between the line of sight velocity of the galaxy and the average velocity of the group.

Looking at the right panel of Fig. 2.2, we do see a dependency between quenching and stellar mass. This measurement was made in 4 evenly spaced logarithmic bins of group velocity dispersion between 1 and 2.8 $\mathrm{km\,s^{-1}}$ for groups with red centrals and between 1 and 2.5 $\mathrm{km\,s^{-1}}$ for groups with blue centrals.

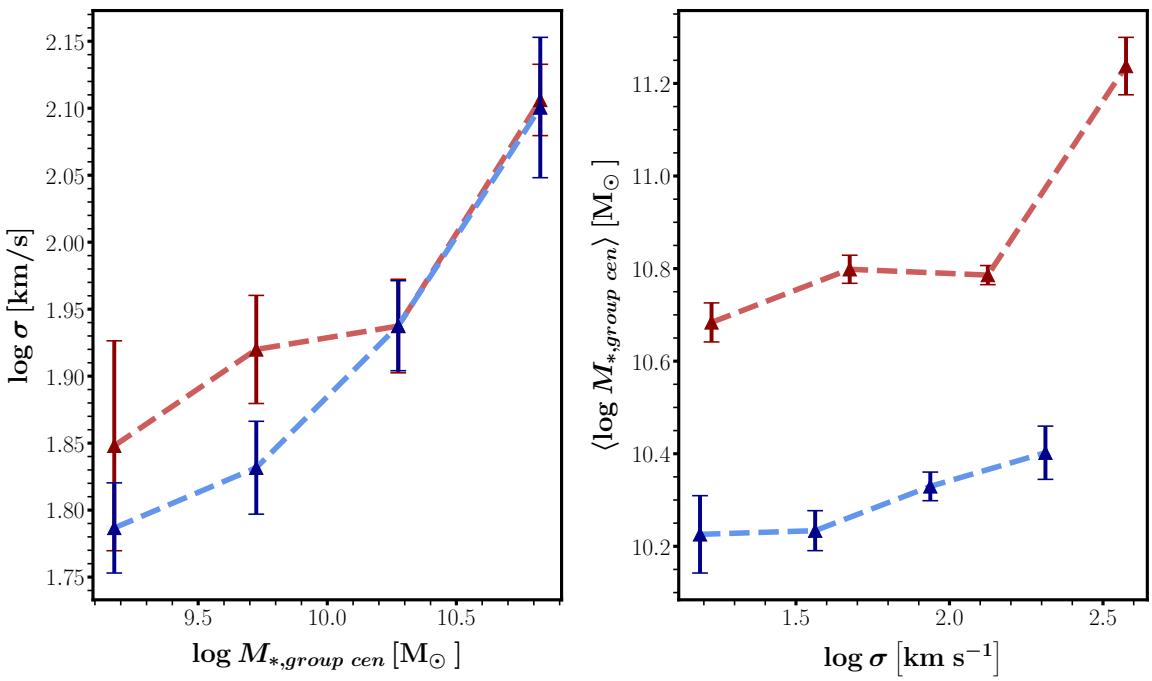

Figure 2.2: Velocity dispersion as a function of group central stellar mass (*left panel*) and average group central stellar mass as a function of group velocity dispersion (*right panel*) as measured for ECO galaxies. Red points show measurements for groups with red centrals and blue points show measurements for groups with blue centrals. In this figure, stellar masses assume $h = H_0/(100km\ s^{-1}\ Mpc^{-1}) = 0.7$. Both red and blue error bars are estimated from 100 bootstrap samples.

While these two panels paint a different picture as to what properties seemingly inform quenching, it does not mean that we can rule out a dependency between halo mass and

quenching according to the left panel of Fig. 2.2 since we know there to be a certain degree of scatter between velocity dispersion and halo mass. Moreover, studies have shown there to be a quenching dependency on halo mass for satellite galaxies (M15). We can also not conclude that stellar mass is the only factor that determines quenching as shown in the right panel of Fig. 2.2, since fixing velocity dispersion doesn't necessarily mean we are controlling for halo mass due to the scatter between these two quantities.

So, in order to more cleanly and directly measure halo mass we turn to ZM16 who introduced parameterized relations that include not just halo mass but stellar mass as well and how both these quantities affect the quenching of true centrals[4] and true satellites[5] separately. However, the only way to test these models and directly measure halo mass is to carry out forward modeling using an N-body simulation. Additionally, the only way to compare the model halo masses to ECO within our statistical framework is to use group halo masses from ECO which are obtained by applying a group finding algorithm to ECO galaxies. Since there are errors associated with the group finding process (Campbell et al., 2015), it is important that we incorporate these errors by applying a group finding algorithm in our model analysis as well, which can also only be done via forward modeling.

2.4 Mock Galaxy Catalogues

Mock galaxy catalogues serve two different purposes in our analysis. We use them to quantify errors in our modeling and also generate them at every point in parameter space in order to apply and evaluate our SHMR/BHMR and quenching models. In this section we describe how the mock catalogues are created in detail for both use cases.

[4]We use the term *true central* to mean a halo central.

[5]We use the term *true satellite* to mean a subhalo central.

2.4.1 For building correlation matrix

2.4.1.1 N-body simulation and halo catalogues

The mock catalogues are constructed from a cosmological N-body simulation that traces the evolution of DM in the Universe. The simulation assumes a *Planck 2015* (Ade et al., 2016b) cosmology, where $\Omega_{m,0} = 0.302$, $\Omega_{b,0} = 0.048$, $\Omega_{\Lambda,0} = 0.698$, $\sigma_8 = 0.828$, $n_s = 0.96$ and $h = H_0/(100km\ s^{-1}\ Mpc^{-1}) = 0.681$. We generated 8 realizations of the initial conditions using 8 different random number seeds where each realization was seeded with second order Lagrangian perturbation theory initial conditions using the `2LPTIC` code (Scoccimarro 1998; Crocce et al. 2006) and was evolved using the N-body code `GADGET-2` (Springel et al. 2001; Springel 2005). The initial power spectrum was generated using `CAMB` (Challinor and Lewis, 2011). The simulation evolved 1080^3 DM particles in a box of size 180 h^{-1}Mpc on a side from a starting redshift of $z_{\rm init} = 99$ to $z = 0$, with a gravitational force softening length of 6 h^{-1}kpc. The resulting particle mass is 3.881×10^8 $h^{-1}\mathrm{M}_\odot$. The DM halos are identified using `Rockstar` (Behroozi et al., 2013b). In order to calculate halo masses, `Rockstar` calculates spherical overdensities according to multiple user-specified density thresholds which for our set of mocks is a threshold of 200 times the mean background density, Δ_{200b}.

2.4.1.2 Populating halos with galaxies

We use the Zheng et al. (2007) HOD model to populate the DM halos with central and satellite galaxies, with HOD parameters chosen so as to reproduce the number density of the ECO survey, $n_{\rm gal}$ = 0.0831 h^3 Mpc^{-3}, as well as the clustering of the ECO survey. Each central galaxy is placed at the minimum of the halo gravitational potential and is assigned the mean velocity of the DM halo. Satellite galaxies are assigned the positions and velocities of randomly chosen DM particles within the host halo.

To assign a luminosity to each mock galaxy, we adopt the formalism of the CLF (Yang et al. 2003a; Van Den Bosch et al. 2003; Cacciato et al. 2009), which specifies functional

forms for the luminosity distributions of central and satellite galaxies as a function of halo mass. We then abundance match the luminosities obtained from the CLF to luminosities derived from a Schechter fit to the ECO r-band luminosity function extrapolated down to RESOLVE-B's lower r-band magnitude completeness limit of -17. With these new luminosities, the simulation volume has the same luminosity function as the data.

We assign other galaxy properties, like stellar mass and baryonic mass, to each of the mock galaxies by finding the galaxy in the ECO data that has the closest r-band absolute magnitude to that of the mock galaxy and then assigning the stellar and baryonic mass of the *real* galaxy to the mock galaxy. We assign colour to each galaxy by applying the relevant quenching model, which are described in detail in §4.3. As a result, the joint probability distributions of observed galaxy properties in the data are preserved in the mocks as well. However, this method doesn't ensure that the correlations between the joint probability distributions and *halo* properties will be correct since r-band absolute magnitude was the only galaxy property that was explicitly used to connect halos to galaxies.

2.4.1.3 Adding survey realism

Within our simulation box, we choose a location for the observer and then apply redshift-space distortions as well as carve out the survey geometry, details of which can be found in Table 2.1. We then apply translations and rotations of the coordinate system to extract additional mock samples. We maximize the number of catalogues we get from the simulation box by fitting as many mock volumes as we can, while still maintaining a distance of roughly 10 h^{-1}Mpc between them. This distance was chosen to prevent the same galaxies from appearing in more than one catalogue and in doing so, we ensure that the mock catalogues are as independent from each other as possible. The final result is a set of volume-limited mock galaxy catalogues in redshift-space with the same geometry as ECO. Given the volume of the survey, after applying necessary rotations and translations to the coordinate space, this process yields 8 ECO mock galaxy catalogues per box. Since 8 boxes

were used, this yields a total of 64 ECO mock galaxy catalogues.

2.4.1.4 Assigning group masses

As a final step in the mock-making procedure, we use the Berlind et al. (2006) friends-of-friends algorithm to assign galaxies to galaxy groups with $l_{\perp} = 0.07$ and $l_{\parallel} = 1.1$ as the linking lengths, in units of the mean inter-galaxy separation, which are based on Duarte and Mamon (2014). Once groups have been identified by the group-finder, group halo masses are assigned via abundance matching the integrated group absolute r-band magnitude, to a halo mass function. This group property is defined to be the sum total for the individual galaxies that make up a group. The halo mass function used is the Warren et al. (2006) function assuming the cosmology mentioned above. Group centrals are chosen to be the most massive (stellar/baryonic mass) galaxy in each group. The rest of the galaxies are defined as satellite galaxies. Halo radii are calculated using Eqn. 2.2 below:

$$R_{\rm halo} = \left[\frac{3M_{\rm h}}{4\pi\Delta_m\Omega_m\rho_c}\right]^{1/3} \tag{2.2}$$

where $\rho_c = 2.787 \times 10^{11} h^2\,{\rm M}_{\odot}\,{\rm Mpc}^{-3}$.

2.4.2 For MCMC parameter exploration

2.4.2.1 N-body simulation and halo catalogues

Since our priority when it came to building a correlation matrix was to utilise as many mock catalogues as we could, this required utilising as many simulation boxes as we could. Due to the associated computational cost, we chose to do so using a lower resolution simulation. While that enabled us to maximize the number of mock catalogues, in order to model the SHMR/BHMR and quenching relations, we required satellite information which the lower

Table 2.1: Survey geometry

Survey	RA range (deg)	DEC range (deg)	cz range (kms^{-1})	Volume Mpc/h^3
ECO	(130.05,237.45)	(-1,49.85)	(2530,7470)	191827.04

resolution simulation could not provide. Thus, we turned to a different simulation for our forward modeling. Within the MCMC framework, a single mock catalogue is constructed from a different cosmological N-body simulation that also traces the evolution of DM in the Universe. The simulation, which is named *Vishnu*, assumes a *WMAP-1* (Spergel et al., 2003) cosmology, where $\Omega_{m,0} = 0.25$, $\Omega_{b,0} = 0.04$, $\Omega_{\Lambda,0} = 0.75$, $\sigma_8 = 0.8$, $n_s = 1.0$ and $h = H_0/(100km\ s^{-1}\ Mpc^{-1}) = 0.7$. *Vishnu* was seeded with second order Lagrangian perturbation theory initial conditions using the `2LPTIC` code (Scoccimarro 1998; Crocce et al. 2006) and was evolved using the N-body code `GADGET-2` (Springel et al. 2001; Springel 2005). *Vishnu* evolved 1680^3 DM particles in a box of size 130 h^{-1}Mpc on a side from a starting redshift of $z_{\rm init} = 99$ to $z = 0$, with a gravitational force softening length of 2.2 h^{-1}kpc. The resulting particle mass is $3.215 \times 10^7\ h^{-1}\mathrm{M}_\odot$. The DM halos and subhalos were identified using the `Rockstar` code (Behroozi et al., 2013b) and halo masses were calculated assuming a threshold density of 200 times the mean background density, Δ_{200b}.

2.4.2.2 Populating halos with galaxies

We use the (sub)halo-based empirical model from B10, which assumes a monotonic relation between stellar mass and halo mass, to populate the DM halos with central and satellite galaxies. Specifically, we use the `Halotools` (v0.7) code (Hearin et al. 2017) which allows us to interact directly with the parameterized SHMR from B10. While the existence of a galaxy-halo connection doesn't specify which halo property is best matched to galaxies, a typical assumption is to use mass. The (sub)halo property we use to regulate the average stellar mass is its mass at the time of accretion, M_{acc}, which for host halos[6] is equivalent to their mass today. Using M_{acc} allows us to circumvent the issue of tidal stripping where a significant mass of the subhalo is thought to be lost once it enters its host halo. While in doing so we ignore the fact that the galaxy also experiences stripping to an extent, Conroy et al. 2006 and Reddick et al. 2013 showed that the SHMR does not evolve significantly be-

[6]We use the term *host halo* to mean a parent halo.

tween prior- and post-infall. More importantly they showed that choosing today's subhalo mass to populate the subhalo instead of its M_{acc} is unable to reproduce galaxy clustering as well as when choosing M_{acc}.

While the complete parameter space in B10 also includes parameters that govern the evolution of the SHMR with cosmic time, our modeling is done at a fixed redshift of $z \sim 0$ and so our SHMR/BHMR parameter space only includes 5 parameters: M_1, the characteristic halo mass, M, the characteristic stellar/baryonic mass, β, the faint-end slope, δ, the massive-end slope and ξ, the logarithmic scatter in M at fixed M_h. The characteristic halo/stellar/baryonic masses are the masses associated with the transition point between low-mass and high-mass galaxies, i.e. the "knee" of the SHMR. As shown in B10, the functional form we adopt is

$$\log_{10}(M_h(M_*)) =$$

$$\log_{10}(M_1) + \beta \log_{10}\left(\frac{M_*}{M_{*,0}}\right) + \frac{\left(\frac{M_*}{M_{*,0}}\right)^{\delta}}{1+\left(\frac{M_*}{M_{*,0}}\right)^{-\gamma}} - \frac{1}{2} \tag{2.3}$$

This best-fit functional form encompasses the quantitative effects of uncertainties in the observed galaxy stellar mass functions, halo mass functions as well as the abundance matching technique and is thus a robust estimator of the SHMR.

2.4.3 Assigning colour labels using quenching models

Once stellar masses are assigned, the last galaxy property left to assign is colour labels just as was done for our data sample. However, our data sample included colours that were the output of the SED fitting procedure which is information that is not available for our model galaxies. To do this we rely on the two quenching models from ZM16 as outlined in the sections that follow. Both models calculate a red fraction, f_{red}, as a proxy for quenching

efficiency. This fraction can be thought of as the probability that a galaxy of that stellar mass/living in a halo of that mass will be quenched.

2.4.3.1 Hybrid quenching model

The hybrid quenching model parametrizes f_{red} as a function of both M_* and M_h. As seen in Eqns. 2.4, 2.5 and 2.6, the quenched fraction of both true centrals and satellites depends on their stellar mass while the satellites are subject to an extra dependency on host halo mass.

$$f_{\rm red}^{\rm cen}(M_*, M_h) = 1 - g(M_*) = 1 - exp[-(M_*/M_{cen}^q)^{\mu_{cen}}] \tag{2.4}$$

where M_{cen}^q is a characteristic stellar mass and μ_{cen} determines how fast the quenching efficiency increases with M_*, where the greater the value of μ_{cen}, the more exponential the increase until it resembles a step function and the smaller the value of μ_{cen}, the more gradual the transition from star-forming to quenched.

As mentioned above, the satellites are subject to an extra halo quenching term $h(M_h)$, such that

$$f_{\rm red}^{\rm sat}(M_*, M_h) = 1 - g(M_*)h(M_h) \tag{2.5}$$

where

$$h(M_h) = exp[-(M_h/M_{sat}^q)^{\mu_{sat}}] \tag{2.6}$$

where M_{sat}^q is a characteristic halo mass and μ_{sat} determines the pace of satellite quenching.

2.4.3.2 Halo quenching model

The halo quenching model parametrizes f_{red} as a function of M_h alone. As seen in Eqns. 2.7, 2.8, halo mass is the sole driver of quenching for both true centrals and satellites.

$$f_{\rm red}^{\rm cen}(M_*, M_h) = 1 - exp[-(M_h/M_{cen}^q)^{\mu_{cen}}] \tag{2.7}$$

and

$$f_{\rm red}^{\rm sat}(M_*, M_h) = 1 - exp[-(M_h/M_{sat}^q)^{\mu_{sat}}] \tag{2.8}$$

where M_{cen}^q and M_{sat}^q are the characteristic halo masses responsible for triggering the quenching of central and satellites, respectively, and μ_{cen} and μ_{sat} are the respective powered-exponential indices controlling the transitional behavior of halo quenching across the characteristic halo masses.

When testing the quenching dependency on stellar and baryonic mass, we utilise the hybrid quenching model and refer to these models as the stellar/baryonic models. When testing the quenching dependency on halo mass alone, we utilise the halo quenching model and refer to this model as the halo model.

2.4.4 Adding survey realism and finding groups

After populating our halos with galaxies, we place a stellar mass cut at $\mathrm{M}_\star \geq 10^{8.6}\, h^{-1}\mathrm{M}_\odot$ equivalent to the stellar mass completeness limit of ECO in units of h=1.0. Within our simulation box, we then choose a location for the observer and apply redshift-space distortions. We include all galaxies between 2530 ¡ cz ¡ 12000. While the inner redshift is the same as that of ECO's (with its buffer), the outer redshift limit is chosen to take advantage of as much of the volume as possible.

As a final step in the Vishnu mock-making procedure, we use the Berlind et al. (2006) friends-of-friends algorithm to assign galaxies to galaxy groups with $l_\perp = 0.07$ and $l_\parallel =$

1.1 as the linking lengths, in units of the mean inter-galaxy separation, which are based on Duarte and Mamon (2014). These are the same linking lengths that are used while carrying out group finding on the ECO catalogue. Group centrals are chosen to be the most massive (stellar/baryonic mass) galaxy in each group. The rest of the galaxies are defined as satellite galaxies. The final Vishnu mock has a slightly modified inner redshift of 3000 km s^{-1} to mimic that of ECO (excluding its buffer) and encompasses a volume of $\sim 890641\ h^{-3}\,\mathrm{Mpc}^3$.

2.5 Observables

Since the goal of the project is to constrain not just the SHMR but the BHMR as well, all observables used have a stellar and a baryonic counterpart. We use four types of observables: stellar/baryonic mass functions (§5.1), blue fraction of group centrals and group satellites[7] as function of stellar/baryonic mass (§5.2), velocity dispersion as a function of group central stellar/baryonic mass (§5.3) and average group central stellar/baryonic mass as a function of group velocity dispersion (§5.4).

2.5.1 Mass Functions

The SMF describes the abundance of galaxies, both centrals and satellites, as a function of their stellar mass and is considered to be a very statistically precise measurement (Bell et al., 2003; Li and White, 2009; Baldry et al., 2012; Contini et al., 2017; Bernardi et al., 2017). We measure the number density of galaxies in 4 evenly spaced logarithmic bins of stellar mass between $10^{8.6}$ and $10^{10.8}\,h^{-2}\mathrm{M}_{\odot}$. The lower limit of the range corresponds to the ECO stellar completeness limit and the number of bins were chosen so as to ensure that each bin has atleast 30 galaxies (for both ECO and ECO mock measurements for building the matrix). Fig. 2.3 shows ECO measurements(black points) and the 1σ error contribution, which is calculated from the dispersion among 64 mock catalogue SMF measurements (shaded region) and used in Eqn. 2.13. The ECO SMF we measure, which has been studied

[7] We use the term *group satellite* to mean a satellite galaxy in a galaxy group.

in detail in E16, begins to drop off for masses $\geq 10.0\,h^{-2}\mathrm{M}_\odot$ and continues to rise, albeit slowly as we move to lower mass galaxies. Even though the mocks were not optimized to fit the ECO SMF, there is excellent agreement between the two even without the offset. This is because the mocks were optimized to fit the ECO luminosity function and luminosity and stellar mass exhibit a tight correlation.

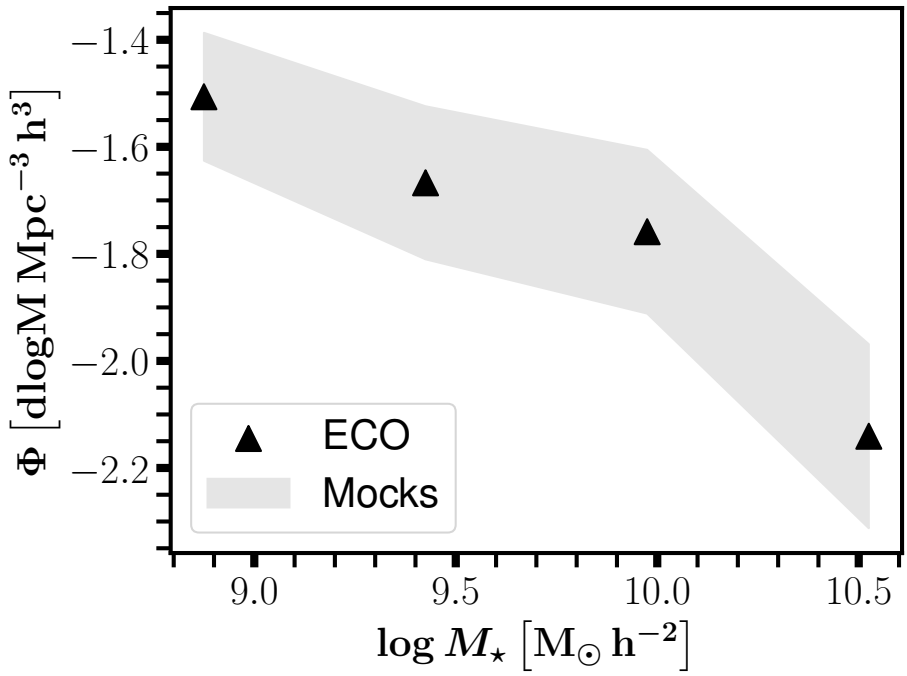

Figure 2.3: Stellar mass function measurements for ECO galaxies. Black points show measurements for ECO galaxies and 1σ errors estimated from dispersion among mock measurements are shown by the shaded region. Bin centers are plotted.

The baryonic mass function, BMF, describes the abundance of galaxies, both centrals and satellites, as a function of their baryonic (stellar plus cold gas) mass (Read and Trentham, 2005; Pan et al., 2019). We measure the number density of galaxies in 4 evenly spaced logarithmic bins of baryonic mass between $10^{9.0}$ and $10^{11.2}\,h^{-2}\mathrm{M}_\odot$. The lower limit of the range corresponds to the ECO baryonic completeness limit and the number of bins were chosen so as to ensure that each bin has atleast 30 galaxies (for both ECO and ECO mock measurements for building the matrix). The ECO BMF we measure, which has also been studied in detail in E16, begins to drop off for masses $\geq 10^{10.5}\,h^{-2}\mathrm{M}_\odot$ and

continues to rise, albeit slowly as we move to lower mass galaxies. While we don't show the BMF, its overall shape is very similar to the SMF. It too has a 1σ error contribution, which is calculated from the dispersion among 64 mock catalogue BMF measurements and used in Eqn. 2.13.

2.5.2 Blue fraction of group centrals and satellites

We define the blue fraction as the fraction of galaxies in a bin of stellar/baryonic mass that have been assigned the colour label 'B'. More specifically, we measure the blue fraction separately for group centrals and satellites which are shown in purple and yellow respectively in Fig. 2.4. We do so in 4 evenly spaced logarithmic bins of stellar/baryonic mass between $10^{8.6}$ and $10^{10.8}\,h^{-2}\mathrm{M}_{\odot}$ and $10^{9.0}$ and $10^{11.2}\,h^{-2}\mathrm{M}_{\odot}$ respectively (which are the same as those used for the mass functions). Fig. 2.4 shows ECO measurements of the blue fraction of group centrals and satellites (purple and yellow points) and the 1σ error contribution, which is calculated from the dispersion among 64 mock catalogue blue fraction measurements (purple and yellow shaded region) and used in Eqn. 2.13. As expected, the lower the mass of a galaxy, the more star-forming it is. The fraction decreases as you move to higher mass galaxies until it approaches nearly zero i.e. completely quenched. One can instead choose to interpret this as the quenched fraction (1 - f_{blue}) increasing with increasing stellar mass (Wang et al., 2018b,a; Davies et al., 2018). (This is not to be confused with the red fraction calculated by the quenching models in §4.3 which is a step before colour labels are assigned.) Given either interpretation, the trend applies to both group centrals and satellites as well as the baryonic version as well. When comparing the blue fraction of group centrals and satellites at fixed stellar mass, the blue fraction of group centrals is higher across the entire mass range. For galaxies between $10^{8.6}$ and $10^{9.6}\,h^{-2}\mathrm{M}_{\odot}$, this factor is close to 2x. In other words, at those lower stellar masses, group centrals are twice as likely to be star-forming than satellites. These centrals could be field galaxies which have grown and evolved outside the environmental influence that large groups and clusters have

on galaxy quenching. This latter effect is what affects the blue fraction at higher masses.

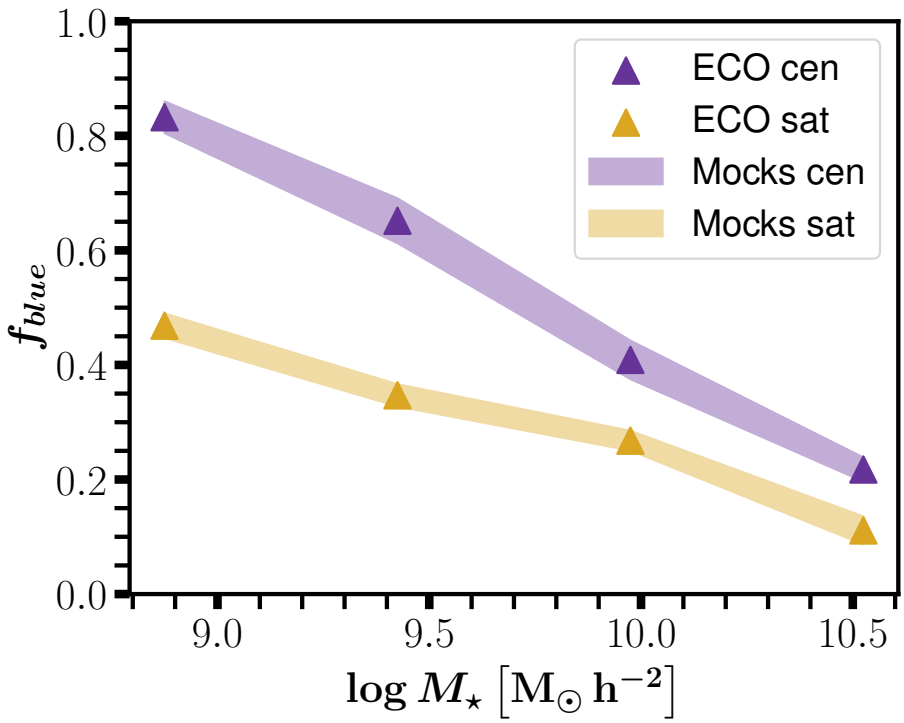

Figure 2.4: Blue fraction as a function of stellar mass for ECO galaxies. Purple and yellow points show measurements for ECO group centrals and satellites respectively. 1σ errors estimated from dispersion among mock measurements are shown by the shaded regions. Binning is the same as in Fig. 2.3.

When comparing the blue fraction of group centrals and satellites at fixed baryonic mass, the trend is quite similar to that at fixed stellar mass with two exceptions. The first is that the blue fraction of group centrals is not higher than that of satellites across the *entire* mass range. In the most massive bin ($10^{10.65}$ - $10^{11.2}\,h^{-2}\mathrm{M}_\odot$), there is complete overlap between group centrals and satellites when taking into account their 1σ error contributions. The second exception is that the separation between group centrals and satellites is not as extreme as in the stellar case i.e. less than a factor of 2x.

It is important to note that when comparing galaxies in bins of stellar mass we are comparing galaxies that correspond to a range of halo masses and that those halo masses also determine quenching and therefore affect your measurement of the blue fraction. Additionally, the group central and satellite designations here are a result of using a group finding

algorithm, which is prone to issues such as fragmentation and overmerging. (Campbell et al., 2015) This means that the central population could be contaminated with satellites which would result in an artificially lower group central blue fraction. On the other hand, the satellite population could also be contaminated with centrals which would result in an artificially higher group satellite blue fraction.

2.5.3 Measuring velocity dispersion as a function of group central mass

In order to calculate this statistic we first measure a velocity difference, Δv, which we define as the difference between the line of sight velocity of each galaxy and the average velocity of the group it belongs to, just as was done in Fig. 2.1. Once a Δv measurement has been calculated for every satellite, we stack satellites from different groups in bins of group central stellar mass and calculate a dispersion of all Δv measurements in each bin. Specifically, we measure this dispersion in 4 evenly spaced logarithmic bins of group central stellar mass between $10^{8.6}$ and $10^{10.8}\,h^{-2}\mathrm{M}_{\odot}$ (same binning as was used in the measurement of the SMF and blue fraction as a function of stellar mass) for both red and blue group centrals. This can be seen in Fig. 2.5 which shows ECO measurements of the group velocity dispersion as a function of group central stellar mass (red and blue points) and the 1σ error contribution, which is calculated from the dispersion among 64 mock catalogue velocity dispersion measurements (red and blue shaded region) and used in Eqn. 2.13. There is an offset at fixed stellar mass between groups with red centrals and groups with blue centrals in all bins except the third where there is significant overlap between groups of both central types. In the second bin that corresponds to a group central stellar mass between $10^{9.15}$ and $10^{9.7}\,h^{-2}\mathrm{M}_{\odot}$, we find this separation to be at its most extreme. Both groups with red and blue centrals exhibit a trend between their group central stellar mass and the velocity dispersion where low mass group centrals correspond to low velocity dispersions (therefore are the centrals of less massive systems). The converse is true for high mass group centrals.

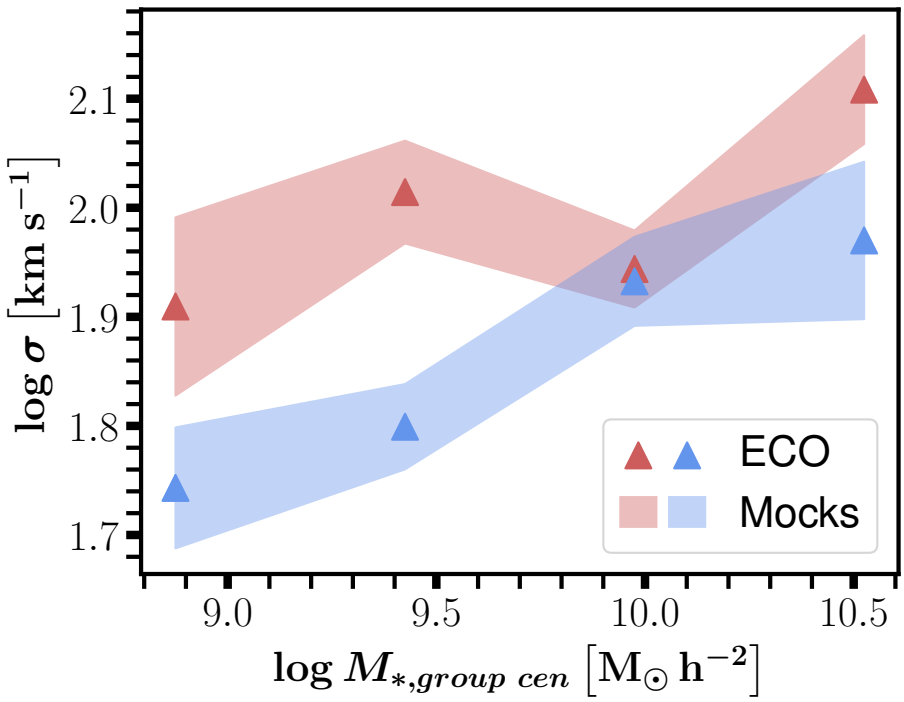

Figure 2.5: Group velocity dispersion as a function of group central stellar mass for ECO galaxies. Red and blue points show measurements for red and blue group centrals respectively. 1σ errors estimated from dispersion among mock measurements are shown by the shaded regions. Bin centers are plotted.

When comparing to this measurement's baryonic counterpart, the separation between red and blue group centrals at fixed baryonic mass is less prominent. While in the lowest mass bin ($10^{9.0}$ - $10^{9.55}\,h^{-2}\mathrm{M}_\odot$) groups with red centrals exhibit a higher velocity dispersion than groups with blue centrals, this offset reduces between $10^{9.55}$ and $10^{10.1}\,h^{-2}\mathrm{M}_\odot$ before increasing again between $10^{10.1}$ and $10^{10.65}\,h^{-2}\mathrm{M}_\odot$, all while taking into account their 1σ error contributions. More interestingly, while in the first three bins ($10^{9.0}$ - $10^{10.65}\,h^{-2}\mathrm{M}_\odot$), *on average*, groups with red centrals correspond to higher velocity dispersions, this trend reverses in the highest mass bin ($10^{10.65}$ - $10^{11.2}\,h^{-2}\mathrm{M}_\odot$) where it is groups with blue centrals that instead correspond to a higher velocity dispersion.

2.5.4 Measuring average group central mass as a function of group velocity dispersion

In order to calculate this statistic we first measure group velocity dispersion (σ) using the Gapper method (as described in §3). Once every group has a velocity dispersion measurement, we then measure the average group central stellar mass in 4 evenly spaced logarithmic bins of group velocity dispersion. We do so separately for groups with red centrals, where the range is between 1 and 2.8 $\mathrm{km\,s^{-1}}$, and groups with blue centrals, where the range is between 1 and 2.5 $\mathrm{km\,s^{-1}}$. This can be seen in Fig. 2.6, which shows ECO measurements of the average group central stellar mass as a function of group velocity dispersion (red and blue points) and the 1σ error contribution, which is calculated from the dispersion among 64 mock catalogue average group central mass measurements and used in Eqn. 2.13.

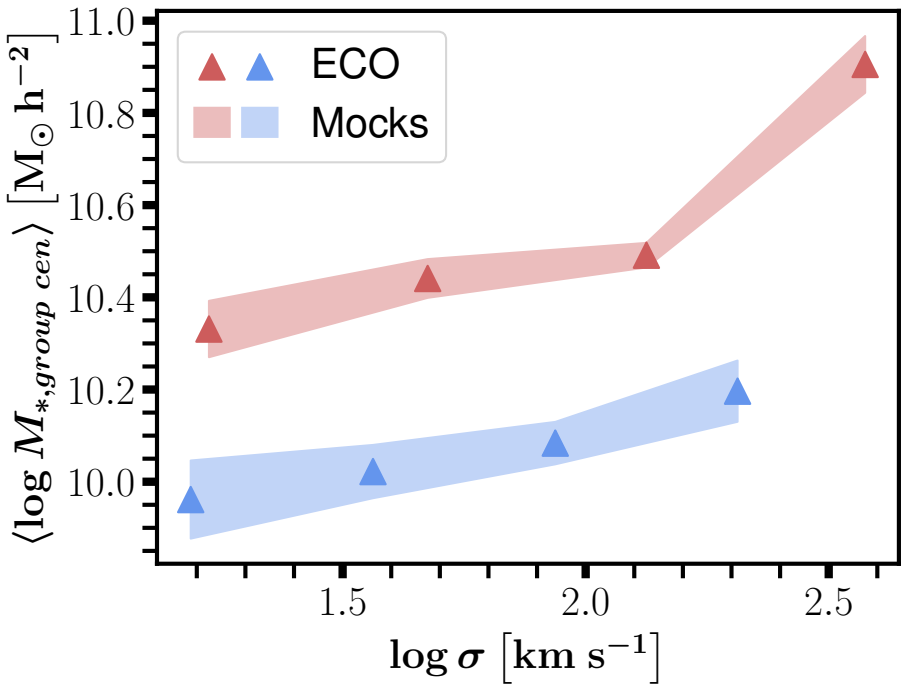

Figure 2.6: Average group central stellar mass as a function of group velocity dispersion for ECO galaxies. Red and blue points show measurements for red and blue group centrals respectively. 1σ errors estimated from dispersion among mock measurements are shown by the shaded regions. Bin centers are plotted.

There is an offset between groups with red and blue centrals in that the former are more massive regardless of the group velocity dispersion. ECO exhibits a correlation between the two quantities for both subpopulations, albeit a weak one initially. This applies to the baryonic version as well (where the binning is the same).

2.6 Correlation Matrix

In order to perform accurate modeling of the galaxy-halo connection measurements, just having an accurate model isn't enough. We also need to have accurate estimates of the errors on the measurements as well as the degrees of correlations between the measurements. More importantly, when running a MCMC analysis, we need to compute a likelihood function that can be expressed as P(data|model) which is the probability that a sample like ECO could have been observed given the model that is being tested. The right way to estimate this probability is to use a large number of independent realizations of the model, where each realization has the same geometry and volume as ECO, and to measure the amount of dispersion between measurements across all realizations. This is the correct error distribution of the data given the model that is being tested and it can be achieved by generating mock catalogues, as described in §4.1, which is what we use to measure a correlation matrix. The matrix we discuss in the following sections and show in Fig. 2.7 assumes the stellar model.

2.6.1 Methodology

To estimate the correlation matrix for the ECO sample, we use the 64 independent mock catalogues described in §3.1. However, in order to construct the mock catalogues we need to first choose a SHMR model to assign stellar masses to halos as well as a quenching model to assign colour labels to galaxies in the same way as is done in the model. Unfortunately, our mocks are limited in that they do not include satellite halo masses. That requires having used a different simulation with higher resolution as well as particle-based merger trees. This poses an issue with applying the SHMR model. So instead, we rely on a

more statistical approach to assign stellar masses to satellites as described in §3.1.2. This issue does not arise in the Vishnu simulation since it includes subhalo information. In order to assign colour labels to our mock catalogue galaxies, we use the best-fit quenching parameters found from a prior chain where we used our final set of observables in the modeling. In other words, we first run a chain using our final set of observables and use the best-fit parameters obtained from that chain as the matrix quenching parameters for the next chain. It is this next chain that we label as the final one and from which we report our results in the case of all three models - stellar, baryonic and halo.

It is important to note that there is a source of stochasticity present in the process of assigning colour labels to mock galaxies. Every time a red fraction is calculated per galaxy it is compared to a randomly generated number from a uniform distribution in order to determine whether the galaxy eventually gets labeled 'R' or 'B'. In order to control for this randomness, instead of using one realization of the matrix we take the average of 100 realizations and use that as the final correlation matrix in our chains.

Fig. 2.3, Fig. 2.4, Fig. 2.5, Fig. 2.6 show the standard deviation of stellar mass function, blue fraction, velocity dispersion and average group central stellar mass measurements across all 64 mocks as the shaded region in all four figures. While in general, the ECO measurements agree with the mock measurements, we want to emphasise that it is not essential that there be perfect agreement between the two. The purpose of the matrix is to capture the errors and correlations of our measurements which is why it is sufficient to get the measurements approximately right.

Once we have our measurements: 4 bins of stellar mass function, 8 bins of blue fraction, 8 bins of velocity dispersion and 8 bins of the average group central stellar mass from 64 mocks, we repeat this process 100 times, each time constructing a joint correlation matrix. Our final matrix is the average of 100 matrices and has dimensions 28 x 28. It is calculated using Eqns. 2.9 and 2.10

$$C_{ij} = \frac{1}{N-1}\sum_{1}^{N}(x_i - \overline{x_i})(x_j - \overline{x_j}), \tag{2.9}$$

where the summation is over $N = 64$ mocks, x_i and x_j are two of the measurements (e.g. one of the stellar mass function bins and one of the blue fraction bins) and $\overline{x_i}$ and $\overline{x_j}$ are the average measurements of that particular bin across all 64 mocks.

The next step is to normalize the covariance matrix by its diagonal elements

$$R_{ij} = \frac{C_{ij}}{\sqrt{C_{ii}C_{jj}}}, \tag{2.10}$$

where the diagonal elements are unity by definition and the off-diagonal elements range in values from -1 to 1.

2.6.2 Joint correlation matrix

Fig. 2.7 shows the average joint correlation matrix, R, given the stellar model. The x and y axes show all 28 bins for all 4 observables that are used. The 4 black squares along the diagonal from the bottom left to the top right (4x4, 8x8, 8x8, 8x8) show the correlation matrices for the 4 observables separately, while the rest of the cells show the correlations between different statistics. The colour of each cell reflects the degree of correlation present according to Eqn. 2.10. Within all the non-diagonal cells we show the actual measurements from one realization of the 64 mocks (black points). This is a much more direct visualization of the correlation coefficients. For example, all the cells of the stellar mass function correlation matrix have a coefficient value close to 1 which indicates a very strong correlation that can be seen in the black points in that 4x4. Conversely, the fifth cell from the bottom left row of the matrix has a coefficient value close to -1 which indicates a very strong anti-correlation that can be seen in the black points except the relationship is in the opposite direction. Meanwhile, the first cell from the top left of the matrix has a coefficient value close to 0 which indicates no correlation and which is reflected in the random distribution

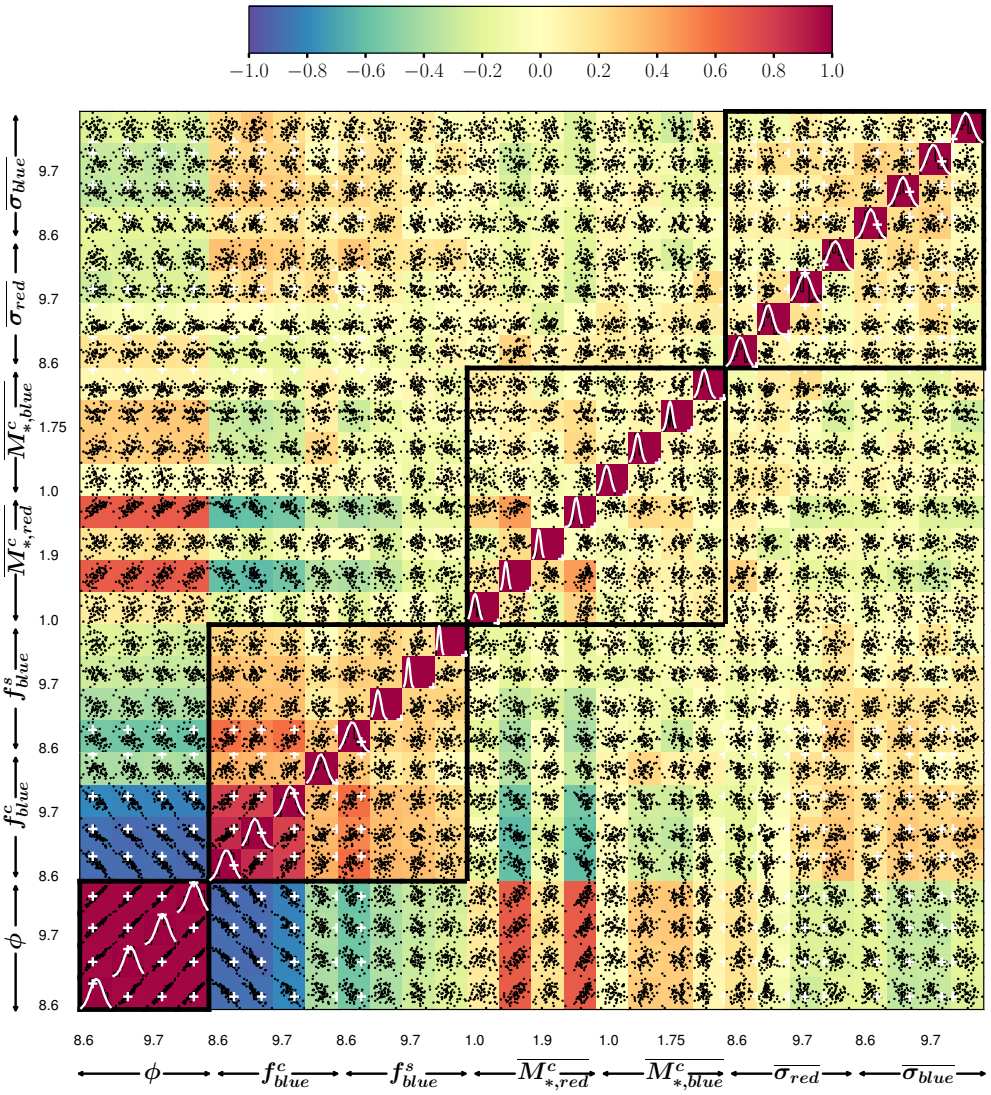

Figure 2.7: The average joint correlation matrix, R, for the stellar mass function (4 bins), blue fraction of centrals (4 bins), blue fraction of satellites (4 bins), average red group central stellar mass (4 bins), average blue group central stellar mass (4 bins), velocity dispersion of groups with red centrals (4 bins) and velocity dispersion of groups with blue centrals (4 bins) estimated from averaging 100 realizations of 64 independent ECO mock catalogues. Each cell shows the correlation between any two bins and is coloured according to the correlation coefficient as calculated using Eqn. 2.10. Each off-diagonal cell also includes a scatter plot of 64 mock measurements (black points) and the ECO measurement for comparison (white cross). Each diagonal cell shows the distribution of mock measurements for each bin of a given statistic (black histogram) as well as a Gaussian fit to the distribution (white line) along with the ECO measurement for comparison (white cross). The 4 individual boxes that are outlined in black represent the correlations between bins of the same statistic.

of the black points. We show the ECO measurements for comparison in all the cells (white plus signs). We remind the reader that, by construction, the mocks were not optimised to fit the ECO blue fraction and velocity dispersion measurements which is why in many cells the ECO measurement doesn't overlap with the mock measurements. The mocks were also not optimized to fit the ECO SMF but there is excellent agreement between the mock measurements of the SMF and that of ECO. This is because the mocks were optimized to fit the ECO luminosity function and luminosity and stellar mass exhibit a tight correlation with each other.

Let us now focus on the structure within the matrix, starting with the stellar mass function. With a correlation coefficient of almost 1, it is clear that neighbouring bins are extremely highly correlated. This can be attributed to the presence of large-scale structure in the survey volume which might make one mock more dense than another by an amount much greater than the sample variance which follows a more poisson-like distribution. This effect is called cosmic variance and implies that a mock with a higher overall number density than another will be more dense across all bins of stellar mass so the entire stellar mass function ends up being boosted.

Next, we move on to the blue fraction measurement, focusing first on the blue fraction of centrals. The first 3 bins show a strong correlation with each other but not as much with the fourth bin. According to the stellar model, the quenching of centrals is determined only by their stellar mass. So, by measuring their blue fraction at fixed stellar mass that correlation should no longer be present yet the matrix shows that it is. One reason for this is errors due to the group finding process, the main one in this case being satellites misclassified as centrals (Campbell et al., 2015). This problem is exacerbated when accounting for fracturing (one halo being associated with two or more groups) and fusing (two or more halos being associated with one group). To verify this, we remade the joint correlation matrix using *true centrals* and *true satellites* i.e. without any group information, and we found the correlations in the blue fraction of centrals disappeared. As for the blue fraction of

satellites, the correlations present are mostly in the first 2-3 bins. According to the stellar model, the quenching of satellites is determined by not just their stellar mass but also their host halo mass. So, after measuring their blue fraction as a function of stellar mass, any correlation that remains is due to the fact that at fixed stellar mass there is a range of host halo masses that determines quenching as well. However, most of this correlation is constrained to lower stellar mass bins because there aren't many satellites in our sample with stellar masses between $10^{10.65}$ and $10^{11.20}\,h^{-2}\mathrm{M}_{\odot}$.

Next is the average group central stellar mass in bins of velocity dispersion where we see little to no correlation between neigbouring bins of groups with red and blue centrals. The same can be said for the last observable which is the velocity dispersion in bins of red and blue group central stellar mass.

In addition to these features in the matrix, it is worth noting the strong anti-correlation between the blue fraction of centrals and the stellar mass function. This anti-correlation can be understood as the result of more dense mocks consisting of more red galaxies since the degree of clustering is greater for these galaxies, while the opposite is true for less dense mocks. Higher density would drive the blue fraction lower and increase the normalization of the SMF, and the opposite would be true for lower density. When we remade our joint correlation matrix using *true centrals* and *true satellites* i.e. without any group information, this strong anti-correlation disappeared for the same reasons mentioned above. A similar, though slightly weaker, trend is exhibited by the blue fraction of satellites which becomes even weaker when group information is excluded.

2.6.3 Noise in the joint correlation matrix

In addition to the noise present due to how colour labels are assigned to galaxies, there is another source of noise in our matrix and that is the fact that we have a limited number of mocks from which we calculate it. When the matrix is inverted, this noise amplifies and affects our calculation of χ^2 in unpredictable ways. We account for this problem by carry-

ing out a principle component analysis whereby we decompose the correlation matrix into its principle components by rotating the space of our measurements into a new coordinate system where most of the variation can be described using fewer dimensions than were originally present in the data. In doing so, the eigenvectors that describe this transformation are uncorrelated (i.e. the correlation matrix is diagonal). We sort the eigenvectors by their eigenvalues (λ_i^2) and remove those with low eigenvalues thereby removing the noise in the matrix. This is done at the expense of removing some information as well but the resulting χ^2 and $p-$values are more reliable. In accordance with Sinha et al. (2018), we only keep eigenvectors for which λ_i^2 is larger than the resolution with which the correlation matrix was measured as shown in Eqn. 2.11 below

$$\lambda_i^2 \geq \sqrt{\frac{2}{N_{mocks}}}, \tag{2.11}$$

where $N_{mocks} = 64$. By removing some eigenvectors we effectively reduce the number of data points that are used in the modeling procedure. For the stellar model we remove 9 eigenvectors and thus keep 19 data points. For the halo model we remove 11 eigenvectors and thus keep 17 data points. For the baryonic model we remove 10 eigenvectors and thus keep 18 data points. For all three models we evaluate, we run two versions: one using the entire average correlation matrix and one after removing noisy eigenvectors. We label the former chain as non-PCA and the latter chain as PCA in the text.

2.7 Model fitting

In order to forward model the dependency of quenching on mass we explore our parameter space using a MCMC method which we describe in the following sections.

2.7.1 Computing the likelihood function

For all three models we test, the parameter space is nine-dimensional consisting of five SHMR/BHMR parameters and 4 quenching parameters (centrals and satellites combined).

For each point in this parameter space we compute the likelihood function which is defined as P(data—model) and is the probability that our combined SHMR/BHMR and quenching model could have generated a dataset whose SMF/BMF, blue fractions, average group central stellar/baryonic mass and velocity dispersion measurements resemble those of ECO. Since the error distributions are approximately Gaussian, the likelihood function is proportional to $\exp(-\chi^2/2)$. The χ^2 statistic is calculated as follows

$$\chi^2 = \sum_{ij} \chi_i R_{ij}^{-1} \chi_j, \tag{2.12}$$

where R^{-1} is the inverse of the correlation matrix and χ_i is calculated as follows

$$\chi_i = \frac{D_i - M_i}{\sigma_i}, \tag{2.13}$$

where D_i is the ECO measurement for data point i, M_i is the model prediction for data point i and σ_i is the error in the ECO measurement which is calculated from the mocks using the matrix described in §3.4.

For the PCA chains, since the correlation matrix is diagonal due to the eigenvectors being uncorrelated, χ^2 is instead just a sum of the individual χ_i^2 contributions for the eigenvectors we choose to keep. Additionally, both D_i and M_i are also transformed into the new coordinate system.

Ideally, every time we moved to a new point in the parameter space we would recompute R and update our measurement of σ_i and χ^2 accordingly. However, this means we would need to create a new set of 64 mock catalogues each time which would increase the computational time of the MCMC chain to an unfeasible extent. Therefore, we make the approximation that our fiducial parameters are representative of the errors and correlation matrix in the parameter space of interest.

Since R and σ_i remain fixed, the only component of Eqn. 2.13 that needs to be computed for each combination of parameters is the model prediction, M_i. For all 4 observables, we

carve out a wedge in the Vishnu simulation that has roughly 6 times more volume than the ECO survey. In doing so, we are able to ensure that the uncertainties in M_i do not dominate the uncertainties in D_i and so they can be safely ignored in the calculation of the likelihood function.

2.7.2 Running the MCMC chains

For each new set of nine parameters we perform the following steps:

1. Populate the halo catalogue with galaxies according to the chosen SHMR/BHMR parameters

2. Apply redshift-space distortions to simulate observational effects as well as mass and velocity cuts

3. Calculate red fractions according to the quenching parameters for centrals and satellites.

4. Assign red ('R') or blue ('B') colour labels by treating the red fraction as a probability that that particular galaxy is quenched. The stochasticity that this process brings to the matrix is not present in the modeling procedure. Here we make sure that the same random number is generated every time for a given galaxy using its unique ID as the seed.

5. Find galaxy groups as described in §4.4 and assign observed central and satellite designation.

6. Compute all four observables as described in §5.

7. Calculate likelihood of model using Eqn. 2.12.

We use the `emcee` (v3.1.1) code (Foreman-Mackey et al. 2013) to generate our MCMC samples. The algorithm consists of an ensemble of walkers that probe the parameter space in such a way that a) each iteration of the chain depends only on the previous chain and

b) this process can be parallelized. All the walkers in one iteration, use the results from the previous iteration to maximize their efficiency i.e get closer and closer to the desired posterior distribution. For each chain, we use 500 walkers and 400 iterations for a total of 200,000 evaluations. To guarantee that our parameters have converged, we demand that their values as a function of iteration number do not contain any large-scale variations. We find that in all cases, the chains converge within 120-140 iterations.

We adopt flat priors for all 9 parameters. Allowable values for the scatter in the SHMR, ξ, are > 0.1 based on previous studies that have tried to constrain this parameter (B10, More et al. 2009b; Yang et al. 2009; Reddick et al. 2013; Tinker et al. 2017; Behroozi et al. 2019; Moster et al. 2018; zhi Cao et al. 2019; Hearin et al. 2013; Gu et al. 2016). For the remaining parameters, positive, non-zero values are considered allowable. Since MCMC algorithms are sensitive to their starting point, they require a burn-in phase to move towards a more desirable parameter space after which this burn-in phase can be discarded to obtain ”memory-less” walker positions. We throw out the first 120 - 140 iterations. We explore the posterior distributions for all 9 parameters as well as the joint distributions for different combinations of parameter pairs, as shown in Fig. 2.12. We retain the median and the percentiles containing 68% of the chain values for each parameter and provide those as our marginalised parameter constraints in Table 2.2. Additionally, we record the parameter values for the best-fit model, which is the point in our parameter space that corresponds to the lowest value of χ^2. To assess goodness-of-fit, we use the p-value associated with the best-fit χ^2 value. The p-value is the probability that our model could have produced a dataset like ECO. This information can be found in Table 2.3.

Table 2.2: Marginalised parameter constraints. Similar to Table 2.3, except that listed parameter values show the median, and the lower and upper limits corresponding to the 16 and 84 percentiles of the parameter values from the MCMC chain.

Quenching Dependence Model	**PCA**	$\log M_1$	$\log M$	β	δ	ξ	M^q_{cen}	M^q_{sat}	μ_{cen}	μ_{sat}
Stellar	No	$12.43^{+0.19}_{-0.10}$	$10.66^{+0.07}_{-0.07}$	$0.47^{+0.03}_{-0.03}$	$0.62^{+0.14}_{-0.15}$	$0.24^{+0.06}_{-0.06}$	$10.25^{+0.18}_{-0.06}$	$14.06^{+0.30}_{-0.50}$	$0.68^{+0.06}_{-0.05}$	$0.05^{+0.08}_{-0.04}$
	Yes	$12.41^{+0.07}_{-0.06}$	$10.76^{+0.05}_{-0.05}$	$0.49^{+0.04}_{-0.04}$	$0.62^{+0.06}_{-0.06}$	$0.20^{+0.05}_{-0.04}$	$10.52^{+0.05}_{-0.06}$	$14.08^{+0.06}_{-0.05}$	$0.74^{+0.05}_{-0.05}$	$0.18^{+0.04}_{-0.06}$
Halo	No	$12.74^{+0.09}_{-0.24}$	$10.72^{+0.05}_{-0.05}$	$0.50^{+0.02}_{-0.03}$	$0.60^{+0.11}_{-0.12}$	$0.25^{+0.04}_{-0.06}$	$12.29^{+0.32}_{-0.13}$	$12.76^{+0.75}_{-0.17}$	$0.97^{+0.19}_{-0.48}$	$0.54^{+0.18}_{-0.35}$
	Yes	$12.57^{+0.29}_{-0.18}$	$10.75^{+0.12}_{-0.16}$	$0.52^{+0.08}_{-0.06}$	$0.64^{+0.23}_{-0.17}$	$0.24^{+0.16}_{-0.08}$	$12.47^{+0.19}_{-0.29}$	$13.25^{+0.30}_{-0.34}$	$0.63^{+0.19}_{-0.18}$	$0.44^{+0.32}_{-0.25}$
Baryonic	No	$12.37^{+0.07}_{-0.11}$	$10.58^{+0.11}_{-0.09}$	$0.55^{+0.03}_{-0.04}$	$0.54^{+0.09}_{-0.11}$	$0.32^{+0.04}_{-0.07}$	$10.42^{+0.07}_{-0.04}$	$14.06^{+0.12}_{-0.23}$	$0.85^{+0.05}_{-0.07}$	$0.14^{+0.05}_{-0.04}$
	Yes	$12.40^{+0.06}_{-0.04}$	$10.76^{+0.05}_{-0.06}$	$0.50^{+0.03}_{-0.06}$	$0.62^{+0.05}_{-0.04}$	$0.21^{+0.05}_{-0.05}$	$10.53^{+0.05}_{-0.05}$	$14.08^{+0.05}_{-0.05}$	$0.74^{+0.05}_{-0.05}$	$0.20^{+0.05}_{-0.05}$

Table 2.3: Best-fit Model Results. The table lists the best-fit values of the five shmr parameters and quenching parameters (columns 3-11) and the corresponding values of χ^2, number of degrees of freedom and $p-$values (columns 12-14) for all the combinations of galaxy sample-assumed quenching model, and choice of reducing noise in the correlation matrix via PCA (columns 1-2).

Qeunching Dependence Model	**PCA**	$\log M_1$	$\log M$	β	δ	ξ	M^q_{cen}	M^q_{sat}	μ_{cen}	μ_{sat}	χ^2	**d.o.f.**	**p-value**
Stellar	No	12.66	10.73	0.47	0.44	0.18	10.19	14.05	0.74	0.02	46.12	19	$9\text{x}10^{-4}$
	Yes	12.40	10.64	0.48	0.47	0.22	10.35	14.08	0.84	0.03	14.97	10	0.27
Halo	No	12.70	10.63	0.48	0.57	0.34	12.08	12.66	1.52	0.54	62.14	19	$4\text{x}10^{-6}$
	Yes	12.80	10.91	0.56	1.10	0.22	11.94	12.74	0.85	0.79	14.33	8	0.15
Baryonic	No	12.49	10.59	0.58	0.33	0.27	10.40	13.85	0.95	0.18	55.70	19	$3.6\text{x}10^{-5}$
	Yes	12.30	10.45	0.39	0.52	0.27	10.33	13.96	0.97	0.25	27.43	9	$2\text{x}10^{-3}$

2.8 Results

We now present the results of our forward modeling aproach. While the third model we tested was a halo quenching one, we only show results from the stellar and baryonic models and leave the halo model to be discussed in the text where relevant. Additionally, while the results we show are for chains where PCA was not carried out, to determine the statistical significance of our three models and draw our conclusions we use the more conservative results corresponding to $p - values$ obtained after carrying out PCA. That being said, when we compared the parameter space between PCA and non-PCA MCMC chains for each of the three models we found that the 1D posterior distributions of individual parameters do overlap. In other words, our parameters are not entirely biased due to noise in the non-PCA MCMC chains. In §8.1 we show comparisons between model predictions of the four observables generated from our MCMC analysis and ECO. We present model predictions for the red fractions of centrals in §8.2 and satellites in §8.3 as well as comparisons with other work. Finally, we present our model predictions for the SHMR/BHMR for all galaxies as well as compare them to other published relations in §8.4 followed by the SHMR/BHMR split by star-formation state in §8.5.

2.8.1 Comparisons between model predictions and ECO measurements of observables

2.8.1.1 Mass functions

To demonstrate how well our forward modeling approach reproduces the observed galaxy stellar/baryonic mass functions, we show a comparison between our model predictions and ECO in Fig. 2.8. The error bars in the plot show σ_i, as estimated from the average correlation matrix in §6. The gray shaded region corresponds to a random subset of 200 models from the MCMC chain that correspond to randomly sampling within the 68th percentile of the χ^2 distribution. Visually, the best-fit stellar model (*left panel*) isn't able to fit the data to within 1σ. However, it is important to note that when data points are highly correlated, as

seen in the first 4x4 block in Fig. 2.7, assessing goodness of fit by eye can be misleading. Therefore, we rely on values of χ^2 and corresponding p-values. The best-fit value of χ^2 is 46.12 for the stellar model. This model has 19 degrees of freedom (4 bins of Φ + 8 bins of f_{blue} + 8 bins of σ-$\langle M_* \rangle$ + 8 bins of M_*-σ $-$ 5 free SHMR parameters $-$ 4 free quenching parameters). The resulting p-value is 0.0009 which suggests that the model is ruled out at $\sim 3.3\sigma$ level. However, the PCA $p-$value is 0.27 which suggests the model is ruled out at $\sim 1\sigma$ level. The best-fit model results for this and all subsequent MCMC chains are listed in Table 2.3. When compared to the baryonic and halo PCA models, the stellar model is the one that best fits our data.

The best-fit baryonic model (*right panel*) isn't able to fit the data to exactly within 1σ either although it is certainly a closer fit than the stellar model. However, the fact that the best-fit model is not centered within the range of acceptable models from the chain is unexpected. This can be better understood when looking at the posterior probability distributions for the BHMR parameters in Fig. 2.12 where the best-fit parameter values for all five parameters (as denoted by the brown star) are at the edge of their respective 68% confidence intervals. This coupled with the fact that most of the constraining power in modeling the SHMR/BHMR comes from the mass functions as compared to the other observables explains the relation between the offset in Fig. 2.12 and the offset in Fig. 2.8. The best-fit value of χ^2 is 55.70 for the baryonic model. This model also has 19 degrees of freedom and the resulting p-value is 0.000036 which suggests that the model is ruled out at $> 4\sigma$ level. In this case, the PCA $p-$value is 0.002 which suggests the model is ruled out at $\sim 3\sigma$ level. When compared to the stellar and halo PCA models, the baryonic model is the one that fits our data the least.

While there are other models in the chains, as indicated by the grey shaded region, that could provide a better fit to the ECO mass functions, it is the combination of all four observables that results in this particular best-fit model as having the highest likelihood. Were we to reduce the number of observables used or utilise the constraining power of

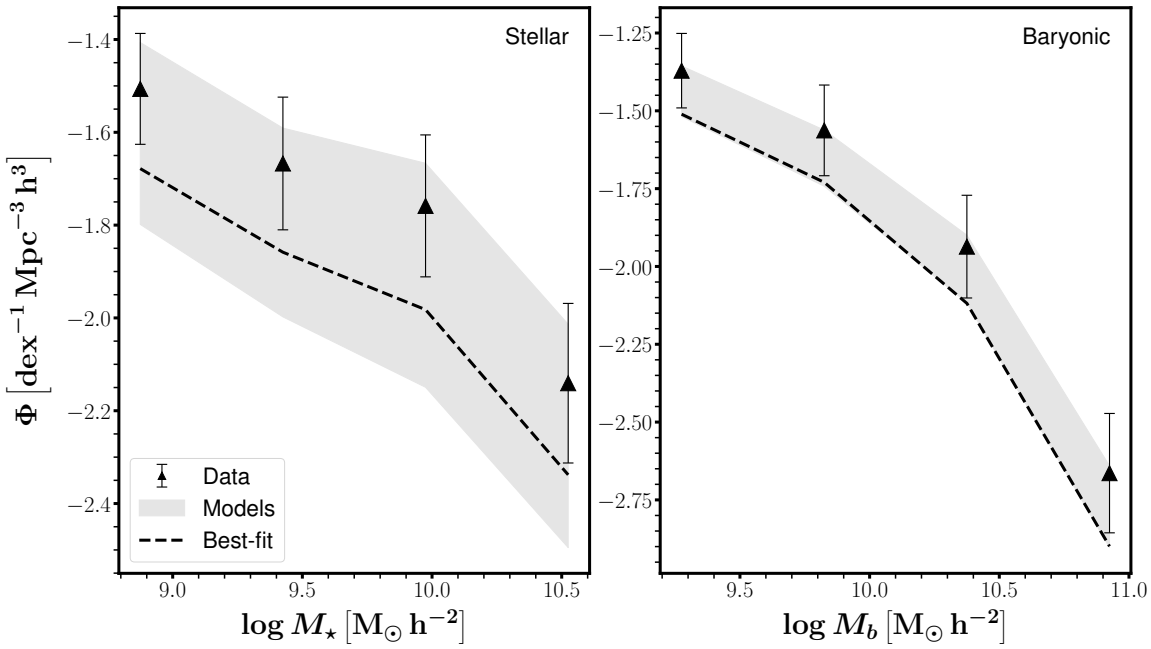

Figure 2.8: Stellar mass function (*left panel*) and baryonic mass function (*right panel*) for the stellar and baryonic quenching models where the models are jointly fit to all four observables. Black points show measurements for ECO and the error bars on the ECO measurements are calculated from the dispersion among 64 mock catalogues as shown in Fig. 2.3 and discussed in S 5.1. The black dashed line represents the best-fit model. The gray shaded region corresponds to a random subset of 200 models from the MCMC chains that correspond to a random sampling within the 68th percentile of the χ^2 distribution. The models shown here do not include PCA. Bin centers are plotted.

only the mass functions, the best-fit mass functions would have been able to reproduce ECO much more closely.

2.8.1.2 Blue fractions of group centrals and satellites

Fig. 2.9 shows a comparison between our model predictions and ECO for the blue fraction of group centrals and satellites as a function of stellar and baryonic mass. The points, error bars, dashed lines and shaded regions have the same meaning as in Fig. 2.3. Group centrals are shown in purple and group satellites are shown in yellow. Looking at the left panel first, we find that there are a few central bins at stellar masses of $10^{9.42}$, $10^{9.97}$ and $10^{10.52}\,h^{-2}\mathrm{M}_\odot$ for which the best-fit model is not able to reproduce ECO, although not as extreme a difference as in the satellite stellar mass bin of $10^{9.42}\,h^{-2}\mathrm{M}_\odot$ which is

more than 2σ. That being said, we conducted an experiment to see how much each of our four observables contributes to the $\sim 3.3\sigma$ tension where we removed each observable one by one (with replacement) and re-calculated χ^2 using the same matrix every time (except without the particular observable being tested). In the stellar model we found that the observable that contributes most to the tension is the blue fraction of centrals. However, this was done in non-PCA space so our test could have been influenced by noise to a certain extent. Irrespective of the offsets between the best-fit model and ECO, the best-fit as well as the subset of 200 models are able to capture the overall trend between blue fractions and mass as well as reproduce the separation between centrals and satellites at fixed stellar mass with a very small predicted degree of overlap between the two in the most massive mass bin between $10^{10.25}$ and $10^{10.8}\,h^{-2}\mathrm{M}_{\odot}$.

In the right panel, the second bin at a baryonic mass of $10^{9.82}\,h^{-2}\mathrm{M}_{\odot}$ for both centrals and satellites is where the best-fit deviates from ECO the most, especially the satellite measurement which is more than 3σ. When we conducted an experiment to see which of the four observables contributes most to the $> 4\sigma$ tension in the baryonic model, we found that both the blue fraction of centrals and satellites had an impact on our measurement of χ^2. The blue fraction of centrals had a slightly greater contribution though, which visually does not look obvious when compared to the second satellite mass bin. While this could be due to noise, it could also be evidence that the measurement of χ^2 involves a lot of components whose effects cannot be easily disentangled, particularly the inverse correlation matrix whose impact is too complex to fully capture. There is significant overlap between the models in the most massive bin of $10^{10.92}\,h^{-2}\mathrm{M}_{\odot}$ due to large satellite errors as measured from mocks. These large errors are in part due to low counts of satellites in that mass range. The overlap implies that within a baryonic mass range of $10^{10.65}$ - $10^{11.2}\,h^{-2}\mathrm{M}_{\odot}$, both centrals and satellites have an equal probability of being quenched with some models indicating that satellites at those masses have blue fractions of exactly 0 i.e. 100% probability of being quenched. For satellites to exist at such high masses, they have to be

residing in a cluster environment where everything is quenched. Central galaxies of such massive groups are also quenched. Of course, it is important to recall that this measurement was obtained by including group finding within the forward modeling framework and these algorithms are prone to issues such as fragmentation and overmerging. This means that the central population could be contaminated with satellites which would result in an artificially lower central blue fraction. On the other hand, the satellite population could also be contaminated with centrals which would result in an artificially higher satellite blue fraction. That being said, both the best-fit and the rest of the models are able to capture the separation between centrals and satellites at fixed baryonic mass as well as the overall trend between blue fractions and mass.

While there are other models in the chains, as indicated by the purple and yellow shaded regions, that could provide a better fit to the ECO blue fractions, it is the combination of all four observables that results in this particular best-fit model as having the highest likelihood. Were we to use the total blue fraction, for example, instead of split by centrals and satellites, the best-fit model might have been able to reproduce the data much more closely.

2.8.1.3 Average group central stellar/baryonic mass as a function of velocity dispersion

Fig. 2.10 shows a comparison between our model predictions and ECO for the average group central stellar and baryonic mass as a function of velocity dispersion. The points, error bars, dashed lines and shaded regions have the same meaning as in Fig. 2.3. The colours represent red and blue group centrals. Looking at the left panel first, the red models deviate from the data in the last two bins of velocity dispersion corresponding to a range of 80 - 640 $\mathrm{km\,s^{-1}}$ and the deviation in the last bin is more than 3σ. When conducting an experiment to see which observable contributes most to the $\sim 3.3\sigma$ tension in the stellar model, we found that the average red group central stellar mass as a function of velocity dispersion

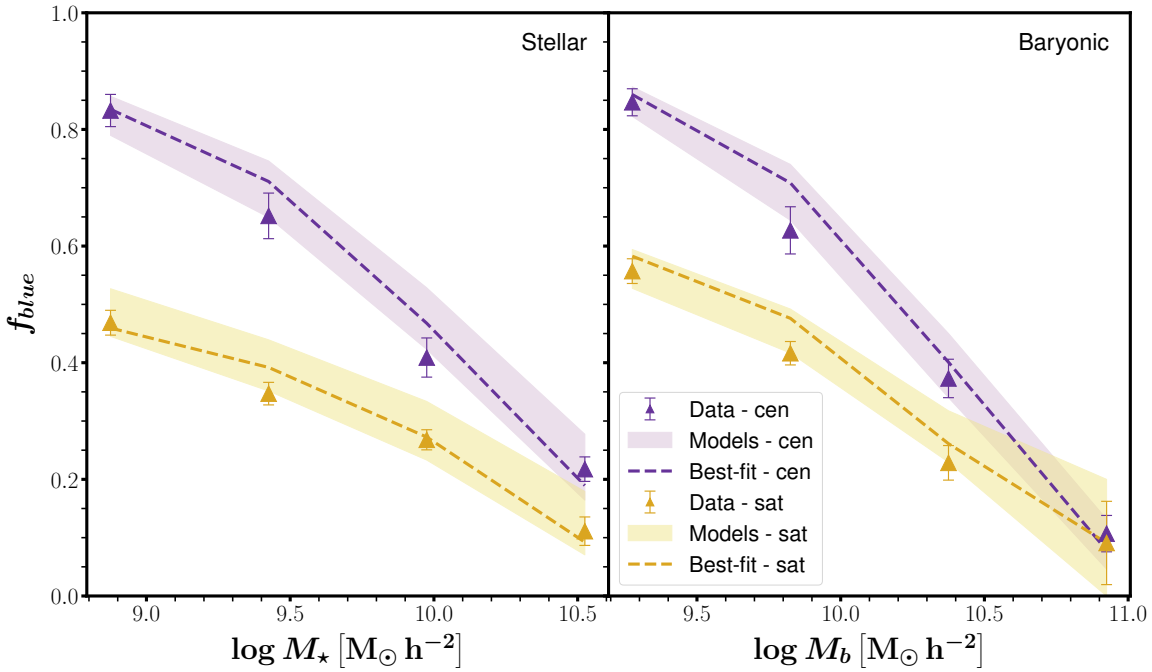

Figure 2.9: Blue fraction of group centrals and satellites as a function of stellar mass (*left panel*) and as a function of baryonic mass (*right panel*) for the stellar and baryonic quenching models where the models are jointly fit to all four observables. Points, error bars, dashed lines and shaded regions have the same meaning as in Fig. 2.3. Group centrals are shown in purple and group satellites are shown in yellow. The models shown here do not include PCA. Bin centers are plotted.

measurement was second in its impact after the blue fraction of centrals. However, both the best-fit model and the subset of 200 models follow the upward trend between velocity dispersion and mass as well as exhibit a $\sim$0.35 dex separation at fixed velocity dispersion between red and blue group centrals.

The separation that exists at fixed velocity dispersion between red and blue group centrals is expected since, by definition, the hybrid model states that the only galaxy property that determines quenching of centrals is their stellar mass. However, this separation persists in the halo quenching model as well which is surprising since that model states that the only property that determines quenching of centrals is their halo mass. So we do not expect to see a separation between the two galaxy populations when we fix the quantity that determines quenching. The reason for this behaviour is that there exists a large amount of scatter between velocity dispersion and halo mass. We found this scatter to be roughly constant at $\sim$ 0.4 dex for red galaxies. For blue galaxies, this scatter ranges from 0.35 to 0.55 and increases with velocity dispersion. In §3, we showed that due to this scatter, we cannot conclusively say that the separation seen in the right panel of Fig. 2.2 tells us that stellar mass is the only factor that determines quenching and we have shown this through our forward modeling approach as well. Both halo and stellar models have high p-values, after accounting for noise in the matrix, although the stellar model is almost twice as probable.

When looking at this observable in the baryonic model, the red best-fit and subset of 200 models struggle to reproduce the data in the last two bins of velocity dispersion corresponding to a range of 80 - 640 $\mathrm{km\,s^{-1}}$ to where the deviation in the last bin is more than 3σ. Overall, this observable resembles that from the stellar model in that both the best-fit and subset of 200 models exhibit an upward trend between velocity dispersion and mass as well as a $\sim$0.4 dex separation at fixed velocity dispersion between red and blue group centrals.

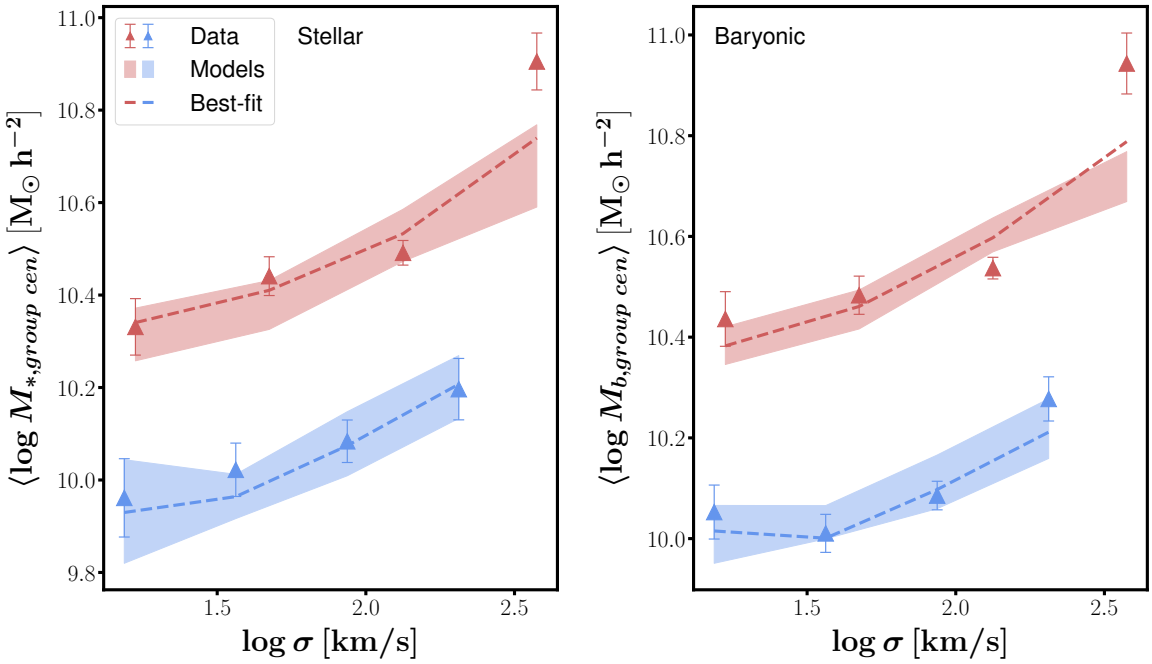

Figure 2.10: Average group central stellar mass as a function of group velocity dispersion (*left panel*) and average group central baryonic mass as a function of group velocity dispersion (*right panel*) for the stellar and baryonic quenching models where the models are jointly fit to all four observables. Points, error bars, dashed lines and shaded regions have the same meaning as in Fig. 2.3. The colours represent groups with red and blue centrals. The models shown here do not include PCA. Bin centers are plotted.

2.8.1.4 Velocity dispersion as a function of group central stellar/baryonic mass

Fig. 2.11 shows a comparison between our model predictions and ECO for velocity dispersion as a function of stellar and baryonic mass. The points, error bars, dashed lines, shaded regions and colours have the same meaning as in Fig. 2.10. Looking at the left panel first, the models follow the upward trend between velocity dispersion and mass and both the best-fit and distribution of 200 models show an offset at fixed stellar mass albeit not as strong of an offset as when velocity dispersion was the quantity that was fixed in Fig. 2.10. There is a significant amount of scatter in velocity dispersion at fixed stellar mass which likely comes from the fact that in a bin of stellar mass, there could be a range of halo masses and this mass mixing implies that smaller mass galaxies/halos are concentrated at the low mass end of the bin and higher mass galaxies/halos are concentrated at the high mass end of the bin. The smaller mass galaxies would be bluer than the higher mass galaxies in the same bin and this is contributing to the offset we are seeing.

The best-fit baryonic model in the panel on the right reproduces the data well with the exception of the lowest and highest mass blue bins that correspond to a baryonic mass range of $10^{9.0}$ - $10^{9.55}$ and $10^{10.65}$ - $10^{11.2}\,h^{-2}\mathrm{M}_{\odot}$. When conducting an experiment to see which observable contributes most to the $> 4\sigma$ tension in the baryonic model, we found that the velocity dispersion of groups with blue centrals contributes to the tension as much as the blue fraction of centrals from Fig. 2.9 and red group central baryonic mass from from Fig. 2.10. We find it interesting that the relation between velocity dispersion and blue group central mass as measured in ECO and mocks exhibits a crossover with that of red group central mass at high masses. In other words, for baryonic masses between $10^{9.0}$ and $10^{10.65}\,h^{-2}\mathrm{M}_{\odot}$, groups with red centrals correspond to a higher velocity dispersion but beyond $10^{10.65}\,h^{-2}\mathrm{M}_{\odot}$, groups with blue centrals (of which there are four) correspond to a higher velocity dispersion. Both red and blue baryonic relations have less scatter than those in the stellar model in the left panel (taking into account the difference in scales). Additionally, both the best-fit and distribution of 200 models show an offset at fixed baryonic

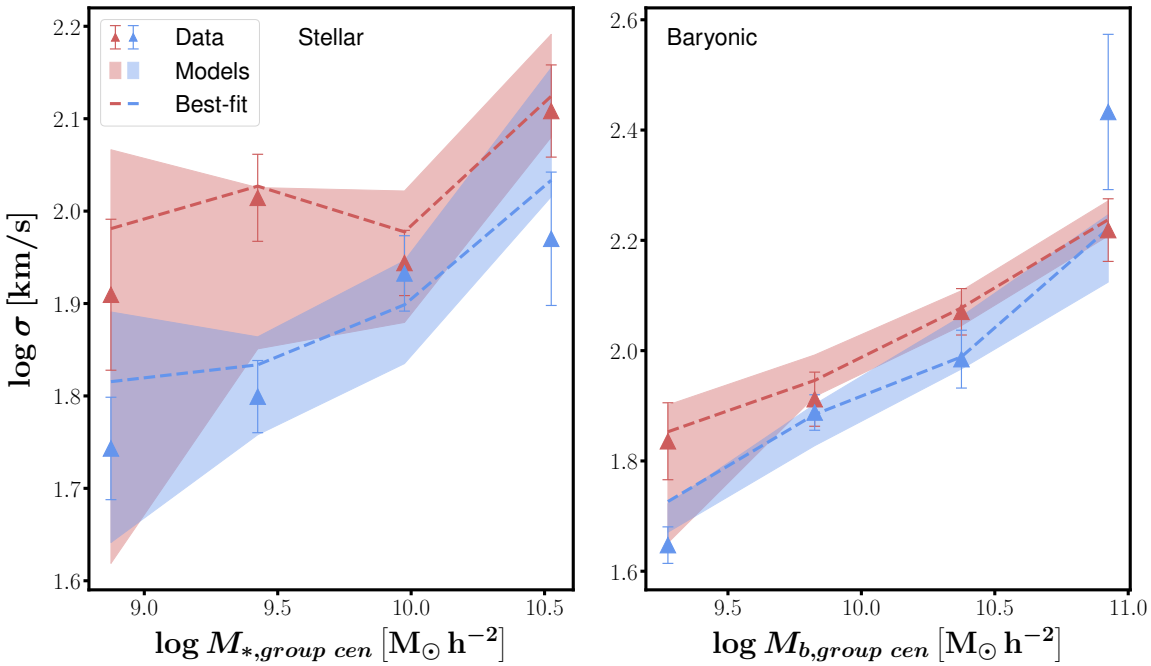

Figure 2.11: Velocity dispersion as a function of group central stellar mass (*left panel*) and as a function of group central baryonic mass (*right panel*) for the stellar and baryonic quenching models where the models are jointly fit to all four observables. Points, error bars, dashed lines and shaded regions have the same meaning as in Fig. 2.3. The colours represent groups with red and blue centrals. The models shown here do not include PCA. Bin centers are plotted.

mass.

2.8.2 Red fraction of true centrals

The red fraction can be interpreted as the probability of a galaxy being quenched. We remind the reader that this fraction, which is introduced in ZM16 as a proxy for quenching efficiency, is directly calculated as part of the stellar and baryonic quenching models. These models dictate that for centrals, it is their stellar/baryonic mass that determines their quenching. When it comes to the red fractions, there are two features of interest that are both also parameters of the model. The first is the pace at which galaxies become quenched, μ_{cen}, i.e how quickly the quenching efficiency increases as a function of mass. The second is the mass scale at which a certain percentage of galaxies are quenched, M^q_{cen}. Above this mass scale, quenched galaxies are more likely to dominate, since these galaxies have min-

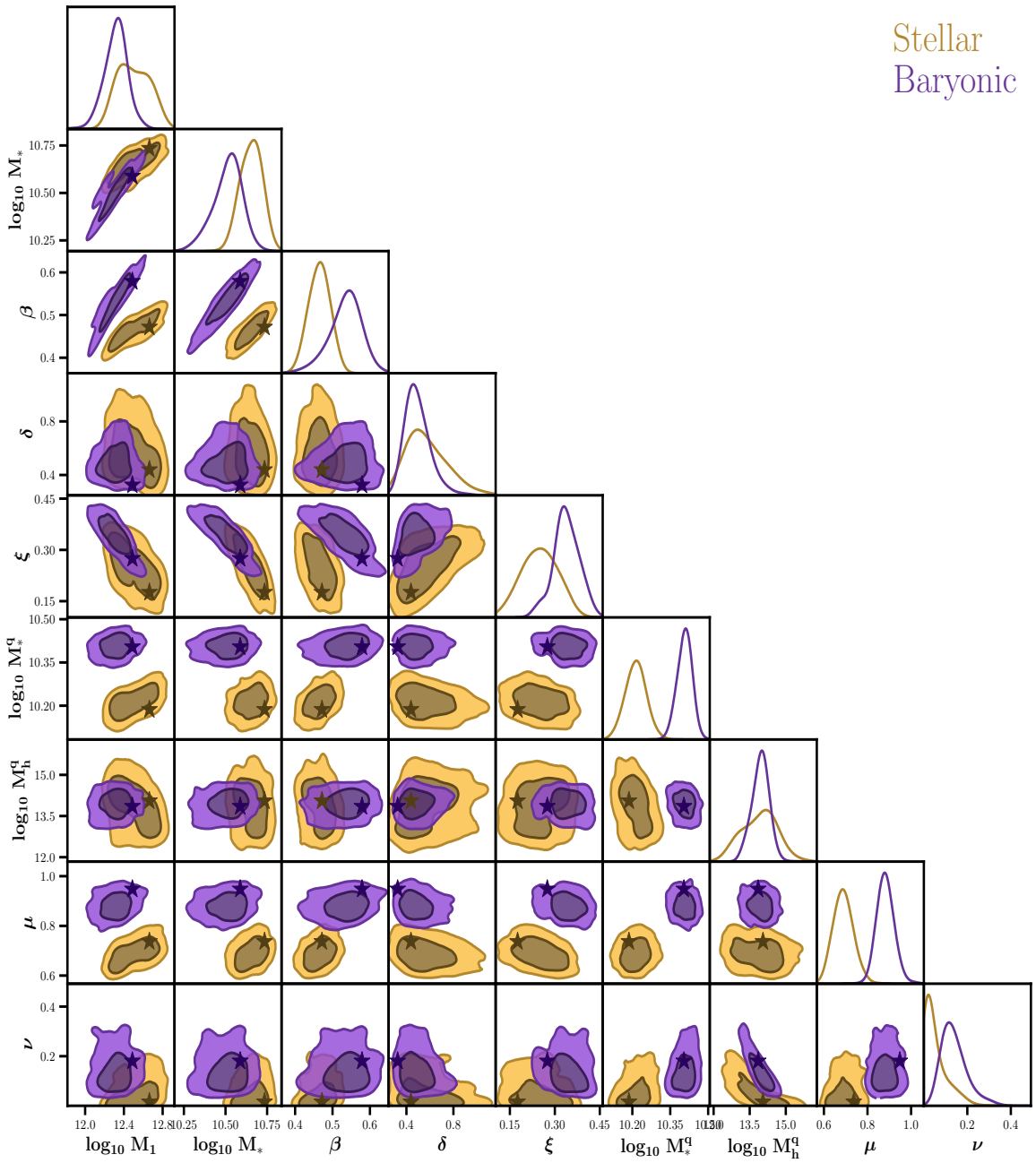

Figure 2.12: Posterior probability distributions and confidence regions for the 5 SHM-R/BHMR and 4 quenching parameters for the stellar and baryonic quenching models where the models are jointly fit to all four observables. The baryonic chain is shown in purple and the stellar chain in yellow. The histograms in the diagonal panels show the 1D posterior distributions of individual parameters. The off-diagonal panels contain 2D contours that show the region of parameter space that contains 68% (dark yellow and dark purple) and 95% (light yellow and light purple) of the MCMC probability for all pairwise combinations of the nine parameters. The yellow and the purple stars in the off-diagonal panels indicate the best-fit parameter values for the stellar and baryonic chain respectively. The models shown here do not include PCA.

imal cold gas reservoirs so their baryonic mass is roughly the same as their stellar mass. Below this point, star-forming galaxies are more likely to be the norm. This mass scale is similar to what was identified in (Kauffmann et al., 2003b; Kannappan et al., 2013) as the bimodality scale. They identified the bimodality scale with stellar mass $M_* \sim 10^{10.5}\,\mathrm{M}_\odot$ which corresponds to $\sim 10^{10.2}\,h^{-2}\mathrm{M}_\odot$. Using PCA, we find that the mass scale at which 50% of galaxies are quenched i.e red fraction of 0.5, is $M^q_{cen} = 10^{10.2}\,h^{-2}\mathrm{M}_\odot$. This is in perfect agreement with the aforementioned bimodality scale. Using PCA, we find the best-fit value of μ_{cen} to be 0.84 while the 68% confidence interval indicates a range of 0.69 - 0.79. Using the best-fit value of 0.84, this pace of quenching implies that the red fraction of galaxies rises from 10% at $\sim 10^{9.2}\,h^{-2}\mathrm{M}_\odot$ to 90% at $\sim 10^{10.8}\,h^{-2}\mathrm{M}_\odot$.

Fig. 2.13 shows our model predictions, both best-fit (yellow curve) as well as the subset of 200 models (purple curves), for the red fraction of true centrals as a function of both stellar and baryonic mass. Both the stellar and baryonic models predict very little scatter in this relation and both predict that the quenched fraction increases as a function of mass. In the left panel, we also provide comparisons with the semi-analytic model, Dark Sage (Stevens et al., 2016), the hydrodynamical simulation, TNG (Nelson et al., 2018), and the observational study of dust attenuation curves of 230,000 galaxies ranging from quiescent to star-forming performed in Salim et al. (2018). While there seems to be some overlap between the 1σ shaded region and TNG between $M_* \sim 10^{10.2} - 10^{11.0}\,h^{-2}\mathrm{M}_\odot$, that is the extent of the agreement. There is no agreement between our model predictions and Dark Sage and Salim et al. For comparison with theory, this could be due to differences in how stellar masses are calculated which would result in a stellar mass offset in the x-axis. For both theory and observational work, the differences could also be attributed to how quenching is defined. Also, AGN feedback in TNG is considered to be the main cause of star-formation shutting down and it occurs rapidly at a specific mass which would result in a sharp turnoff at low masses. We can see this in the behavior of the TNG relation and we find it is not consistent with our model prediction of a much more gradual cessation of

star-formation. Interestingly, Dark Sage and TNG also don't agree with each other.

For the baryonic model in the right panel of Fig. 2.13, the 68% confidence interval of μ_{cen} indicates a range of 0.69 - 0.79 which corresponds to the 68% confidence interval of μ_{cen} in the stellar model. Using PCA, the best-fit value of μ_{cen} of 0.97 indicates that the quenching efficiency increases with baryonic mass at a rate that is 15% faster than with stellar mass. In other words, it suggests that baryonic mass is more closely tied to the quenching of centrals than stellar mass. Using the best-fit value of 0.97, this pace of quenching implies that the red fraction of galaxies rises from 10% at $\sim 10^{9.2}\,h^{-2}\mathrm{M}_{\odot}$ to 90% at $\sim 10^{10.8}\,h^{-2}\mathrm{M}_{\odot}$. It is important to note, however, that the $p-$value associated with the baryonic model tells us that this model is less statistically probable than either stellar or halo.

According to the halo quenching model, the best-fit value of pace of μ_{cen} is 0.85, after having accounted for noise. This is similar to the pace predicted by the stellar model. The 68% confidence interval indicates a range of 0.45 - 0.82 which is much larger than for either the stellar or baryonic model. It seems to suggest that central quenching might not be as tightly coupled with halo mass as it is with either stellar mass or baryonic mass. Using the best-fit value of 0.85, this pace of quenching implies that the red fraction of galaxies rises from 10% at $\sim 10^{10.8}\,h^{-1}\mathrm{M}_{\odot}$ to 90% at $\sim 10^{12.4}\,h^{-1}\mathrm{M}_{\odot}$

An advantage of being able to measure red fractions for *true* centrals is that we can compare this to blue fractions of *group* centrals predicted in Fig. 2.9 to quantify the degree to which contamination occurs due to group finding. According to the best-fit model in Fig. 2.9, the blue fraction of group centrals at $M_* = 10^{9.0}\,h^{-2}\mathrm{M}_{\odot}$ is ~ 0.8 which corresponds to a predicted red fraction of group centrals of 0.2. From the left panel of Fig. 2.13, the predicted red fraction of true centrals is actually closer to 0.15 which is a 5% difference. Similarly, at a higher mass of $M_* = 10^{10.5}\,h^{-2}\mathrm{M}_{\odot}$ the blue fraction of group centrals at is ~ 0.2 which corresponds to a predicted red fraction of group centrals of 0.8. From the left panel of Fig. 2.13, the predicted red fraction of true centrals at that mass is 0.85

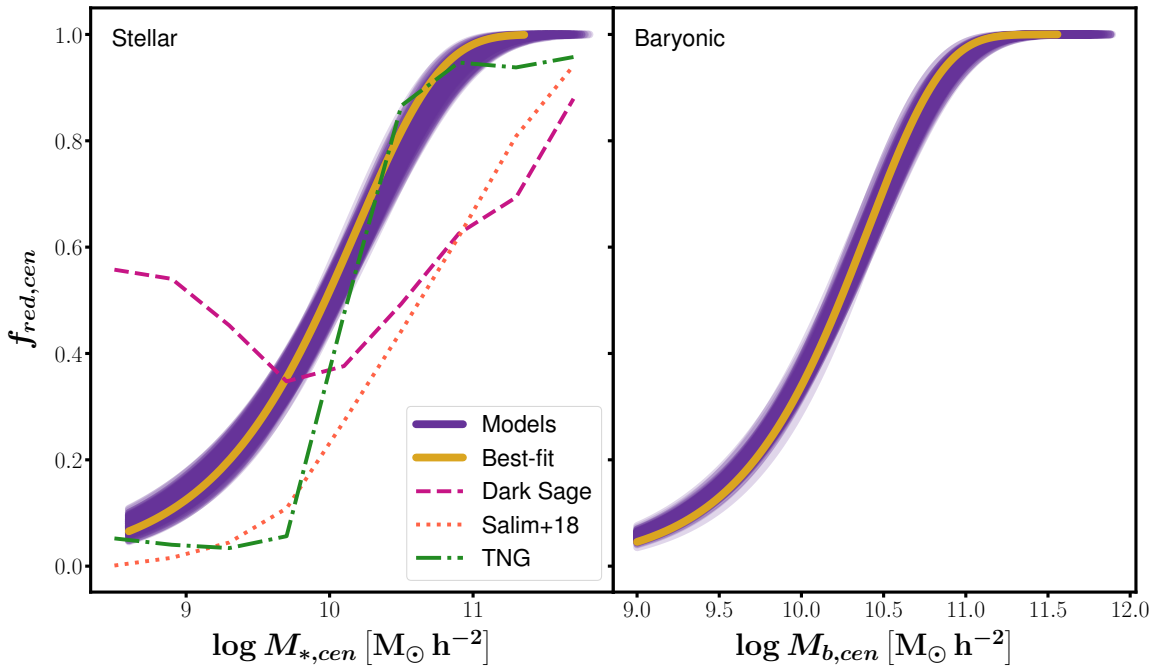

Figure 2.13: Red fractions of true centrals as a function of their stellar mass (*left panel*) and as a function of their baryonic mass (*right panel*) for the stellar and baryonic quenching models where the models are jointly fit to all four observables. The yellow curve represents the best-fit model and the purple curves represent the random subset of 200 models from the MCMC chain that correspond to a random sampling within the 68th percentile of the χ^2 distribution. In the left panel, we also show curves from Dark Sage (black dashed line), TNG (black dashed-dotted line) and (Salim et al., 2018) (black dotted line). The models shown here do not include PCA.

which is also a 5% difference. While this difference is small, it does indicate that satellites contaminate the central fraction when a group finder is applied.

2.8.3 Red fraction of true satellites

Fig. 2.14 shows our model predictions, both best-fit (yellow curve) as well as the subset of 200 models (purple curves), for the red fraction of true satellites as a function of both stellar and baryonic mass. We remind the reader that this fraction is directly calculated as part of the stellar and baryonic quenching models. These models dictate that for satellites, it is their stellar/baryonic mass along with their host halo mass that determines their quenching. The feature of interest, that is also one of the parameters of the ZM16 model, is the pace

at which satellites become quenched, μ_{sat}, i.e how quickly the quenching efficiency of satelltes increases as a function of stellar/baryonic mass. From Table 2.3, for the stellar model, after having accounted for noise, we find μ_{sat} to be 0.03 while the 68% confidence interval indicates a range of 0.12 - 0.21. Both the stellar and baryonic models predict more scatter in this relation than in that of centrals and both models predict that the quenched fraction increases as a function of mass.

What we find interesting in Fig. 2.14 is that our models predict a red fraction greater than 0.5 over the entire stellar/baryonic mass range of satellites. In other words, a satellite galaxy of stellar mass between $10^{8.6}$ and $10^{12.0}\,h^{-2}\mathrm{M}_{\odot}$ baryonic mass between $10^{9.0}$ and $10^{12.0}\,h^{-2}\mathrm{M}_{\odot}$ is predicted to be quenched $> 50\%$ of the time. This also means that satellites tend to be more quenched than centrals of the same stellar mass (Yang et al., 2003a; Peng et al., 2010; Wetzel et al., 2012, 2013; Wang et al., 2018c) and that this property extends to baryonic mass as well. In the left panel, we also provide comparisons with Dark Sage and TNG. While TNG captures the overall trend where more massive satellites have a higher tendency to be quenched than lower mass satellites, our predictions disagree when it comes to the pace of quenching as well as the probability of being quenched at stellar masses $< 10^{10.5}\,h^{-2}\mathrm{M}_{\odot}$. As for Dark Sage, while at stellar masses $\lesssim 10^{9.0}\,h^{-2}\mathrm{M}_{\odot}$ it too predicts a similar probability for the satellite to be quenched, it severely under predicts this probability for stellar masses $> 10^{9.0}\,h^{-2}\mathrm{M}_{\odot}$. As mentioned earlier, these differences could be due to how stellar masses are calculated which would result in a stellar mass offset in the x-axis for both theoretical works. Additionally, it could be due to differences in how quenching is defined. We see the same abrupt turn-on of satellite quenching in TNG as we did for centrals above and again, Dark Sage and TNG don't agree with each other.

For the baryonic model in the right panel of Fig. 2.14, the 68% confidence interval of μ_{sat} indicates a range of 0.15 - 0.25 which is similar to that from the stellar model. Given the best-fit model and using PCA, we find μ_{sat} to be 0.25, which indicates that the quenching efficiency as a function of baryonic mass is ~ 8 times greater than the quenching

efficiency as a function of stellar mass. This can be understood as a faster rate of quenching and it suggests that baryonic mass is more closely tied to the quenching of satellites than stellar mass. We remind the reader, however, that the $p-$value associated with the baryonic model tells us that this model is less statistically probable than either stellar or halo.

According to the halo quenching model and using PCA, we find μ_{sat} to be 0.79, which indicates that the quenching efficiency as a function of host halo mass is ~ 26 times greater and ~ 3 times greater than the quenching efficiency as a function of stellar and baryonic mass respectively. This can be understood as a faster rate of quenching and it suggests that host halo mass is much more closely tied to the quenching of satellites than their stellar mass. While this is true given the best-fit model to see the full picture, we need to turn to the 68% confidence interval which indicates a range of 0.19 - 0.76 which is much larger than for either the stellar or baryonic model. In other words, our model predicts a range of quenching efficiencies for satellites given their host halo mass.

Just as was done for true centrals, we use Fig. 2.9 to quantify the degree to which contamination occurs due to group finding. According to the best-fit model in Fig. 2.9, the blue fraction of group satellites at $M_* = 10^{9.0}\,h^{-2}\mathrm{M}_\odot$ is ~ 0.45 which corresponds to a predicted red fraction of group satellites of 0.55. From the left panel of Fig. 2.14, the predicted red fraction of true satellites is actually closer to 0.65 which is a 10% difference. Similarly, at a higher mass of $M_* = 10^{10.5}\,h^{-2}\mathrm{M}_\odot$ the blue fraction of group satellites at is ~ 0.15 which corresponds to a predicted red fraction of group satellites of 0.85. From the left panel of Fig. 2.14, the predicted red fraction of true satellites at that mass is closer 0.95 which is also a 10% difference. This indicates that centrals contaminate the satellites fraction when a group finder is applied. Moreover, the satellite fraction is more contaminated (10%) than the central fraction (5%).

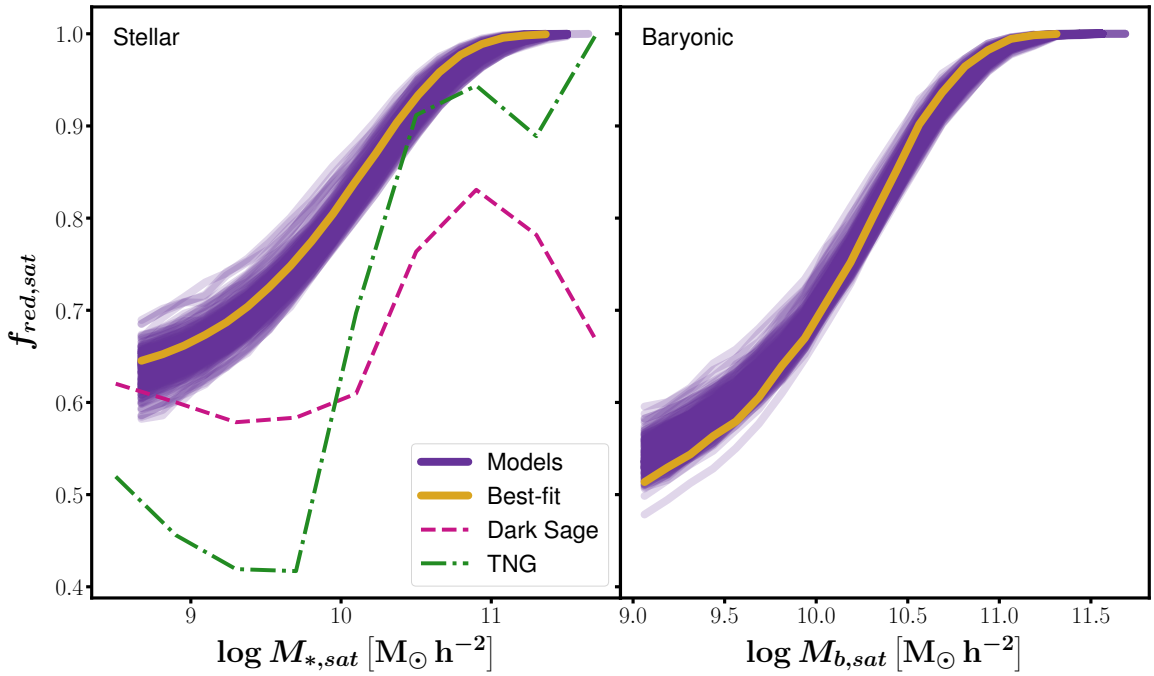

Figure 2.14: Red fractions of true satellites as a function of their stellar mass (*left panel*) and as a function of their baryonic mass (*right panel*) for the stellar and baryonic quenching models where the models are jointly fit to all four observables. The yellow curve represents the best-fit model and the purple curves represent the random subset of 200 models from the MCMC chain that correspond to a random sampling within the 68th percentile of the χ^2 distribution. In the left panel, both sets of curves are average red fractions calculated in 25 evenly spaced logarithmic bins of stellar mass between $10^{8.6}$ and $10^{12.0}\,h^{-2}\mathrm{M}_\odot$. In this panel, we also show curves from Dark Sage (black dashed line) and TNG (black dashed-dotted line). In the right panel, both sets of curves are average red fractions calculated in 25 evenly spaced logarithmic bins of baryonic mass between $10^{9.0}$ and $10^{12.0}\,h^{-2}\mathrm{M}_\odot$. The models shown here do not include PCA. Bin centers are plotted.

2.8.4 Total stellar- and baryonic-to-halo mass relations

For the purpose of comparing our SHMR to those from literature, we show the *parameterized* (i.e. our model predictions here are analytical instead of predicted measurements from mocks we populated using parameters from the MCMC chain) stellar-to-halo and baryonic-to-halo mass relations for all galaxies in Fig. 2.15, both the best-fit (black solid line) as well as the subset of 200 models (grey shaded region). Table 2.3 shows the five best-fit parameter values for both stellar and baryonic relations. When accounting for noise, there are some differences between all five of the best-fit parameter values. However, when looking at Table 2.2, we find that the 68% confidence intervals are similar between the stellar and baryonic model. Both relations have a very similar shape in terms of the low-mass slope, β and the high-mass slope, δ. The constraint on the amount of scatter in both relations is also very similar with the median scatter being ~ 0.2. We remind the reader though, that the $p-value$ of the baryonic model, post-PCA, is much worse than the stellar model which implies that it does not explain the data as well.

In the left panel of Fig. 2.15, we compare our SHMR to that of RP17, M18 and B19. Such comparisons are not always straightforward as other papers might have made different assumptions about the cosmological model, the definition of halo mass or the definition of stellar mass. The assumptions used to derive stellar masses have not been adjusted. We have only corrected the masses such that they assume $h = H_0/(100km\ s^{-1}\ Mpc^{-1}) = 1.0$. We find that our model predictions agree well with all three SHMRs between halo massses of $10^{10.8}$ and $10^{11.8}\,h^{-1}\mathrm{M}_{\odot}$. The SHMR from RP17 diverges beyond this mass and predicts a higher value for the high-mass slope resulting in a difference of 0.25 dex at a halo mass of $10^{13.0}\,h^{-1}\mathrm{M}_{\odot}$. They estimated their SHMR as a function of redshift using SHAM and many observed SMFs. The SHMRs from M18 and B19 agree very well with our SHMR. B19 presented a method for determining galaxy star formation rates from their host halos potential well depths, redshifts and assembly histories. They used observed SMFs, specific and cosmic star formation rates, quenched fractions, UV luminosity functions, UV-stellar

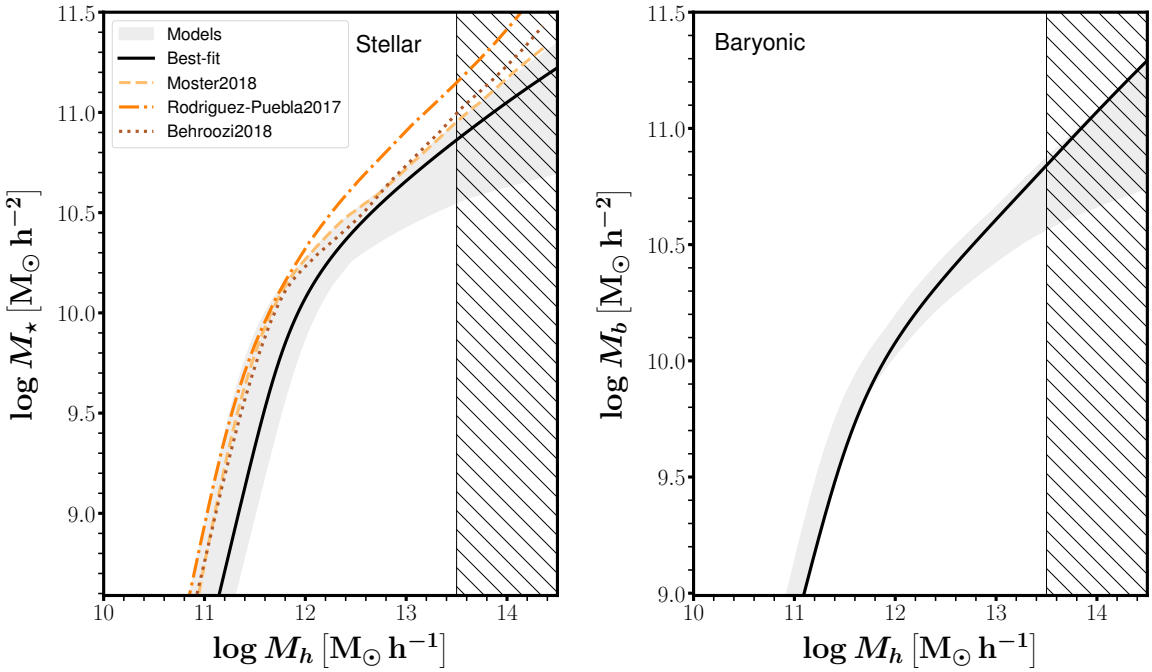

Figure 2.15: The parameterized stellar-to-halo (*left panel*) and baryonic-to-halo mass relation (*right panel*) for the stellar and baryonic quenching models where the models are jointly fit to all four observables. Solid lines represent the best-fit analytical model and the shaded regions have the same meaning as in Fig. 2.3 except they are shown here in analytical space rather than in mock space. The (*left panel*) also includes SHMRs from literature - B19 (brown dotted), RP17 (orange dashed-dotted) and M18 (yellow dashed). The models shown here do not include PCA. Bin centers are plotted.

mass relations, IRX-UV relations, auto- and cross- correlation functions and quenching dependence on environment to constrain their method from redshift 0 - 10. M18 developed an empirical model of galaxy formation where they assigned a star formation rate to each DM halo based on its growth rate and computed the stellar masses by integrating it. Several sets of observed data including (but not limited to) SMFs and sSFRs were used to constrain their method.

2.8.5 Stellar- and baryonic-to-halo mass relations split by star formation state

In Fig. 2.16 we show our model predictions for the stellar-to-halo and baryonic-to-halo mass relations split by star formation state for both best-fit models (solid lines) as well as the subset of 200 models (shaded regions). As expected, at fixed halo mass, more massive

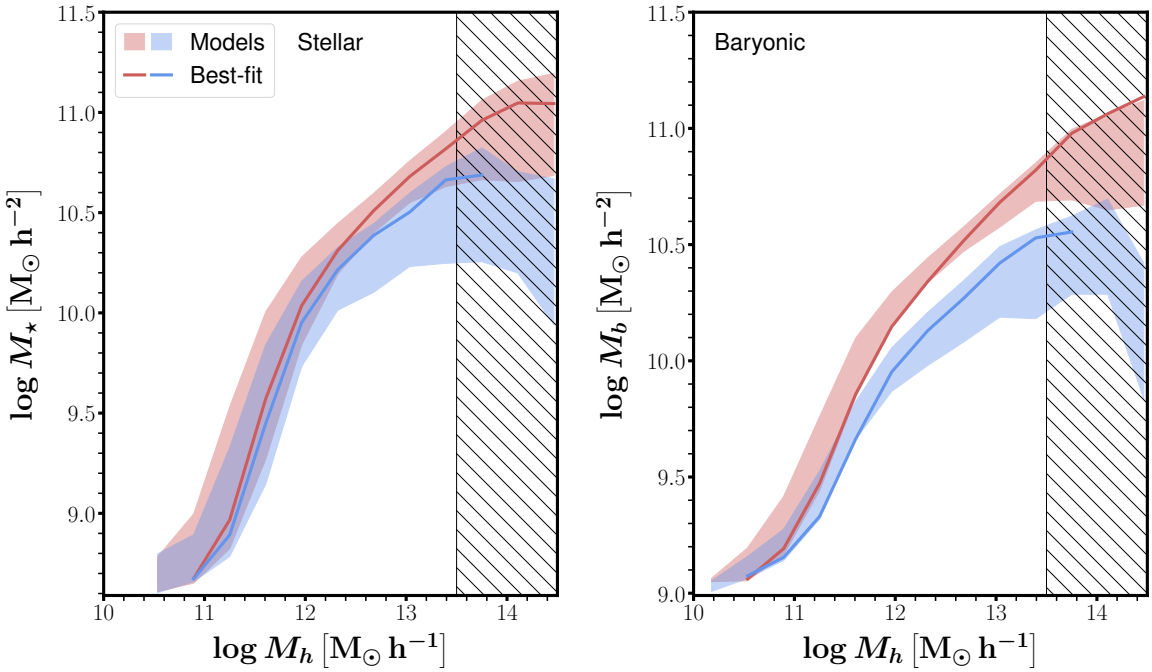

Figure 2.16: Similar to Fig. 2.15 but split by star-formation state where quenched galaxies are shown in red and star-forming galaxies are shown in blue. Bin centers are plotted.

galaxies are redder. There seems to be a degree of separation between the red SHMR and blue SHMR, for both the best-fit model as well as the full stellar mass distribution of red and blue galaxies at fixed halo mass. This separation increases as halo mass increases. At a halo mass of $10^{11.4}\,h^{-1}\mathrm{M}_\odot$, the separation between both best-fit relations is ~ 0.05 dex while at a halo mass of $10^{13.0}\,h^{-1}\mathrm{M}_\odot$ it grows to 0.2 dex. This separation becomes even more prominent in the BHMR. At a halo mass of $10^{11.4}\,h^{-1}\mathrm{M}_\odot$, the separation between both best-fit relations is ~ 0.2 dex while at a halo mass of $10^{13.0}\,h^{-1}\mathrm{M}_\odot$ it grows to 0.3 dex. The flattening of the mass relations at low halo masses is due to the fact that there is a stellar mass cut that is applied the mock that corresponds to the stellar and baryonic mass incompleteness of ECO. So in the lowest halo mass bin, galaxies below the cut are not included in the measurement of the mean stellar mass which results in an artificially higher mean.

We have repeatedly emphasized the fact that the baryonic model does not reproduce our data as well as both the stellar and halo models and one of the reasons for this could

be that the models that are used are not entirely descriptive of ECO. In other words, the SHMR model from B10 might not be able to fully capture the BHMR. It could also be that the quenching models from ZM16 aren't able to fully encapsulate how quenching depends on baryonic mass.

2.9 Summary and Conclusions

In this paper, we have adopted a Bayesian approach via MCMC to investigate the dependence of galaxy quenching on stellar, baryonic and halo mass using data from the ECO survey. We have done so by combining two empirical models: the parameterized model from B10 that we use for both stellar and baryonic mass, and both parameterized quenching models (hybrid and halo) from ZM16. The statistics we have used to constrain these models are the stellar/baryonic mass functions, the blue fractions of group centrals and satellites as a function of stellar/baryonic mass, group velocity dispersion as a function of average group central stellar/baryonic mass, and its converse, the average group central stellar/baryonic mass as a function of group velocity dispersion. These statistics were measured in ECO as well as in mock catalogues constructed by applying our empirical models to DM halos in a cosmological N-body simulation. We quantified errors and covariances using a separate suite of independent ECO mock catalogues and we used a PCA method to reduce the noise in our correlation matrix. Though we present both the raw and the PCA results, we draw our conclusions from the PCA MCMC chains where the noise has been mitigated, as these results (especially the $p-values$) are more reliable.

Our main results are as follows:

- By confronting the ZM16 quenching models against a suite of observational measurements from the ECO survey via our mock-based forward-modeling approach, we are able to constrain the quenched fractions of *true* centrals and satellites as a function of their stellar, baryonic, and host halo mass. In our best-fit models, we find that the mass scale at which 50% of true centrals are quenched is $M_* \sim 10^{10.2}\,h^{-2}\mathrm{M}_\odot$,

$M_b \sim 10^{10.2}\,h^{-2}\mathrm{M}_\odot$ and $M_h \sim 10^{11.8}\,h^{-1}\mathrm{M}_\odot$ for the stellar, baryonic, and halo models, respectively. Central galaxies above these masses are more likely to be quenched than not, while less massive galaxies are more likely to be star- forming. Our 50% stellar mass scale is in perfect agreement with the well-known Kauffmann et al. (2003b) bimodality scale of $10^{10.5}\,\mathrm{M}_\odot$[1]

- Our model constraints also reveal how quickly central galaxy quenching increases with mass through the μ_{cen} parameter. We find agreement in the values of this parameter among the stellar, baryonic, and halo quenching models. In our best-fit stellar quenching model, the fraction of red galaxies rises from 10% at $M_* \sim 10^{9.2}\,h^{-2}\mathrm{M}_\odot$ to 90% at $M_* \sim 10^{10.8}\,h^{-2}\mathrm{M}_\odot$. This mass range is similar for the baryonic model, while in the best-fit halo quenching model, the fraction of red galaxies rises from 10% at $M_h \sim 10^{10.8}\,h^{-1}\mathrm{M}_\odot$ to 90% at $M_h \sim 10^{12.4}\,h^{-1}\mathrm{M}_\odot$.

- The quenching model for satellite galaxies is more complex than that for centrals in the stellar and baryonic cases because the quenching probability includes a dependence on both stellar/baryonic and halo mass. In both cases, our best-fit models show that satellites are significantly more quenched than centrals at the same stellar/baryonic mass, with the difference being most prominent at the smallest masses. Indeed, at the low mass limit of our samples, we find that $\sim 60\%$ of satellites are red, compared to only $\sim 5\%$ of centrals. When we examine how quickly satellite quenching increases with mass, we find that stellar/baryonic mass has a bigger impact on the satellite quenching probability than does halo mass. This is evidenced by the significantly larger values of μ_{cen} compared to μ_{sat}[2] This is especially true in the best-fit stellar model, where the dependence halo mass is very weak. In contrast, in the best-fit halo quenching model, the quenching of satellites only depends on halo

[1]The difference between our numbers is due to our h units.

[2]Recall that in the ZM16 hybrid model, μ_{cen} dictates how fast the quenched fraction depends on stellar/baryonic mass for *both* centrals and satellites, while μ_{sat} controls the additional dependence of satellite quenching on halo mass.

mass and the value of μ_{sat} is almost as high as that of μ_{cen}.

- The stellar mass quenching model is the most successful at fitting all of the ECO statistics that we consider, with its best-fit model having a $p-value$ of 0.27. The halo mass quenching model is next, with a $p-value$ of 0.15. Though the stellar model is somewhat preferred over the halo one, both yield statistically acceptable fits to ECO data. In contrast, the baryonic quenching model has a best-fit $p-value$ of 2×10^{-3}, making it strongly disfavored relative to the other models.

- Though not the primary focus of this paper, our stellar model also constrains the stellar-to-halo mass relation (SHMR) for ECO galaxies. We find results consistent with other empirical measurements of the SHMR. Perhaps, more interestingly, our baryonic model constrains the baryonic-to-halo mass relation (BHMR), which is less well studied. We find that the scatter in the BHMR is the same as the scatter in the SHMR and is $\sim 0.2\pm0.05$ dex.

- The best-fit stellar quenching model predicts a separation between the SHMRs for red and blue true central galaxies, whereby red centrals reside in more massive halos on average than blue centrals at fixed stellar mass. This separation grows from $\sim$0.05 dex at a halo mass of $M_h \sim 10^{11.4}\,h^{-1}\mathrm{M}_\odot$ to $\sim$0.2 dex at a halo mass of $M_h \sim 10^{13.0}\,h^{-1}\mathrm{M}_\odot$. The separation between the BHMRs for red and blue central galaxies is even larger at all halo masses, growing from $\sim$0.2 dex at low mass to $\sim$0.3 dex at high mass. In the halo quenching model, there is no separation between the SHMRs for red and blue centrals, by construction. Since both the stellar and the halo quenching models yield acceptable fits to the ECO data, we cannot claim that we have detected a dependence of the SHMR on galaxy colour.

- By comparing the predicted quenched fractions of *true* centrals and satellites (Figs. 2.13 and 2.14) to the directly measured blue fractions of *group* centrals and satellites (Fig. 2.4), we are able to quantify the extent of contamination that occurs due to

errors in group finding. When measuring blue fractions of central/satellite galaxies that were identified using ECO groups, we underestimated the blue fractions of centrals by 5-10% and overestimated the blue fractions of satellites by 10-15%, relative to what the best-fit stellar quenching model reveals for true halo centrals/satellites. This is a natural consequence of central/satellite misidentification. Additionally, when measuring the large separation between the average stellar mass of red vs. blue group centrals at fixed velocity dispersion directly from ECO, as shown in the right panel of Fig. 2.2, we might naively conclude that quenching correlates with stellar mass at fixed halo mass. However, we have shown that this separation persists even in the halo quenching model, where the quenching prescription does not include stellar mass at all, and it is caused by the large scatter in the relationship between velocity dispersion and halo mass. The naive conclusion from Fig. 2.2 would thus have been incorrect. These examples demonstrate the value of adopting a forward modeling approach.

- When comparing our predicted red fraction of true centrals with results from the Dark Sage semi-analytic model and the Illustris-TNG hydrodynamic simulation, we find rough agreement with TNG at stellar masses greater than $M_* \sim 10^{10.2}\, h^{-2}\mathrm{M}_\odot$, but poor agreement with TNG at lower masses and poor agreement with Dark Sage at all masses. AGN feedback in TNG is assumed to be the main cause of star-formation shutting down and it occurs rapidly at a specific stellar mass, which results in a sharp upturn in red fraction near that mass. We can see this behavior in Figure 2.13 and we find that it is not consistent with our model fit to ECO, which reveals a more gradual transition from blue to red for central galaxies. The discrepancy between our empirical results and these galaxy formation models is even bigger in the case of true satellite galaxies. We find broadly no agreement with the exception that Dark Sage correctly predicts a red fraction of ~ 0.6 for low-mass satellites, and TNG correctly predicts that the most massive satellite galaxies are entirely quenched.

There are a few caveats with our analysis that we would like to mention. First, our estimate of the correlation matrix includes a source of stochasticity that is due to the fact that we have a limited number of mocks from which we calculate it. While the sole purpose of performing PCA was to account for this noise, having more mocks to measure our matrix from would further improve the accuracy with which we estimate the uncertainties in our observed measurements. Second, we treat subhalos as centrals when populating our mock universe by using the subhalo's mass at accretion, (M_{acc}). While this allows us to circumvent the issue of tidal stripping, where the subhalo is thought to lose a significant amount of its mass upon host halo entry, in doing so we ignore the fact that the galaxy also experiences stripping to an extent. However, Conroy et al. 2006 and Reddick et al. 2013 showed that the SHMR does not evolve significantly between prior- and post-infall. More importantly they showed that choosing today's subhalo mass to populate the subhalo instead of its M_{acc} is unable to reproduce galaxy clustering as well as when choosing M_{acc}. Lastly, while the majority of ECO consists of atomic gas content measurements, a percentage of measurements, where 21 cm detections were either too weak or badly confused, were replaced with photometric gas fractions (E15). This could affect some of our baryonic mass measurements and to quantify the effect on our constraints we would have to turn to RESOLVE-B, a different segment of the RESOLVE survey where all the gas measurements are real measurements i.e. none have been replaced with estimates from the photometric gas fraction technique. However, RESOLVE-B is ~ 32 times smaller in volume than ECO which means our RESOLVE-B measurements would be significantly more noisy.

We find it interesting that there is tension between ECO and the model where quenching depends on baryonic mass. One possible reason for this could be that the SHMR model from B10 or the quenching models from ZM16 (or a combination of the two) are not able to fully describe how baryonic mass depends on halo mass or how baryonic mass determines the quenching of centrals and satellites. This would imply that perhaps the analytical forms of the relations between baryonic mass and halo mass as well as between

baryonic mass and red fractions of centrals and satellites are different from their stellar counterparts. Alternatively, it is possible that the physical mechanisms that are responsible for quenching correlate more strongly with the stellar mass of central galaxies than they do with baryonic mass.

We find that the *hybrid* quenching model, where central galaxy quenching is driven by stellar mass and satellite quenching is driven by both stellar and halo mass, provides the best statistical fit to ECO data. This is different from ZM16, who concluded that the *halo* model, where quenching solely depends on halo mass, better explains the relationship between quenching and mass. There are many differences between our analyses that could be responsible for this different conclusion. ZM16 used SDSS data, a different definition of quenching that was based on $(g-r)$ colour, and they employed clustering and galaxy-galaxy lensing statistics to constrain their model. Additionally, ZM16 adopted an analytic halo model for calculating predicted statistics, in contrast to our fully numerical mock-based approach. Moreover, we find that the halo quenching model provides an acceptable fit to our data and is not ruled out, so there may actually be no tension between our analyses.

It is interesting to compare our results with those of M15, who also use the ECO survey for their analysis but with a direct approach using groups as proxies for halos. M15 found that the colour of group centrals depends on stellar/baryonic mass, with no dependence on group mass at fixed baryonic mass. For satellite galaxies, M15 found the opposite, i.e., that red satellites are found in more massive groups than blue satellites at fixed baryonic mass (Fig. 20 in M15). These findings are qualitatively consistent with the ZM16 hybrid quenching models that we use in this paper. However, we find that the halo quenching model, which has a different behavior from the M15 results, is also consistent with ECO data and so we are not in a position to decisively confirm the M15 result. There are several differences between the methodology employed by M15 and this paper. Most importantly, M15 used galaxy groups as a proxy for halos and estimated group mass from the total group luminosity, whereas we populate DM halos in a N-body simulation and use a variety

of statistics, including satellite kinematics, to constrain our models. It is interesting to further explore the differences between these two complementary approaches.

2.10 Acknowledgements

We would like to thank Duncan Campbell for providing the initial motivation for this research, Victor Calderon for providing code that was used to generate the mock galaxy catalogues to quantify errors in our analysis, Gillian Beltz-Mohrmann for providing us with simulation boxes used to make the aforementioned mock galaxy catalogues, Manodeep Sinha for providing us with the Vishnu simulation box used in our modeling procedure and Derrick Carr for providing red/blue ECO galaxy classification data as outlined in §2.2.

This research has made use of NASA's Astrophysics Data System; the `IPython` package (Pérez and Granger, 2007), `NumPy` (Harris et al., 2020), `SciPy` (Virtanen et al., 2020), `Pandas` (McKinney, 2010), `Matplotlib`, a Python library for publication quality graphics (Hunter, 2007), `Astropy` (Robitaille et al., 2013), `ChainConsumer` (Hinton, 2016), `emcee` (Foreman-Mackey et al., 2013) and `Halotools` (v0.7) code (Hearin et al., 2017).

The mock catalogues used to quantify errors in this paper were produced by the LasDamas project (http://lss.phy.vanderbilt.edu/lasdamas/); we thank NSF XSEDE for providing the computational resources for LasDamas. Some of the computational facilities used in this project were provided by the Vanderbilt Advanced Computing Center for Research and Education (ACCRE). Parts of this research were conducted by the Australian Research Council Centre of Excellence for All Sky Astrophysics in 3 Dimensions (ASTRO 3D), through project number CE170100013. SJK and ZLH acknowledge support from National Science Foundation (NSF) grant AST-1814486.

This research quite frequently sought Croton 2013 ("Damn You, Little h!"). Data compilations for other studies used in this paper were made much more efficient by the online `WebPlotDigitizer` (https://automeris.io/WebPlotDigitizer). These acknowledge-

ments were compiled using the Astronomy Acknowledgement Generator (http://astrofrog.github.io/acknowledgment-generator/).

CHAPTER 3

Summary and Outlook

3.1 Summary

In this dissertation, I have presented work that seeks to improve our understanding of the galaxy-halo connection by investigating the relationship between galaxy quenching and stellar, baryonic and halo mass in order to determine what mass quantity is more closely correlated with quenching. More specifically, we use two empirical models: a parameterized relation between stellar/baryonic mass and halo mass in the form of the stellar-to-halo/baryonic-to-halo mass relation and a parameterized relation between mass and quenching in the form of the hybrid and halo quenching models. By taking an empirical mock-based forward modeling approach, we are able to use a diverse combination of statistics to constrain these models. We use mock galaxy catalogues to quantify the uncertainties in the modeling procedure.

We find that the model where quenching of centrals and satellites depends on stellar mass with an additional satellite dependence on host halo mass provides the best fit to our data statistically, with a $p-$value of 0.27. The halo-driven quenching model also provides a statistically acceptable fit, with a $p-$value of 0.15. In other words, the hybrid stellar model is twice as probable as the halo-driven model. Based on our stellar model predictions, we identify the mass scale that divides predominantly star-forming galaxies from the quenched population to be $M_* \sim 10^{10.3}\, h^{-2}\mathrm{M}_\odot$ which is in perfect agreement with the bimodality scale of $M_* \sim 10^{10.5}\,\mathrm{M}_\odot$ identified in Kauffmann et al. 2003b and Kannappan et al. 2013 (the difference between our numbers is due to our h units). Lastly, we find tension at the $\sim 3\sigma$ level between ECO and the model where quenching depends instead on baryonic mass. With a $p-$value of 0.002, the hybrid baryonic model is 135 times and 75 times less probable than the hybrid stellar and halo-driven quenching models respectively.

3.2 Outlook

The study of the dependence of quenching on baryonic mass is one that is quite new. The tension that we find between our baryonic model and ECO could be due to either of (or the combination of) the two empirical models not being able to fully describe (i) the relation between halo mass and baryonic mass and (ii) how baryonic mass determines quenching of centrals and satellites. This might suggest the need for a model where the analytical forms of the relations between baryonic mass and halo mass as well as between baryonic mass and red fractions of centrals and satellites are different from their stellar counterparts. It could also be that quenching is tied to more things than just baryonic mass and a secondary matching between galaxy colour and another galaxy/halo property is required. Alternatively, it is also possible that the physical mechanisms that correlate with quenching do so more strongly with the stellar mass of galaxies than they do with baryonic mass.

References

Ade, P. A., Aghanim, N., Arnaud, M., Ashdown, M., Aumont, J., Baccigalupi, C., Banday, A. J., Barreiro, R. B., Bartlett, J. G., Bartolo, N., Battaner, E., Battye, R., Benabed, K., Benoît, A., Benoit-Lévy, A., Bernard, J. P., Bersanelli, M., Bielewicz, P., Bock, J. J., Bonaldi, A., Bonavera, L., Bond, J. R., Borrill, J., Bouchet, F. R., Boulanger, F., Bucher, M., Burigana, C., Butler, R. C., Calabrese, E., Cardoso, J. F., Catalano, A., Challinor, A., Chamballu, A., Chary, R. R., Chiang, H. C., Chluba, J., Christensen, P. R., Church, S., Clements, D. L., Colombi, S., Colombo, L. P., Combet, C., Coulais, A., Crill, B. P., Curto, A., Cuttaia, F., Danese, L., Davies, R. D., Davis, R. J., De Bernardis, P., De Rosa, A., De Zotti, G., Delabrouille, J., Désert, F. X., Di Valentino, E., Dickinson, C., Diego, J. M., Dolag, K., Dole, H., Donzelli, S., Doré, O., Douspis, M., Ducout, A., Dunkley, J., Dupac, X., Efstathiou, G., Elsner, F., Enßlin, T. A., Eriksen, H. K., Farhang, M., Fergusson, J., Finelli, F., Forni, O., Frailis, M., Fraisse, A. A., Franceschi, E., Frejsel, A., Galeotta, S., Galli, S., Ganga, K., Gauthier, C., Gerbino, M., Ghosh, T., Giard, M., Giraud-Héraud, Y., Giusarma, E., Gjerløw, E., González-Nuevo, J., Górski, K. M., Gratton, S., Gregorio, A., Gruppuso, A., Gudmundsson, J. E., Hamann, J., Hansen, F. K., Hanson, D., Harrison, D. L., Helou, G., Henrot-Versillé, S., Hernández-Monteagudo, C., Herranz, D., Hildebrandt, S. R., Hivon, E., Hobson, M., Holmes, W. A., Hornstrup, A., Hovest, W., Huang, Z., Huffenberger, K. M., Hurier, G., Jaffe, A. H., Jaffe, T. R., Jones, W. C., Juvela, M., Keihänen, E., Keskitalo, R., Kisner, T. S., Kneissl, R., Knoche, J., Knox, L., Kunz, M., Kurki-Suonio, H., Lagache, G., Lähteenmäki, A., Lamarre, J. M., Lasenby, A., Lattanzi, M., Lawrence, C. R., Leahy, J. P., Leonardi, R., Lesgourgues, J., Levrier, F., Lewis, A., Liguori, M., Lilje, P. B., Linden-Vørnle, M., López-Caniego, M., Lubin, P. M., Maciás-Pérez, J. F., Maggio, G., Maino, D., Mandolesi, N., Mangilli, A., Marchini, A., Maris, M., Martin, P. G., Martinelli, M., Martínez-González, E., Masi, S., Matarrese, S., Mcgehee, P., Meinhold, P. R., Melchiorri, A., Melin, J. B., Mendes, L., Mennella, A., Migliaccio, M., Millea, M., Mitra, S., Miville-Deschênes, M. A., Moneti, A., Montier, L., Morgante, G., Mortlock, D., Moss, A., Munshi, D., Murphy, J. A., Naselsky, P., Nati, F., Natoli, P., Netterfield, C. B., Nørgaard-Nielsen, H. U., Noviello, F., Novikov, D., Novikov, I., Oxborrow, C. A., Paci, F., Pagano, L., Pajot, F., Paladini, R., Paoletti, D., Partridge, B., Pasian, F., Patanchon, G., Pearson, T. J., Perdereau, O., Perotto, L., Perrotta, F., Pettorino, V., Piacentini, F., Piat, M., Pierpaoli, E., Pietrobon, D., Plaszczynski, S., Pointecouteau, E., Polenta, G., Popa, L., Pratt, G. W., Prézeau, G., Prunet, S., Puget, J. L., Rachen, J. P., Reach, W. T., Rebolo, R., Reinecke, M., Remazeilles, M., Renault, C., Renzi, A., Ristorcelli, I., Rocha, G., Rosset, C., Rossetti, M., Roudier, G., Rouillé D'orfeuil, B., Rowan-Robinson, M., Rubinõ-Martín, J. A., Rusholme, B., Said, N., Salvatelli, V., Salvati, L., Sandri, M., Santos, D., Savelainen, M., Savini, G., Scott, D., Seiffert, M. D., Serra, P., Shellard, E. P., Spencer, L. D., Spinelli, M., Stolyarov, V., Stompor, R., Sudiwala, R., Sunyaev, R., Sutton, D., Suur-Uski, A. S., Sygnet, J. F., Tauber, J. A., Terenzi, L., Toffolatti, L., Tomasi, M., Tristram, M., Trombetti, T., Tucci, M., Tuovinen, J., Türler, M., Umana, G., Valenziano, L., Valiviita, J., Van Tent, F., Vielva, P., Villa, F., Wade, L. A., Wandelt, B. D., Wehus, I. K., White, M., White, S. D., Wilkinson, A., Yvon, D., Zacchei, A., and Zonca, A. (2016a). Planck 2015

results: XIII. Cosmological parameters. *Astronomy and Astrophysics*, 594:A13.

Ade, P. A., Aghanim, N., Arnaud, M., Ashdown, M., Aumont, J., Baccigalupi, C., Banday, A. J., Barreiro, R. B., Bartlett, J. G., Bartolo, N., Battaner, E., Battye, R., Benabed, K., Benoît, A., Benoit-Lévy, A., Bernard, J. P., Bersanelli, M., Bielewicz, P., Bock, J. J., Bonaldi, A., Bonavera, L., Bond, J. R., Borrill, J., Bouchet, F. R., Boulanger, F., Bucher, M., Burigana, C., Butler, R. C., Calabrese, E., Cardoso, J. F., Catalano, A., Challinor, A., Chamballu, A., Chary, R. R., Chiang, H. C., Chluba, J., Christensen, P. R., Church, S., Clements, D. L., Colombi, S., Colombo, L. P., Combet, C., Coulais, A., Crill, B. P., Curto, A., Cuttaia, F., Danese, L., Davies, R. D., Davis, R. J., De Bernardis, P., De Rosa, A., De Zotti, G., Delabrouille, J., Désert, F. X., Di Valentino, E., Dickinson, C., Diego, J. M., Dolag, K., Dole, H., Donzelli, S., Doré, O., Douspis, M., Ducout, A., Dunkley, J., Dupac, X., Efstathiou, G., Elsner, F., Enßlin, T. A., Eriksen, H. K., Farhang, M., Fergusson, J., Finelli, F., Forni, O., Frailis, M., Fraisse, A. A., Franceschi, E., Frejsel, A., Galeotta, S., Galli, S., Ganga, K., Gauthier, C., Gerbino, M., Ghosh, T., Giard, M., Giraud-Héraud, Y., Giusarma, E., Gjerløw, E., González-Nuevo, J., Górski, K. M., Gratton, S., Gregorio, A., Gruppuso, A., Gudmundsson, J. E., Hamann, J., Hansen, F. K., Hanson, D., Harrison, D. L., Helou, G., Henrot-Versillé, S., Hernández-Monteagudo, C., Herranz, D., Hildebrandt, S. R., Hivon, E., Hobson, M., Holmes, W. A., Hornstrup, A., Hovest, W., Huang, Z., Huffenberger, K. M., Hurier, G., Jaffe, A. H., Jaffe, T. R., Jones, W. C., Juvela, M., Keihänen, E., Keskitalo, R., Kisner, T. S., Kneissl, R., Knoche, J., Knox, L., Kunz, M., Kurki-Suonio, H., Lagache, G., Lähteenmäki, A., Lamarre, J. M., Lasenby, A., Lattanzi, M., Lawrence, C. R., Leahy, J. P., Leonardi, R., Lesgourgues, J., Levrier, F., Lewis, A., Liguori, M., Lilje, P. B., Linden-Vørnle, M., López-Caniego, M., Lubin, P. M., Maciás-Pérez, J. F., Maggio, G., Maino, D., Mandolesi, N., Mangilli, A., Marchini, A., Maris, M., Martin, P. G., Martinelli, M., Martínez-González, E., Masi, S., Matarrese, S., Mcgehee, P., Meinhold, P. R., Melchiorri, A., Melin, J. B., Mendes, L., Mennella, A., Migliaccio, M., Millea, M., Mitra, S., Miville-Deschênes, M. A., Moneti, A., Montier, L., Morgante, G., Mortlock, D., Moss, A., Munshi, D., Murphy, J. A., Naselsky, P., Nati, F., Natoli, P., Netterfield, C. B., Nørgaard-Nielsen, H. U., Noviello, F., Novikov, D., Novikov, I., Oxborrow, C. A., Paci, F., Pagano, L., Pajot, F., Paladini, R., Paoletti, D., Partridge, B., Pasian, F., Patanchon, G., Pearson, T. J., Perdereau, O., Perotto, L., Perrotta, F., Pettorino, V., Piacentini, F., Piat, M., Pierpaoli, E., Pietrobon, D., Plaszczynski, S., Pointecouteau, E., Polenta, G., Popa, L., Pratt, G. W., Prézeau, G., Prunet, S., Puget, J. L., Rachen, J. P., Reach, W. T., Rebolo, R., Reinecke, M., Remazeilles, M., Renault, C., Renzi, A., Ristorcelli, I., Rocha, G., Rosset, C., Rossetti, M., Roudier, G., Rouillé D'orfeuil, B., Rowan-Robinson, M., Rubinõ-Martín, J. A., Rusholme, B., Said, N., Salvatelli, V., Salvati, L., Sandri, M., Santos, D., Savelainen, M., Savini, G., Scott, D., Seiffert, M. D., Serra, P., Shellard, E. P., Spencer, L. D., Spinelli, M., Stolyarov, V., Stompor, R., Sudiwala, R., Sunyaev, R., Sutton, D., Suur-Uski, A. S., Sygnet, J. F., Tauber, J. A., Terenzi, L., Toffolatti, L., Tomasi, M., Tristram, M., Trombetti, T., Tucci, M., Tuovinen, J., Türler, M., Umana, G., Valenziano, L., Valiviita, J., Van Tent, F., Vielva, P., Villa, F., Wade, L. A., Wandelt, B. D., Wehus, I. K., White, M., White, S. D., Wilkinson, A., Yvon, D., Zacchei, A., and Zonca, A. (2016b). Planck 2015 results: XIII. Cosmological parameters. *Astronomy and Astrophysics*, 594.

Aghanim, N., Akrami, Y., Ashdown, M., Aumont, J., Baccigalupi, C., Ballardini, M., Banday, A. J., Barreiro, R. B., Bartolo, N., Basak, S., Battye, R., Benabed, K., Bernard, J. P., Bersanelli, M., Bielewicz, P., Bock, J. J., Bond, J. R., Borrill, J., Bouchet, F. R., Boulanger, F., Bucher, M., Burigana, C., Butler, R. C., Calabrese, E., Cardoso, J. F., Carron, J., Challinor, A., Chiang, H. C., Chluba, J., Colombo, L. P., Combet, C., Contreras, D., Crill, B. P., Cuttaia, F., De Bernardis, P., De Zotti, G., Delabrouille, J., Delouis, J. M., Di Valentino, E., Diego, J. M., Doré, O., Douspis, M., Ducout, A., Dupac, X., Dusini, S., Efstathiou, G., Elsner, F., Enßlin, T. A., Eriksen, H. K., Fantaye, Y., Farhang, M., Fergusson, J., Fernandez-Cobos, R., Finelli, F., Forastieri, F., Frailis, M., Fraisse, A. A., Franceschi, E., Frolov, A., Galeotta, S., Galli, S., Ganga, K., Génova-Santos, R. T., Gerbino, M., Ghosh, T., González-Nuevo, J., Górski, K. M., Gratton, S., Gruppuso, A., Gudmundsson, J. E., Hamann, J., Handley, W., Hansen, F. K., Herranz, D., Hildebrandt, S. R., Hivon, E., Huang, Z., Jaffe, A. H., Jones, W. C., Karakci, A., Keihänen, E., Keskitalo, R., Kiiveri, K., Kim, J., Kisner, T. S., Knox, L., Krachmalnicoff, N., Kunz, M., Kurki-Suonio, H., Lagache, G., Lamarre, J. M., Lasenby, A., Lattanzi, M., Lawrence, C. R., Le Jeune, M., Lemos, P., Lesgourgues, J., Levrier, F., Lewis, A., Liguori, M., Lilje, P. B., Lilley, M., Lindholm, V., López-Caniego, M., Lubin, P. M., Ma, Y. Z., Maciás-Pérez, J. F., Maggio, G., Maino, D., Mandolesi, N., Mangilli, A., Marcos-Caballero, A., Maris, M., Martin, P. G., Martinelli, M., Martínez-González, E., Matarrese, S., Mauri, N., McEwen, J. D., Meinhold, P. R., Melchiorri, A., Mennella, A., Migliaccio, M., Millea, M., Mitra, S., Miville-Deschênes, M. A., Molinari, D., Montier, L., Morgante, G., Moss, A., Natoli, P., Nørgaard-Nielsen, H. U., Pagano, L., Paoletti, D., Partridge, B., Patanchon, G., Peiris, H. V., Perrotta, F., Pettorino, V., Piacentini, F., Polastri, L., Polenta, G., Puget, J. L., Rachen, J. P., Reinecke, M., Remazeilles, M., Renzi, A., Rocha, G., Rosset, C., Roudier, G., Rubiño-Martín, J. A., Ruiz-Granados, B., Salvati, L., Sandri, M., Savelainen, M., Scott, D., Shellard, E. P., Sirignano, C., Sirri, G., Spencer, L. D., Sunyaev, R., Suur-Uski, A. S., Tauber, J. A., Tavagnacco, D., Tenti, M., Toffolatti, L., Tomasi, M., Trombetti, T., Valenziano, L., Valiviita, J., Van Tent, B., Vibert, L., Vielva, P., Villa, F., Vittorio, N., Wandelt, B. D., Wehus, I. K., White, M., White, S. D., Zacchei, A., and Zonca, A. (2018). Planck 2018 results. VI. Cosmological parameters. *Astronomy and Astrophysics*, 641.

Baldry, I. K., Balogh, M. L., Bower, R. G., Glazebrook, K., Nichol, R. C., Bamford, S. P., and Budavari, T. (2006). Galaxy bimodality versus stellar mass and environment. *Monthly Notices of the Royal Astronomical Society*, 373(2):469–483.

Baldry, I. K., Driver, S. P., Loveday, J., Taylor, E. N., Kelvin, L. S., Liske, J., Norberg, P., Robotham, A. S., Brough, S., Hopkins, A. M., Bamford, S. P., Peacock, J. A., Bland-Hawthorn, J., Conselice, C. J., Croom, S. M., Jones, D. H., Parkinson, H. R., Popescu, C. C., Prescott, M., Sharp, R. G., and Tuffs, R. J. (2012). Galaxy And Mass Assembly (GAMA): The galaxy stellar mass function at $z < 0.06$. *Monthly Notices of the Royal Astronomical Society*, 421(1):621–634.

Baldry, I. K., Glazebrook, K., Brinkmann, J., Ivezić, Ž., Lupton, R. H., Nichol, R. C., and Szalay, A. S. (2004). Quantifying the Bimodal Color-Magnitude Distribution of Galaxies. *The Astrophysical Journal*, 600(2):681–694.

Beers, T. C., Flynn, K., and Gebhardt, K. (1990). Measures of location and scale for velocities in clusters of galaxies - A robust approach. *The Astronomical Journal*, 100(1):32.

Behroozi, P., Wechsler, R. H., Hearin, A. P., and Conroy, C. (2019). Universemachine: The correlation between galaxy growth and dark matter halo assembly from z = 0-10. *Monthly Notices of the Royal Astronomical Society*, 488(3):3143–3194.

Behroozi, P. S., Conroy, C., and Wechsler, R. H. (2010). A comprehensive analysis of uncertainties affecting the stellar mass-halo mass relation for $0 < z < 4$. *Astrophysical Journal*, 717(1):379–403.

Behroozi, P. S., Wechsler, R. H., and Conroy, C. (2013a). The average star formation histories of galaxies in dark matter halos from z = 0-8. *Astrophysical Journal*, 770(1).

Behroozi, P. S., Wechsler, R. H., and Wu, H. Y. (2013b). The ROCKSTAR phase-space temporal halo finder and the velocity offsets of cluster cores. *Astrophysical Journal*, 762(2).

Bell, E. F., McIntosh, D. H., Katz, N., and Weinberg, M. D. (2003). The Optical and Near-Infrared Properties of Galaxies. I. Luminosity and Stellar Mass Functions. *The Astrophysical Journal Supplement Series*, 149(2):289–312.

Berlind, A. A., Frieman, J. A., Weinberg, D. H., Blanton, M. R., Warren, M. S., Abazajian, K., Scranton, R., Hogg, D. W., Scoccimarro, R., Bahcall, N. A., Brinkmann, J., Gott, J. R., Kleinman, S. J., Krzesinski, J., Lee, B. C., Miller, C. J., Nitta, A., Schneider, D. P., Tucker, D. L., and Zehavi, I. (2006). Percolation Galaxy Groups and Clusters in the SDSS Redshift Survey: Identification, Catalogs, and the Multiplicity Function. *The Astrophysical Journal Supplement Series*, 167(1):1–25.

Berlind, A. A. and Weinberg, D. H. (2002). The Halo Occupation Distribution: Toward an Empirical Determination of the Relation between Galaxies and Mass. *The Astrophysical Journal*, 575(2):587–616.

Bernardi, M., Meert, A., Sheth, R. K., Fischer, J. L., Huertas-Company, M., Maraston, C., Shankar, F., and Vikram, V. (2017). The high-mass end of the stellar mass function: dependence on stellar population models and agreement between fits to the light profile. *Monthly Notices of the Royal Astronomical Society*, 467(2):2217–2233.

Blanton, M. R., Schlegel, D. J., Strauss, M. A., Brinkmann, J., Finkbeiner, D., Fukugita, M., Gunn, J. E., Hogg, D. W., Ivezic, Z., Knapp, G. R., Lupton, R. H., Munn, J. A., Schneider, D. P., Tegmark, M., and Zehavi, I. (2004). NYU-VAGC: a galaxy catalog based on new public surveys. *AJ*, 129(6):2562–2578.

Bluck, A. F., Mendel, J. T., Ellison, S. L., Patton, D. R., Simard, L., Henriques, B. M., Torrey, P., Teimoorinia, H., Moreno, J., and Starkenburg, E. (2016). The impact of galactic properties and environment on the quenching of central and satellite galaxies: a comparison between SDSS, Illustris and L-Galaxies. *Monthly Notices of the Royal Astronomical Society*, 462(3):2559–2586.

Bluck, A. F., Trevor Mendel, J., Ellison, S. L., Moreno, J., Simard, L., Patton, D. R., and Starkenburg, E. (2014). Bulge mass is king: The dominant role of the bulge in determining the fraction of passive galaxies in the sloan digital sky survey. *Monthly Notices of the Royal Astronomical Society*, 441(1):599–629.

Blumenthal, G. R., Faber, S. M., Primack, J. R., and Rees, M. J. (1984). Formation of galaxies and large-scale structure with cold dark matter. *Nature 1984 311:5986*, 311(5986):517–525.

Bond, J. R., Kofman, L., and Pogosyan, D. (1996). How filaments of galaxies are woven into the cosmic web. *Nature*, 380(6575):603–606.

Brinchmann, J., Charlot, S., White, S. D., Tremonti, C., Kauffmann, G., Heckman, T., and Brinkmann, J. (2004). The physical properties of star-forming galaxies in the low-redshift Universe. *Monthly Notices of the Royal Astronomical Society*, 351(4):1151–1179.

Bullock, J. S., Wechsler, R. H., and Somerville, R. S. (2002). Galaxy halo occupation at high redshift. *Monthly Notices of the Royal Astronomical Society*, 329(1):246–256.

Cacciato, M., Van Den Bosch, F. C., More, S., Li, R., Mo, H. J., and Yang, X. (2009). Galaxy clustering and galaxy-galaxy lensing: A promising union to constrain cosmological parameters. *Monthly Notices of the Royal Astronomical Society*, 394(2):929–946.

Campbell, D., Van den Bosch, F. C., Hearin, A., Padmanabhan, N., Berlind, A., Mo, H. J., Tinker, J., and Yang, X. (2015). Assessing colour-dependent occupation statistics inferred from galaxy group catalogues. *Monthly Notices of the Royal Astronomical Society*, 452(1):444–469.

Carlberg, Yee, Ellingson, Abraham, Gravel, Morris, and Pritchet (1995). Galaxy Cluster Virial Masses and Omega. *ApJ*, 462:32.

Carretero, J., Castander, F. J., Gaztañaga, E., Crocce, M., and Fosalba, P. (2015). An algorithm to build mock galaxy catalogues using MICE simulations. *Monthly Notices of the Royal Astronomical Society*, 447(1):646–670.

Challinor, A. and Lewis, A. (2011). Linear power spectrum of observed source number counts. *Physical Review D - Particles, Fields, Gravitation and Cosmology*, 84(4):1–17.

Cole, S., Aragón-Salamanca, A., Frenk, C. S., Navarro, J. F., and Zepf, S. E. (1994). A recipe for galaxy formation. *Monthly Notices of the Royal Astronomical Society*, 271(4):781–806.

Colless, M., Dalton, G., Maddox, S., Sutherland, W., Norberg, P., Cole, S., Bland-Hawthorn, J., Bridges, T., Cannon, R., Collins, C., Couch, W., Cross, N., Deeley, K., De Propris, R., Driver, S. P., Efstathiou, G., Ellis, R. S., Frenk, C. S., Glazebrook, K., Jackson, C., Lahav, O., Lewis, I., Lumsden, S., Madgwick, D., Peacock, J. A., Peterson, B. A., Price, I., Seaborne, M., and Taylor, K. (2001). The 2dF Galaxy Redshift Survey:

Spectra and redshifts. *Monthly Notices of the Royal Astronomical Society*, 328(4):1039–1063.

Conroy, C., Prada, F., Newman, J. A., Croton, D., Coil, A. L., Conselice, C. J., Cooper, M. C., Davis, M., Faber, S. M., Gerke, B. F., Guhathakurta, P., Klypin, A., Koo, D. C., and Yan, R. (2007). Evolution in the Halo Masses of Isolated Galaxies between z $\sim$ 1 and z $\sim$ 0: From DEEP2 to SDSS . *The Astrophysical Journal*, 654(1):153–171.

Conroy, C., Wechsler, R. H., and Kravtsov, A. V. (2006). Modeling Luminosity-dependent Galaxy Clustering through Cosmic Time. *The Astrophysical Journal*, 647(1):201–214.

Contini, E., Gu, Q., Ge, X., Rhee, J., Yi, S. K., and Kang, X. (2020). The Roles of Mass and Environment in the Quenching of Galaxies. II. *The Astrophysical Journal*, 889(2):156.

Contini, E., Kang, X., Romeo, A. D., and Xia, Q. (2017). Constraints on the Evolution of the Galaxy Stellar Mass Function. I. Role of Star Formation, Mergers, and Stellar Stripping. *The Astrophysical Journal*, 837(1):27.

Cooray, A. and Sheth, R. (2002). Halo models of large scale structure. *Physics Report*, 372(1):1–129.

Crocce, M., Pueblas, S., and Scoccimarro, R. (2006). Transients from initial conditions in cosmological simulations. *Monthly Notices of the Royal Astronomical Society*, 373(1):369–381.

Croton, D. J. (2013). Damn You, Little h! (Or, Real-World Applications of the Hubble Constant Using Observed and Simulated Data). *Publications of the Astronomical Society of Australia*, 30(1):e052.

Croton, D. J., Stevens, A. R. H., Tonini, C., Garel, T., Bernyk, M., Bibiano, A., Hodkinson, L., Mutch, S. J., Poole, G. B., and Shattow, G. M. (2016). SEMI-ANALYTIC GALAXY EVOLUTION (SAGE): MODEL CALIBRATION AND BASIC RESULTS. *The Astrophysical Journal Supplement Series*, 222(2):22.

Davies, L. J. M., Robotham, A. S. G., Del, C., Lagos, P., Driver, S. P., Stevens, A. R. H., Davies, L. J. M. ., Bahé, Y. M., Alpaslan, M., Bremer, M. N., Brown, M. J. I., Brough, S., Bland-Hawthorn, J., Cortese, L., Elahi, P., Grootes, M. W., Holwerda, B. W., Ludlow, A. D., Mcgee, S., Owers, M., Phillipps, S., and Holwerda, B. W. (2018). Galaxy and Mass Assembly (GAMA): Environmental quenching of Galaxy and Mass Assembly (GAMA): Environmental quenching of centrals and satellites in groups centrals and satellites in groups ThinkIR Citation Galaxy And Mass Assembly (GAMA): Environmental Que. *MNRAS*, 000:1–16.

de Vaucouleurs, G. (1961). Integrated Colors of Bright Galaxies in the u, b, V System. *Astrophysical Journal Supplement, vol. 5, p.233*, 5:233.

Driver, S. P., Hill, D. T., Kelvin, L. S., Robotham, A. S., Liske, J., Norberg, P., Baldry, I. K., Bamford, S. P., Hopkins, A. M., Loveday, J., Peacock, J. A., Andrae, E., Bland-Hawthorn, J., Brough, S., Brown, M. J., Cameron, E., Ching, J. H., Colless, M., Conselice, C. J., Croom, S. M., Cross, N. J., De Propris, R., Dye, S., Drinkwater, M. J., Ellis, S., Graham, A. W., Grootes, M. W., Gunawardhana, M., Jones, D. H., van Kampen, E., Maraston, C., Nichol, R. C., Parkinson, H. R., Phillipps, S., Pimbblet, K., Popescu, C. C., Prescott, M., Roseboom, I. G., Sadler, E. M., Sansom, A. E., Sharp, R. G., Smith, D. J., Taylor, E., Thomas, D., Tuffs, R. J., Wijesinghe, D., Dunne, L., Frenk, C. S., Jarvis, M. J., Madore, B. F., Meyer, M. J., Seibert, M., Staveley-Smith, L., Sutherland, W. J., and Warren, S. J. (2011). Galaxy and Mass Assembly (GAMA): Survey diagnostics and core data release. *Monthly Notices of the Royal Astronomical Society*, 413(2):971–995.

Duarte, M. and Mamon, G. A. (2014). How well does the friends-of-friends algorithm recover group properties from galaxy catalogues limited in both distance and luminosity? *Monthly Notices of the Royal Astronomical Society*, 440(2):1763–1778.

Eckert, K. D., Kannappan, S. J., Lagos, C. D. P., Baker, A. D., Berlind, A. A., Stark, D. V., Moffett, A. J., Nasipak, Z., and Norris, M. A. (2017). The Baryonic Collapse Efficiency of Galaxy Groups in the RESOLVE and ECO Surveys. *The Astrophysical Journal*, 849(1):20.

Eckert, K. D., Kannappan, S. J., Stark, D. V., Moffett, A. J., Berlind, A. A., and Norris, M. A. (2016). RESOLVE AND ECO: THE HALO MASS-DEPENDENT SHAPE OF GALAXY STELLAR AND BARYONIC MASS FUNCTIONS. *The Astrophysical Journal*, 824(2):124.

Eckert, K. D., Kannappan, S. J., Stark, D. V., Moffett, A. J., Norris, M. A., Snyder, E. M., and Hoversten, E. A. (2015). RESOLVE SURVEY PHOTOMETRY and VOLUME-LIMITED CALIBRATION of the PHOTOMETRIC GAS FRACTIONS TECHNIQUE. *Astrophysical Journal*, 810(2):166.

Erickson, L. K., Gottesman, S. T., and Hunter, J. H. (1987). Mass distribution in spiral galaxies. *Natur*, 325(6107):779–782.

Falco, E. E., Kurtz, M. J., Geller, M. J., Huchra, J. P., Peters, J., Berlind, P., Mink, D. J., Tokarz, S. P., and Elwell, B. (1999). The Updated Zwicky Catalog (UZC). *Publications of the Astronomical Society of the Pacific*, 111(758):438–452.

Fall, S. M. and Efstathiou, G. (1980). 18 9F Mon. *Not. R. astr. Soc*, 193:189–206.

Foreman-Mackey, D., Hogg, D. W., Lang, D., and Goodman, J. (2013). emcee : The MCMC Hammer . *Publications of the Astronomical Society of the Pacific*, 125(925):306–312.

Girelli, G., Pozzetti, L., Bolzonella, M., Giocoli, C., Marulli, F., and Baldi, M. (2020). The stellar-to-halo mass relation over the past 12 Gyr - I. Standard ΛCDM model. *Astronomy & Astrophysics*, 634:A135.

Gonzalez-perez, V., Lacey, C. G., Baugh, C. M., Lagos, C. D., Helly, J., Campbell, D. J., and Mitchell, P. D. (2014). How sensitive are predicted galaxy luminosities to the choice of stellar population synthesis model? *Monthly Notices of the Royal Astronomical Society*, 439(1):264–283.

Gu, M., Conroy, C., and Behroozi, P. (2016). Hierarchical Galaxy Growth and Scatter in the Stellar Mass–Halo Mass Relation. *The Astrophysical Journal*, 833(1):2.

Guo, Q., White, S., Li, C., and Boylan-Kolchin, M. (2010). How do galaxies populate dark matter haloes? *Monthly Notices of the Royal Astronomical Society*, 404(3):1111–1120.

Guzik, J. and Seljak, U. (2002). Virial masses of galactic haloes from galaxy–galaxy lensing: theoretical modelling and application to Sloan Digital Sky Survey data. *Monthly Notices of the Royal Astronomical Society*, 335(2):311–324.

Hansen, S. M., Sheldon, E. S., Wechsler, R. H., and Koester, B. P. (2009). THE GALAXY CONTENT OF SDSS CLUSTERS AND GROUPS. *The Astrophysical Journal*, 699(2):1333.

Harris, C. R., Millman, K. J., van der Walt, S. J., Gommers, R., Virtanen, P., Cournapeau, D., Wieser, E., Taylor, J., Berg, S., Smith, N. J., Kern, R., Picus, M., Hoyer, S., van Kerkwijk, M. H., Brett, M., Haldane, A., del Río, J. F., Wiebe, M., Peterson, P., Gérard-Marchant, P., Sheppard, K., Reddy, T., Weckesser, W., Abbasi, H., Gohlke, C., and Oliphant, T. E. (2020). Array programming with NumPy. *Nature 2020 585:7825*, 585(7825):357–362.

Haynes, M. P., Giovanelli, R., Kent, B. R., Adams, E. A. K., Balonek, T. J., Craig, D. W., Fertig, D., Finn, R., Giovanardi, C., Hallenbeck, G., Hess, K. M., Hoffman, G. L., Huang, S., Jones, M. G., Koopmann, R. A., Kornreich, D. A., Leisman, L., Miller, J., Moorman, C., O'Connor, J., O'Donoghue, A., Papastergis, E., Troischt, P., Stark, D., and Xiao, L. (2018). The Arecibo Legacy Fast ALFA Survey: The ALFALFA Extragalactic H i Source Catalog. *The Astrophysical Journal*, 861(1):49.

Haynes, M. P., Giovanelli, R., Martin, A. M., Hess, K. M., Saintonge, A., Adams, E. A., Hallenbeck, G., Hoffman, G. L., Huang, S., Kent, B. R., Koopmann, R. A., Papastergis, E., Stierwalt, S., Balonek, T. J., Craig, D. W., Higdon, S. J., Kornreich, D. A., Miller, J. R., O'Donoghue, A. A., Olowin, R. P., Rosenberg, J. L., Spekkens, K., Troischt, P., and Wilcots, E. M. (2011). THE ARECIBO LEGACY FAST ALFA SURVEY: THE α.40 H i SOURCE CATALOG, ITS CHARACTERISTICS AND THEIR IMPACT ON THE DERIVATION OF THE H i MASS FUNCTION. *The Astronomical Journal*, 142(5):170.

Hearin, A. P., Campbell, D., Tollerud, E., Behroozi, P., Diemer, B., Goldbaum, N. J., Jennings, E., Leauthaud, A., Mao, Y.-Y., More, S., Parejko, J., Sinha, M., Sipöcz, B., and Zentner, A. (2017). Forward Modeling of Large-scale Structure: An Open-source Approach with Halotools. *The Astronomical Journal*, 154(5):190.

Hearin, A. P., Zentner, A. R., Berlind, A. A., and Newman, J. A. (2013). SHAM beyond clustering: New tests of galaxy-halo abundance matching with galaxy groups. *Monthly Notices of the Royal Astronomical Society*, 433(1):659–680.

Henriques, B. M., White, S. D., Thomas, P. A., Angulo, R., Guo, Q., Lemson, G., Springel, V., and Overzier, R. (2015). Galaxy formation in the Planck cosmology - I. Matching the observed evolution of star formation rates, colours and stellar masses. *Monthly Notices of the Royal Astronomical Society*, 451(3):2663–2680.

Hinton, S. (2016). ChainConsumer. *Journal of Open Source Software*, 1(4):45.

Huchra, J. P., Geller, M. J., de Lapparent, V., and Burg, R. (1988). The CFA Redshift Survey. *IAUS*, 130:105.

Hunter, J. D. (2007). Matplotlib: A 2D graphics environment. *Computing in Science and Engineering*, 9(3):90–95.

Jones, D. H., Read, M. A., Saunders, W., Colless, M., Jarrett, T., Parker, Q. A., Fairall, A. P., Mauch, T., Sadler, E. M., Watson, F. G., Burton, D., Campbell, L. A., Cass, P., Croom, S. M., Dawe, J., Fiegert, K., Frankcombe, L., Hartley, M., Huchra, J., James, D., Kirby, E., Lahav, O., Lucey, J., Mamon, G. A., Moore, L., Peterson, B. A., Prior, S., Proust, D., Russell, K., Safouris, V., Wakamatsu, K. I., Westra, E., and Williams, M. (2009). The 6dF Galaxy Survey: Final redshift release (DR3) and southern large-scale structures. *Monthly Notices of the Royal Astronomical Society*, 399(2):683–698.

Kannappan, S. J., Stark, D. V., Eckert, K. D., Moffett, A. J., Wei, L. H., Pisano, D. J., Baker, A. J., Vogel, S. N., Fabricant, D. G., Laine, S., Norris, M. A., Jogee, S., Lepore, N., Hough, L. E., and Weinberg-Wolf, J. (2013). Connecting transitions in galaxy properties to refueling. *Astrophysical Journal*, 777(1).

Kannappan, S. J., Wei, L. H., Kannappan, S. J., and Wei, L. H. (2008). Galaxy Gas Fractions, Characteristic Mass Scales, and the RESOLVE Survey. *AIPC*, 1035:163–168.

Katz, N., Weinberg, D. H., and Hernquist, L. (1995). Cosmological Simulations with TreeSPH. *ApJS*, 105:19.

Kauffmann, G., Heckman, T. M., White, S. D., Charlot, S., Tremonti, C., Brinchmann, J., Bruzual, G., Peng, E. W., Seibert, M., Bernardi, M., Blanton, M., Brinkmann, J., Castander, F., Csábai, I., Fukugita, M., Ivezic, Z., Munn, J. A., Nichol, R. C., Padmanabhan, N., Thakar, A. R., Weinberg, D. H., and York, D. (2003a). Stellar masses and star formation histories for 105 galaxies from the Sloan Digital Sky Survey. *Monthly Notices of the Royal Astronomical Society*, 341(1):33–53.

Kauffmann, G., Heckman, T. M., White, S. D., Charlot, S., Tremonti, C., Peng, E. W., Seibert, M., Brinkmann, J., Nichol, R. C., SubbaRao, M., and York, D. (2003b). The dependence of star formation history and internal structure on stellar mass for 105 low-redshift galaxies. *Monthly Notices of the Royal Astronomical Society*, 341(1):54–69.

Kauffmann, G., White, S. D. M., Guiderdoni, B., Kauffmann, G., White, S. D. M., and Guiderdoni, B. (1993). The formation and evolution of galaxies within merging dark matter haloes. *MNRAS*, 264(1):201–218.

Klypin, A. A., Trujillo-Gomez, S., and Primack, J. (2011). Dark Matter Halos in the Standard Cosmological Model: Results from the Bolshoi Simulation. *ApJ*, 740(2):102.

Knobel, C., Lilly, S. J., Woo, J., and Kovač, K. (2015). QUENCHING OF STAR FORMATION IN SLOAN DIGITAL SKY SURVEY GROUPS: CENTRALS, SATELLITES, AND GALACTIC CONFORMITY. *The Astrophysical Journal*, 800(1):24.

Kravtsov, A. V., Berlind, A. A., Wechsler, R. H., Klypin, A. A., Gottlober, S., Allgood, B., and Primack, J. R. (2004). The Dark Side of the Halo Occupation Distribution. *The Astrophysical Journal*, 609(1):35–49.

Kravtsov, A. V., Vikhlinin, A. A., and Meshcheryakov, A. V. (2018). Stellar Mass—Halo Mass Relation and Star Formation Efficiency in High-Mass Halos. *Astronomy Letters*, 44(1):8–34.

Legrand, L., McCracken, H. J., Davidzon, I., Ilbert, O., Coupon, J., Aghanim, N., Douspis, M., Capak, P. L., Le Fèvre, O., and Milvang-Jensen, B. (2019). The COSMOS-UltraVISTA stellar-to-halo mass relationship: New insights on galaxy formation efficiency out to z ˜ 5. *Monthly Notices of the Royal Astronomical Society*, 486(4):5468–5481.

Li, C., Jing, Y. P., Mao, S., Han, J., Peng, Q., Yang, X., Mo, H. J., and Van Den Bosch, F. (2012). Internal kinematics of groups of galaxies in the Sloan digital sky survey data release 7. *Astrophysical Journal*, 758(1):50.

Li, C. and White, S. D. (2009). The distribution of stellar mass in the low-redshift Universe. *Monthly Notices of the Royal Astronomical Society*, 398(4):2177–2187.

Lin, Y. and Mohr, J. J. (2004). K -band Properties of Galaxy Clusters and Groups: Brightest Cluster Galaxies and Intracluster Light . *The Astrophysical Journal*, 617(2):879–895.

Lin, Y., Mohr, J. J., and Stanford, S. A. (2003). Near-Infrared Properties of Galaxy Clusters: Luminosity as a Binding Mass Predictor and the State of Cluster Baryons. *The Astrophysical Journal*, 591(2):749–763.

Lin, Y., Mohr, J. J., and Stanford, S. A. (2004). K -Band Properties of Galaxy Clusters and Groups: Luminosity Function, Radial Distribution, and Halo Occupation Number . *The Astrophysical Journal*, 610(2):745–761.

Mandelbaum, R., Seljak, U., Kauffmann, G., Hirata, C. M., and Brinkmann, J. (2005). Galaxy halo masses and satellite fractions from galaxy-galaxy lensing in the SDSS: stellar mass, luminosity, morphology, and environment dependencies. *MNRAS*, 368(2):715–731.

Mandelbaum, R., Seljak, U., Kauffmann, G., Hirata, C. M., and Brinkmann, J. (2006). Galaxy halo masses and satellite fractions from galaxy-galaxy lensing in the Sloan Digital Sky Survey: stellar mass, luminosity, morphology and environment dependencies. *MNRAS*, 368(2):715–731.

McAlpine, S., Helly, J. C., Schaller, M., Trayford, J. W., Qu, Y., Furlong, M., Bower, R. G., Crain, R. A., Schaye, J., Theuns, T., Dalla Vecchia, C., Frenk, C. S., McCarthy, I. G., Jenkins, A., Rosas-Guevara, Y., White, S. D., Baes, M., Camps, P., and Lemson, G. (2016). The eagle simulations of galaxy formation: Public release of halo and galaxy catalogues. *Astronomy and Computing*, 15:72–89.

McKinney, W. (2010). *Data Structures for Statistical Computing in Python*.

Moffett, A. J., Kannappan, S. J., Berlind, A. A., Eckert, K. D., Stark, D. V., Hendel, D., Norris, M. A., and Grogin, N. A. (2015). ECO and RESOLVE: Galaxy Disk Growth in Environmental Context. *The Astrophysical Journal*, 812(2):89.

More, S., Van Den Bosch, F. C., and Cacciato, M. (2009a). Satellite kinematics - I. A new method to constrain the halo mass-luminosity relation of central galaxies. *Monthly Notices of the Royal Astronomical Society*, 392(2):917–924.

More, S., Van Den Bosch, F. C., and Cacciato, M. (2009b). Satellite kinematics - I. A new method to constrain the halo mass-luminosity relation of central galaxies. *Monthly Notices of the Royal Astronomical Society*, 392(2):917–924.

More, S., Van Den Bosch, F. C., Cacciato, M., Mo, H. J., Yang, X., and Li, R. (2009c). Satellite kinematics - II. the halo mass-luminosity relation of central galaxies in SDSS. *Monthly Notices of the Royal Astronomical Society*, 392(2):801–816.

More, S., Van Den Bosch, F. C., Cacciato, M., Skibba, R., Mo, H. J., and Yang, X. (2011). Satellite kinematics - III. Halo masses of central galaxies in SDSS. *Monthly Notices of the Royal Astronomical Society*, 410(1):210–226.

Moster, B. P., Naab, T., and White, S. D. (2013). Galactic star formation and accretion histories from matching galaxies to dark matter haloes. *Monthly Notices of the Royal Astronomical Society*, 428(4):3121–3138.

Moster, B. P., Naab, T., and White, S. D. (2018). EMERGE - An empirical model for the formation of galaxies since z ˜ 10. *Monthly Notices of the Royal Astronomical Society*, 477(2):1822–1852.

Moster, B. P., Somerville, R. S., Maulbetsch, C., Van Den Bosch, F. C., MacCiò, A. V., Naab, T., and Oser, L. (2010). Constraints on the relationship between stellar mass and halo mass at low and high redshift. *Astrophysical Journal*, 710(2):903–923.

Nelson, D., Pillepich, A., Genel, S., Vogelsberger, M., Springel, V., Torrey, P., Rodriguez-Gomez, V., Sijacki, D., Snyder, G. F., Griffen, B., Marinacci, F., Blecha, L., Sales, L., Xu, D., and Hernquist, L. (2015). The illustris simulation: Public data release. *Astronomy and Computing*, 13:12–37.

Nelson, D., Springel, V., Pillepich, A., Rodriguez-Gomez, V., Torrey, P., Genel, S., Vogelsberger, M., Pakmor, R., Marinacci, F., Weinberger, R., Kelley, L., Lovell, M., Diemer, B., and Hernquist, L. (2018). The IllustrisTNG Simulations: Public Data Release. *Computational Astrophysics and Cosmology*, 6(1).

Pan, Z., Peng, Y., Zheng, X., Wang, J., and Kong, X. (2019). The Evolution of Baryonic Mass Function of Galaxies to z = 3. *The Astrophysical Journal Letters*, 885(1):L14.

Paturel, G., Petit, C., Prugniel, P., Theureau, G., Rousseau, J., Brouty, M., Dubois, P., Cambrésy, L., Paturel, G., Petit, C., Prugniel, P., Theureau, G., Rousseau, J., Brouty, M., Dubois, P., and Cambrésy, L. (2003). HYPERLEDA. I. Identification and designation of galaxies. *A&A*, 412(1):45–55.

Peacock, J. A. and Smith, R. E. (2000). Halo occupation numbers and galaxy bias. *Monthly Notices of the Royal Astronomical Society*, 318(4):1144–1156.

Peng, Y. J., Lilly, S. J., Kovač, K., Bolzonella, M., Pozzetti, L., Renzini, A., Zamorani, G., Ilbert, O., Knobel, C., Iovino, A., Maier, C., Cucciati, O., Tasca, L., Carollo, C. M., Silverman, J., Kampczyk, P., De Ravel, L., Sanders, D., Scoville, N., Contini, T., Mainieri, V., Scodeggio, M., Kneib, J. P., Le Fèvre, O., Bardelli, S., Bongiorno, A., Caputi, K., Coppa, G., De La Torre, S., Franzetti, P., Garilli, B., Lamareille, F., Le Borgne, J. F., Le Brun, V., Mignoli, M., Perez Montero, E., Pello, R., Ricciardelli, E., Tanaka, M., Tresse, L., Vergani, D., Welikala, N., Zucca, E., Oesch, P., Abbas, U., Barnes, L., Bordoloi, R., Bottini, D., Cappi, A., Cassata, P., Cimatti, A., Fumana, M., Hasinger, G., Koekemoer, A., Leauthaud, A., MacCagni, D., Marinoni, C., McCracken, H., Memeo, P., Meneux, B., Nair, P., Porciani, C., Presotto, V., and Scaramell, R. (2010). Mass and Environment as Drivers of Galaxy Evolution in SDSS and zCOSMOS and the Origin of the Schechter Function. *ApJ*, 721(1):193–221.

Peng, Y. J., Lilly, S. J., Renzini, A., and Carollo, M. (2012). Mass and environment as drivers of galaxy evolution. II. the quenching of satellite galaxies as the origin of environmental effects. *Astrophysical Journal*, 757(1):4.

Pérez, F. and Granger, B. E. (2007). IPython: A system for interactive scientific computing. *Computing in Science and Engineering*, 9(3):21–29.

Perlmutter, S., Aldering, G., Goldhaber, G., Knop, R. A., Nugent, P., Castro, P. G., Deustua, S., Fabbro, S., Goobar, A., Groom, D. E., Hook, I. M., Kim, A. G., Kim, M. Y., Lee, J. C., Nunes, N. J., Pain, R., Pennypacker, C. R., Quimby, R., Lidman, C., Ellis, R. S., Irwin, M., McMahon, R. G., Ruiz-Lapuente, P., Walton, N., Schaefer, B., Boyle, B. J., Filippenko, A. V., Matheson, T., Fruchter, A. S., Panagia, N., Newberg, H. J. M., Couch, W. J., and Project, T. S. C. (1999). Measurements of Ω and Λ from 42 High-Redshift Supernovae. *The Astrophysical Journal*, 517(2):565–586.

Prada, F., Vitvitska, M., Klypin, A., Holtzman, J. A., Schlegel, D. J., Grebel, E. K., Rix, H., Brinkmann, J., McKay, T. A., and Csabai, I. (2003). Observing the Dark Matter Density Profile of Isolated Galaxies. *The Astrophysical Journal*, 598(1):260–271.

Read, J. I. and Trentham, N. (2005). The baryonic mass function of galaxies. *Philosophical Transactions of the Royal Society A: Mathematical, Physical and Engineering Sciences*, 363(1837):2693–2710.

Reddick, R. M., Wechsler, R. H., Tinker, J. L., and Behroozi, P. S. (2013). The connection between galaxies and dark matter structures in the local universe. *Astrophysical Journal*, 771(1).

Riess, A. G., Filippenko, A. V., Challis, P., Clocchiatti, A., Diercks, A., Garnavich, P. M., Gilliland, R. L., Hogan, C. J., Jha, S., Kirshner, R. P., Leibundgut, B., Phillips, M. M., Reiss, D., Schmidt, B. P., Schommer, R. A., Smith, R. C., Spyromilio, J., Stubbs, C., Suntzeff, N. B., and Tonry, J. (1998). Observational Evidence from Supernovae for an Accelerating Universe and a Cosmological Constant. *The Astronomical Journal*, 116(3):1009–1038.

Robitaille, T. P., Tollerud, E. J., Greenfield, P., Droettboom, M., Bray, E., Aldcroft, T., Davis, M., Ginsburg, A., Price-Whelan, A. M., Kerzendorf, W. E., Conley, A., Crighton, N., Barbary, K., Muna, D., Ferguson, H., Grollier, F., Parikh, M. M., Nair, P. H., Günther, H. M., Deil, C., Woillez, J., Conseil, S., Kramer, R., Turner, J. E., Singer, L., Fox, R., Weaver, B. A., Zabalza, V., Edwards, Z. I., Azalee Bostroem, K., Burke, D. J., Casey, A. R., Crawford, S. M., Dencheva, N., Ely, J., Jenness, T., Labrie, K., Lim, P. L., Pierfederici, F., Pontzen, A., Ptak, A., Refsdal, B., Servillat, M., and Streicher, O. (2013). Astropy: A community Python package for astronomy. *Astronomy and Astrophysics*, 558:A33.

Rodriguez-Puebla, A., Primack, J. R., Avila-Reese, V., and Faber, S. M. (2017). The Galaxy-Halo Connection Over The Last 13.3 Gyrs. *MNRAS*, 470(1):651–687.

Rubin, V. C., Ford, W. K., J., and Thonnard, N. (1980). Rotational properties of 21 SC galaxies with a large range of luminosities and radii, from NGC 4605 (R=4kpc) to UGC 2885 (R=122kpc). *ApJ*, 238:471–487.

Salim, S., Boquien, M., and Lee, J. C. (2018). Dust Attenuation Curves in the Local Universe: Demographics and New Laws for Star-forming Galaxies and High-redshift Analogs. *The Astrophysical Journal*, 859(1):11.

Scoccimarro, R. (1998). Transients from initial conditions: A perturbative analysis. *Monthly Notices of the Royal Astronomical Society*, 299(4):1097–1118.

Seljak, U. (2000). Analytic model for galaxy and dark matter clustering. *Monthly Notices of the Royal Astronomical Society*, 318(1):203–213.

Shankar, F., Sonnenfeld, A., Mamon, G. A., Chae, K.-H., Gavazzi, R., Treu, T., Diemer, B., Nipoti, C., Buchan, S., Bernardi, M., Sheth, R., and Huertas-Company, M. (2017). Revisiting the Bulge–Halo Conspiracy. I. Dependence on Galaxy Properties and Halo Mass. *The Astrophysical Journal*, 840(1):34.

Sheldon, E. S., Johnston, D. E., Frieman, J. A., Scranton, R., McKay, T. A., Connolly, A. J., Budavari, T., Zehavi, I., Bahcall, N., Brinkmann, J., and Fukugita, M. (2003). The Galaxy-mass Correlation Function Measured from Weak Lensing in the SDSS. *AJ*, 127(5):2544–2564.

Sinha, M., Berlind, A. A., McBride, C. K., Scoccimarro, R., Piscionere, J. A., and Wibking, B. D. (2018). Towards accurate modelling of galaxy clustering on small scales: testing the standard ΛCDM + halo model. *Monthly Notices of the Royal Astronomical Society*, 478(1):1042–1064.

Somerville, R. S. and Primack, J. R. (1998). Semi-Analytic Modelling of Galaxy Formation: The Local Universe. *MNRAS*, 310(4):1087–1110.

Spergel, D. N., Verde, L., Peiris, H. V., Komatsu, E., Nolta, M. R., Bennett, C. L., Halpern, M., Hinshaw, G., Jarosik, N., Kogut, A., Limon, M., Meyer, S. S., Page, L., Tucker, G. S., Weiland, J. L., Wollack, E., and Wright, E. L. (2003). First-Year Wilkinson Microwave Anisotropy Probe (WMAP) Observations: Determination of Cosmological Parameters . *The Astrophysical Journal Supplement Series*, 148(1):175–194.

Springel, V. (2005). The cosmological simulation code GADGET-2. *Monthly Notices of the Royal Astronomical Society*, 364(4):1105–1134.

Springel, V. and Hernquist, L. (2002). Cosmological SPH simulations: A hybrid multiphase model for star formation. *MNRAS*, 339(2):289–311.

Springel, V., Yoshida, N., and White, S. D. (2001). GADGET: A code for collisionless and gasdynamical cosmological simulations. *New Astronomy*, 6(2):79–117.

Stark, D. V., Kannappan, S. J., Eckert, K. D., Florez, J., Hall, K. R., Watson, L. C., Hoversten, E. A., Burchett, J. N., Guynn, D. T., Baker, A. D., Moffett, A. J., Berlind, A. A., Norris, M. A., Haynes, M. P., Giovanelli, R., Leroy, A. K., Pisano, D. J., Wei, L. H., Gonzalez, R. E., and Calderon, V. F. (2016). THE RESOLVE SURVEY ATOMIC GAS CENSUS AND ENVIRONMENTAL INFLUENCES ON GALAXY GAS RESERVOIRS. *The Astrophysical Journal*, 832(2):126.

Stevens, A. R., Croton, D. J., and Mutch, S. J. (2016). Building disc structure and galaxy properties through angular momentum: The DARK SAGE semi-analytic model. *Monthly Notices of the Royal Astronomical Society*, 461(1):859–876.

Strateva, I., Ivezić, Ž., Knapp, G. R., Narayanan, V. K., Strauss, M. A., Gunn, J. E., Lupton, R. H., Schlegel, D., Bahcall, N. A., Brinkmann, J., Brunner, R. J., Budavári, T., Csabai, I., Castander, F. J., Doi, M., Fukugita, M., Győry, Z., Hamabe, M., Hennessy, G., Ichikawa, T., Kunszt, P. Z., Lamb, D. Q., McKay, T. A., Okamura, S., Racusin, J., Sekiguchi, M., Schneider, D. P., Shimasaku, K., and York, D. (2001). Color Separation of Galaxy Types in the Sloan Digital Sky Survey Imaging Data. *The Astronomical Journal*, 122(4):1861–1874.

Strauss, M. A., Weinberg, D. H., Lupton, R. H., Narayanan, V. K., Annis, J., Bernardi, M., Blanton, M., Burles, S., Connolly, A. J., Dalcanton, J., Doi, M., Eisenstein, D., Frieman, J. A., Fukugita, M., Gunn, J. E., Ivezić, Ž., Kent, S., Kim, R. S. J., Knapp, G. R., Kron, R. G., Munn, J. A., Newberg, H. J., Nichol, R. C., Okamura, S., Quinn, T. R., Richmond, M. W., Schlegel, D. J., Shimasaku, K., SubbaRao, M., Szalay, A. S., Vanden Berk, D., Vogeley, M. S., Yanny, B., Yasuda, N., York, D. G., and Zehavi, I. (2002). Spectroscopic Target Selection in the Sloan Digital Sky Survey: The Main Galaxy Sample. *The Astronomical Journal*, 124(3):1810–1824.

Tasitsiomi, A., Kravtsov, A. V., Wechsler, R. H., and Primack, J. R. (2004). Modeling Galaxy-Mass Correlations in Dissipationless Simulations. *ApJ*, 614(2):533–546.

Tinker, J. L., Brownstein, J. R., Guo, H., Leauthaud, A., Maraston, C., Masters, K., Montero-Dorta, A. D., Thomas, D., Tojeiro, R., Weiner, B., Zehavi, I., and Olmstead, M. D. (2017). The Correlation between Halo Mass and Stellar Mass for the Most Massive Galaxies in the Universe. *The Astrophysical Journal*, 839(2):121.

Tinker, J. L., Weinberg, D. H., Zheng, Z., and Zehavi, I. (2005). On the Mass-to-Light Ratio of Large-Scale Structure. *The Astrophysical Journal*, 631(1):41–58.

Vale, A. and Ostriker, J. P. (2004). Linking halo mass to galaxy luminosity. *Monthly Notices of the Royal Astronomical Society*, 353(1):189–200.

Van Den Bosch, F. C., Aquino, D., Yang, X., Mo, H. J., Pasquali, A., McIntosh, D. H., Weinmann, S. M., and Kang, X. (2008). The importance of satellite quenching for the build-up of the red sequence of present-day galaxies. *Monthly Notices of the Royal Astronomical Society*, 387(1):79–91.

Van Den Bosch, F. C., Norberg, P., Mo, H. J., and Yang, X. (2004). Probing dark matter haloes with satellite kinematics. *Monthly Notices of the Royal Astronomical Society*, 352(4):1302–1314.

Van Den Bosch, F. C., Yang, X., and Mo, H. J. (2003). Linking early- and late-type galaxies to their dark matter haloes. *Monthly Notices of the Royal Astronomical Society*, 340(3):771–792.

Velander, M., Van Uitert, E., Hoekstra, H., Coupon, J., Erben, T., Heymans, C., Hildebrandt, H., Kitching, T. D., Mellier, Y., Miller, L., Van Waerbeke, L., Bonnett, C., Fu, L., Giodini, S., Hudson, M. J., Kuijken, K., Rowe, B., Schrabback, T., and Semboloni, E. (2014). CFHTLenS: The relation between galaxy dark matter haloes and baryons from weak gravitational lensing. *Monthly Notices of the Royal Astronomical Society*, 437(3):2111–2136.

Virtanen, P., Gommers, R., Oliphant, T. E., Haberland, M., Reddy, T., Cournapeau, D., Burovski, E., Peterson, P., Weckesser, W., Bright, J., van der Walt, S. J., Brett, M., Wilson, J., Millman, K. J., Mayorov, N., Nelson, A. R., Jones, E., Kern, R., Larson, E., Carey, C. J., Polat, I., Feng, Y., Moore, E. W., VanderPlas, J., Laxalde, D., Perktold, J., Cimrman, R., Henriksen, I., Quintero, E. A., Harris, C. R., Archibald, A. M., Ribeiro,

A. H., Pedregosa, F., van Mulbregt, P., Vijaykumar, A., Bardelli, A. P., Rothberg, A., Hilboll, A., Kloeckner, A., Scopatz, A., Lee, A., Rokem, A., Woods, C. N., Fulton, C., Masson, C., Häggström, C., Fitzgerald, C., Nicholson, D. A., Hagen, D. R., Pasechnik, D. V., Olivetti, E., Martin, E., Wieser, E., Silva, F., Lenders, F., Wilhelm, F., Young, G., Price, G. A., Ingold, G. L., Allen, G. E., Lee, G. R., Audren, H., Probst, I., Dietrich, J. P., Silterra, J., Webber, J. T., Slavič, J., Nothman, J., Buchner, J., Kulick, J., Schönberger, J. L., de Miranda Cardoso, J. V., Reimer, J., Harrington, J., Rodríguez, J. L. C., Nunez-Iglesias, J., Kuczynski, J., Tritz, K., Thoma, M., Newville, M., Kümmerer, M., Bolingbroke, M., Tartre, M., Pak, M., Smith, N. J., Nowaczyk, N., Shebanov, N., Pavlyk, O., Brodtkorb, P. A., Lee, P., McGibbon, R. T., Feldbauer, R., Lewis, S., Tygier, S., Sievert, S., Vigna, S., Peterson, S., More, S., Pudlik, T., Oshima, T., Pingel, T. J., Robitaille, T. P., Spura, T., Jones, T. R., Cera, T., Leslie, T., Zito, T., Krauss, T., Upadhyay, U., Halchenko, Y. O., and Vázquez-Baeza, Y. (2020). SciPy 1.0: fundamental algorithms for scientific computing in Python. *Nature Methods 2020 17:3*, 17(3):261–272.

Vogelsberger, M., Genel, S., Springel, V., Torrey, P., Sijacki, D., Xu, D., Snyder, G., Nelson, D., and Hernquist, L. (2014). Introducing the Illustris Project: simulating the coevolution of dark and visible matter in the Universe. *Monthly Notices of the Royal Astronomical Society*, 444(2):1518–1547.

Wang, E., Wang, H., Mo, H., Lim, S. H., van den Bosch, F. C., Kong, X., Wang, L., Yang, X., and Chen, S. (2018a). The Dearth of Difference between Central and Satellite Galaxies. I. Perspectives on Star Formation Quenching and AGN Activities. *The Astrophysical Journal*, 860(2):102.

Wang, H., Mo, H. J., Chen, S., Yang, Y., Yang, X., Wang, E., van den Bosch, F. C., Jing, Y., Kang, X., Lin, W., Lim, S. H., Huang, S., Lu, Y., Li, S., Cui, W., Zhang, Y., Tweed, D., Wei, C., Li, G., and Shi, F. (2018b). ELUCID. IV. Galaxy Quenching and its Relation to Halo Mass, Environment, and Assembly Bias. *The Astrophysical Journal*, 852(1):31.

Wang, H., Mo, H. J., Chen, S., Yang, Y., Yang, X., Wang, E., van den Bosch, F. C., Jing, Y., Kang, X., Lin, W., Lim, S. H., Huang, S., Lu, Y., Li, S., Cui, W., Zhang, Y., Tweed, D., Wei, C., Li, G., and Shi, F. (2018c). ELUCID. IV. Galaxy Quenching and its Relation to Halo Mass, Environment, and Assembly Bias. *The Astrophysical Journal*, 852(1):31.

Warren, M. S., Abazajian, K., Holz, D. E., and Teodoro, L. (2006). Precision Determination of the Mass Function of Dark Matter Halos. *The Astrophysical Journal*, 646(2):881–885.

Weinmann, S. M., van den Bosch, F. C., Yang, X., and Mo, H. J. (2005). Properties of Galaxy Groups in the SDSS: I.– The Dependence of Colour, Star Formation, and Morphology on Halo Mass. *MNRAS*, 366(1):2–28.

Wetzel, A. R., Tinker, J. L., and Conroy, C. (2012). Galaxy evolution in groups and clusters: Star formation rates, red sequence fractions and the persistent bimodality. *Monthly Notices of the Royal Astronomical Society*, 424(1):232–243.

Wetzel, A. R., Tinker, J. L., Conroy, C., and van den Bosch, F. C. (2013). Galaxy evolution in groups and clusters: satellite star formation histories and quenching time-scales in a

hierarchical Universe. *Monthly Notices of the Royal Astronomical Society*, 432(1):336–358.

White, M. (2001). The redshift-space power spectrum in the halo model. *Monthly Notices of the Royal Astronomical Society*, 321(1):1–3.

White, S. D. M. and Rees, M. J. (1978). Core condensation in heavy halos: a two-stage theory for galaxy formation and clustering.

Woo, J., Dekel, A., Faber, S. M., and Koo, D. C. (2015). Two conditions for galaxy quenching: compact centres and massive haloes. *Monthly Notices of the Royal Astronomical Society*, 448(1):237–251.

Woo, J., Dekel, A., Faber, S. M., Noeske, K., Koo, D. C., Gerke, B. F., Cooper, M. C., Salim, S., Dutton, A. A., Newman, J., Weiner, B. J., Bundy, K., Willmer, C. N., Davi, M., and Yan, R. (2013). Dependence of galaxy quenching on halo mass and distance from its centre. *Monthly Notices of the Royal Astronomical Society*, 428(4):3306–3326.

Yang, X., Mo, H. J., and Van den Bosch, F. C. (2003a). Constraining galaxy formation and cosmology with the conditional luminosity function of galaxies. *Monthly Notices of the Royal Astronomical Society*, 339(4):1057–1080.

Yang, X., Mo, H. J., and Van den Bosch, F. C. (2003b). Constraining galaxy formation and cosmology with the conditional luminosity function of galaxies. *Monthly Notices of the Royal Astronomical Society*, 339(4):1057–1080.

Yang, X., Mo, H. J., and Van den Bosch, F. C. (2009). Galaxy groups in the SDSS DR4. III. The luminosity and stellar mass functions. *Astrophysical Journal*, 695(2):900–916.

Yang, X., Mo, H. J., van den Bosch, F. C., Pasquali, A., Li, C., and Barden, M. (2007). Galaxy Groups in the SDSS DR4. I. The Catalog and Basic Properties. *The Astrophysical Journal*, 671(1):153–170.

Yang, X., Mo, H. J., Van Den Bosch, F. C., Zhang, Y., and Han, J. (2012). Evolution of the galaxydark matter connection and the assembly of galaxies in dark matter halos. *Astrophysical Journal*, 752(1).

York, D. G., Adelman, J., Anderson, Jr., J. E., Anderson, S. F., Annis, J., Bahcall, N. A., Bakken, J. A., Barkhouser, R., Bastian, S., Berman, E., Boroski, W. N., Bracker, S., Briegel, C., Briggs, J. W., Brinkmann, J., Brunner, R., Burles, S., Carey, L., Carr, M. A., Castander, F. J., Chen, B., Colestock, P. L., Connolly, A. J., Crocker, J. H., Csabai, I., Czarapata, P. C., Davis, J. E., Doi, M., Dombeck, T., Eisenstein, D., Ellman, N., Elms, B. R., Evans, M. L., Fan, X., Federwitz, G. R., Fiscelli, L., Friedman, S., Frieman, J. A., Fukugita, M., Gillespie, B., Gunn, J. E., Gurbani, V. K., de Haas, E., Haldeman, M., Harris, F. H., Hayes, J., Heckman, T. M., Hennessy, G. S., Hindsley, R. B., Holm, S., Holmgren, D. J., Huang, C.-h., Hull, C., Husby, D., Ichikawa, S.-I., Ichikawa, T., Ivezić, Ž., Kent, S., Kim, R. S. J., Kinney, E., Klaene, M., Kleinman, A. N., Kleinman, S., Knapp, G. R., Korienek, J., Kron, R. G., Kunszt, P. Z., Lamb, D. Q., Lee, B., Leger,

R. F., Limmongkol, S., Lindenmeyer, C., Long, D. C., Loomis, C., Loveday, J., Lucinio, R., Lupton, R. H., MacKinnon, B., Mannery, E. J., Mantsch, P. M., Margon, B., McGehee, P., McKay, T. A., Meiksin, A., Merelli, A., Monet, D. G., Munn, J. A., Narayanan, V. K., Nash, T., Neilsen, E., Neswold, R., Newberg, H. J., Nichol, R. C., Nicinski, T., Nonino, M., Okada, N., Okamura, S., Ostriker, J. P., Owen, R., Pauls, A. G., Peoples, J., Peterson, R. L., Petravick, D., Pier, J. R., Pope, A., Pordes, R., Prosapio, A., Rechenmacher, R., Quinn, T. R., Richards, G. T., Richmond, M. W., Rivetta, C. H., Rockosi, C. M., Ruthmansdorfer, K., Sandford, D., Schlegel, D. J., Schneider, D. P., Sekiguchi, M., Sergey, G., Shimasaku, K., Siegmund, W. A., Smee, S., Smith, J. A., Snedden, S., Stone, R., Stoughton, C., Strauss, M. A., Stubbs, C., SubbaRao, M., Szalay, A. S., Szapudi, I., Szokoly, G. P., Thakar, A. R., Tremonti, C., Tucker, D. L., Uomoto, A., Vanden Berk, D., Vogeley, M. S., Waddell, P., Wang, S.-i., Watanabe, M., Weinberg, D. H., Yanny, B., and Yasuda, N. (2000). The Sloan Digital Sky Survey: Technical Summary. *The Astronomical Journal*, 120(3):1579–1587.

Zaritsky, D., Smith, R., Frenk, C., and White, S. D. M. (1993). Satellites of Spiral Galaxies. *ApJ*, 405:464.

Zaritsky, D. and White, S. D. M. (1994). The Massive Halos of Spiral Galaxies. *ApJ*, 435:599.

Zheng, Z., Coil, A. L., and Zehavi, I. (2007). Galaxy Evolution from Halo Occupation Distribution Modeling of {DEEP}2 and {SDSS} Galaxy Clustering. *The Astrophysical Journal*, 667(2):760–779.

zhi Cao, J., Tinker, J. L., Mao, Y. Y., and Wechsler, R. H. (2019). Constraining the scatter in the galaxy-halo connection at Milky Way masses. *arXiv*, 498(4):5080–5092.

Zu, Y. and Mandelbaum, R. (2016). Mapping stellar content to dark matter haloes - II. Halo mass is the main driver of galaxy quenching. *Monthly Notices of the Royal Astronomical Society*, 457(4):4360–4383.

Zwicky, F., Zwicky, and F. (1933). Die Rotverschiebung von extragalaktischen Nebeln. *AcHPh*, 6:110–127.